ADVANCED COLD ENERGY STORAGE MATERIALS FOR A LIGHTWEIGHT REFRIGERATED VEHICLE

by

LIN CONG

A thesis submitted to the University of Birmingham for the degree of

DOCTOR OF PHILOSOPHY

Birmingham Centre for Energy Storage

School of Chemical Engineering

College of Engineering and Physical Sciences

University of Birmingham

October, 2020

UNIVERSITY OF
BIRMINGHAM

University of Birmingham Research Archive

e-theses repository

This unpublished thesis/dissertation is copyright of the author and/or third parties. The intellectual property rights of the author or third parties in respect of this work are as defined by The Copyright Designs and Patents Act 1988 or as modified by any successor legislation.

Any use made of information contained in this thesis/dissertation must be in accordance with that legislation and must be properly acknowledged. Further distribution or reproduction in any format is prohibited without the permission of the copyright holder.

Abstract

Cold-chain transportation is essential for temperature sensitive perishable products. Currently, various vehicle refrigeration systems are used to provide cooling power for temperature controlled vehicles. However, conventional refrigeration systems powered by fossil fuel have high energy consumption and give unwanted emissions from the vehicles. An alternative approach is needed to reduce the negative impact of such vehicles without compromising the performance of the temperature control. The use of cold energy storage provides a promising alternative approaches for temperature controlled vehicles through offering reliable cold energy while eliminating the emission of the vehicles at the same time. Cold storage using phase change materials (PCMs) has attracted a lot of attention in recent decades because of their thermoproperties and material property driven temperature self-control.

This work focuses on the development of PCMs with phase transition temperatures of $-25\,^{\circ}\mathrm{C}$ and $-33\,^{\circ}\mathrm{C}$ for refrigerated transportation. Salt-water based PCMs are targeted for such an application. To improve the properties of the PCMs, thermal conductivity enhancers, and nucleation and thickening/gelling agents are used in the formulation to form composite PCMs.

Those composite PCMs are characterised and the data show that the thermal conductivity and stability of the PCMs are enhanced and the supercooling effect is suppressed effectively due to the addition of modifiers.

The cold loss of a refrigerated container with PCM based cold storage is studied. A High level of energy efficiency can be achieved by installing an air curtain. To demonstrate the effectiveness of it, CFD simulations are carried out on temperature and air velocity distribution. The results show a significant decrease of cold loss.

ACKNOWLEDGEMENTS

In memory of my beloved grandmother.

I would like to express my special thanks to professor Yulong Ding for providing me with the opportunity to this attractive research and guiding me throughout every stage of my PhD project. Thanks to Hubbard Products, who currently is a member of Daikin group, for financially supporting my work and providing invaluable suggestions respect to the orientation of industry.

I would also like to extend my gratitude to my parents and friends who always support me unconditionally and give me the encouragement and assistance.

Last but not least, I would like to thank all the members in BCES group, University of Birmingham. And to all who have helped me during this wonderful journey.

CONTENTS

LIST OF FIGURES

LIST OF TABLES

NOMENCLATURE

Acronyms

ACH Air change per hour

CFD Computational fluid dynamics

COP Coefficient of performance

CR Corrosion rate

DSC Differential scanning calorimetry

LFA Laser flash apparatus

PCM Phase change material

TES Thermal energy storage

VC Conventional vapour compression

XRD X-ray powder diffraction

Symbols

α	Thermal diffusivity
$\bar{\bar{\tau}}$	Stress tensor
β	Thermal expansion coefficient
Δw	Air humidity ratio
$\dot{V}$	Average air velocity
γ	Liquid fraction
λ	Thermal conductivity
μ	Molecular viscosity
∇	Spatial derivative operator
ω	Number of doorway passages
ρ	Density
Θ	Time period
θ	Jet angle
A	Area
C_p	Specific heat

D	Doorway factor
E	Effectiveness
F	Additional body force
F_m	Density factor
g	Acceleration of gravity
H	Heat of fusion
h	Heat transfer coefficient
I	Unit tensor
L	Characteristic length
M	Molecular weight
m	Mass
P	Static pressure
p	Pressure
Q	Energy
R	Universal gas constant
R_a	Rayleigh number

S_m	Additional source term
T	Temperature
t	Time
U	Overall heat transfer coefficient
u	Flow velocity
V	Volume
x	Thickness

CHAPTER 1

INTRODUCTION

1.1 Background

According to the UK Department for Business, Energy & Industrial Strategy (2017), as shown in Figure 1.1, the energy consumption in the transport sector has been rising in the last few decades, making transport one of the largest energy consumption sectors since 1988. Road transport consumes the most energy in the sector, accounting for $\sim$40% of the UK's non-traded emissions in 2016 (Department for Business, Energy & Industrial Strategy, 2018). 11% of the world's electricity is consumed in the cold chain of food, and the energy consumption of refrigerated transport has been widely concerned (Gao, 2019). The great demand for refrigeration transport is expected to be continuously led by the increasing awareness of health and safety issues associated with food and pharmaceutical products. It is predicted that over 9.6 million vehicles will be in the global refrigerated transport market by 2025 (Dearman, 2016).

The increasing number of vehicles is accompanied by unwanted CO_2 emissions, a major factor causing the global warming. In addition, diesel powered refrigerated vehicles emit toxic NO_X and particulate matters during transportation, leading to serious environmental and public health issues. Hence, different refrigerated vehicle solutions, such as cryogenic and eutectic based cooling have been brought to light in recent years, latter has a potential CO_2 reduction of 5%$\sim$22% regarding different scenarios in Europe (Oró et al.,

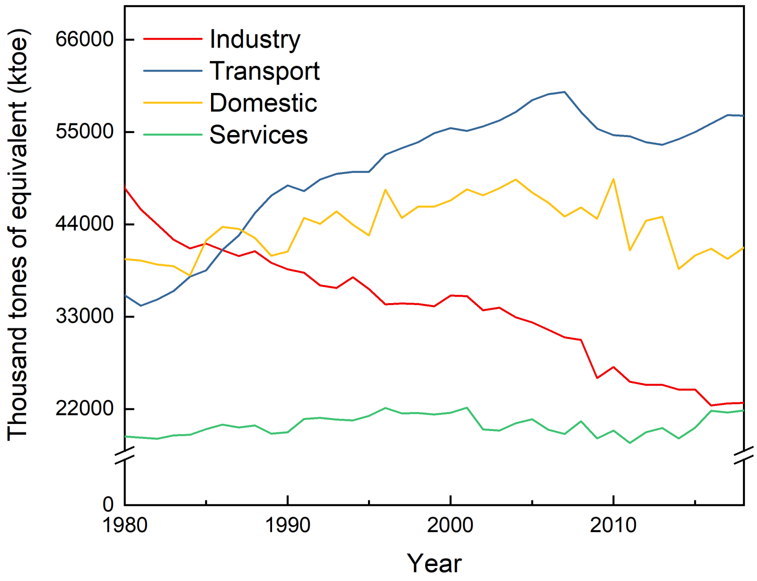

Figure 1.1: Energy consumption by final user from 1980 to 2018 in the UK (Department for Business, Energy & Industrial Strategy, 2017)

2014). Although there are still some technical and economic barriers that hinder their commercial utilisation and large scale development.

1.2 Aims and objectives

This PhD work aims to develop a light-weight solution using passive cooling based phase change materials (PCMs) with an enhanced charging/discharging performance and to understand the energy dissipation in a refrigerated container. The focus is on screening, fabricating and characterising PCMs, optimising thermal performance of the PCMs, and modelling air circulation in a refrigerated container with the presence of air curtain. The specific objectives are:

i) To understand and screen eutectic based PCMs for refrigerated vehicle applications;

ii) To study the thermophysical properties of the screened PCMs, including latent heat; specific heat, thermal conductivity, supercooling, physical stability and chemical stability;

iii) To enhance the performance of the targeted PCMs;

iv) To study the air circulation in a refrigerated container affected by loading/unloading behaviour.

To achieve the objectives in this study, novel research content and methods are involved. In addition to introducing new research approaches, novel results are also found in this study.

· The NaCl-NH_4Cl solution and eutectic $MgCl_2$ solution that exhibited favourable thermophysical properties at $-25\,°C$ and $-33\,°C$ were found;

· The mass ratio of salt and water was optimised;

· An approach was developed for identifying the ternary eutectic point at subzero temperatures;

- The optimised techniques of adding thermal conductivity enhancers, nucleation agents and thickening/gelling agents were developed;
- The impact of the nozzle width, jet velocity and jet angle on the performance of air curtain were first simultaneously studied and the preferable parameter combination was found.

1.3 Methodologies

Theoretical, experimental and modelling methods were used in the work. The experimental work focused on two eutectic salt-water based PCMs suitable at the working temperatures of refrigerated vehicles. The PCM formulations were optimised by thermodynamic analysis. The thermophysical properties were characterised by using differential scanning calorimetry (DSC), laser flash apparatus (LFA), X-ray powder diffraction (XRD), etc. To understand the cold load and air infiltration, simulations based on mathematical models were performed on a refrigerated vehicle using computational fluid dynamics (CFD) in a ANSYS FLUENT environment.

1.4 Layout of the thesis

This thesis consists of 7 Chapters:

- Chapter 2 summarises the key relevant technologies to vehicle refrigeration systems and methods of evaluating thermophysical properties of PCMs. The main challenges and potential solutions are outlined with a focus on based PCMs. Numerical studies on cooling load and air distribution within a vehicle container are also discussed.

- Chapter 3 provides the details of measurement techniques for the thermophysical properties of the PCMs outlined in Chapter 2; and the mathematical modelling including model formulation and numerical solution.

- Chapter 4 details the protocol for screening and formulating the PCMs based on practical application needs.

- Chapter 5 discusses the thermophysical properties of the PCMs formulation using protocols detailed in Chapter 4.

- Chapter 6 details CFD modelling of air distribution of a refrigerated vehicle in different working scenarios.

- Finally, Chapter 7 summaries the main conclusions of the PhD work and also gives an outlook of future work.

To sum up, the outlines of the thesis is presented in Figure 1.2.

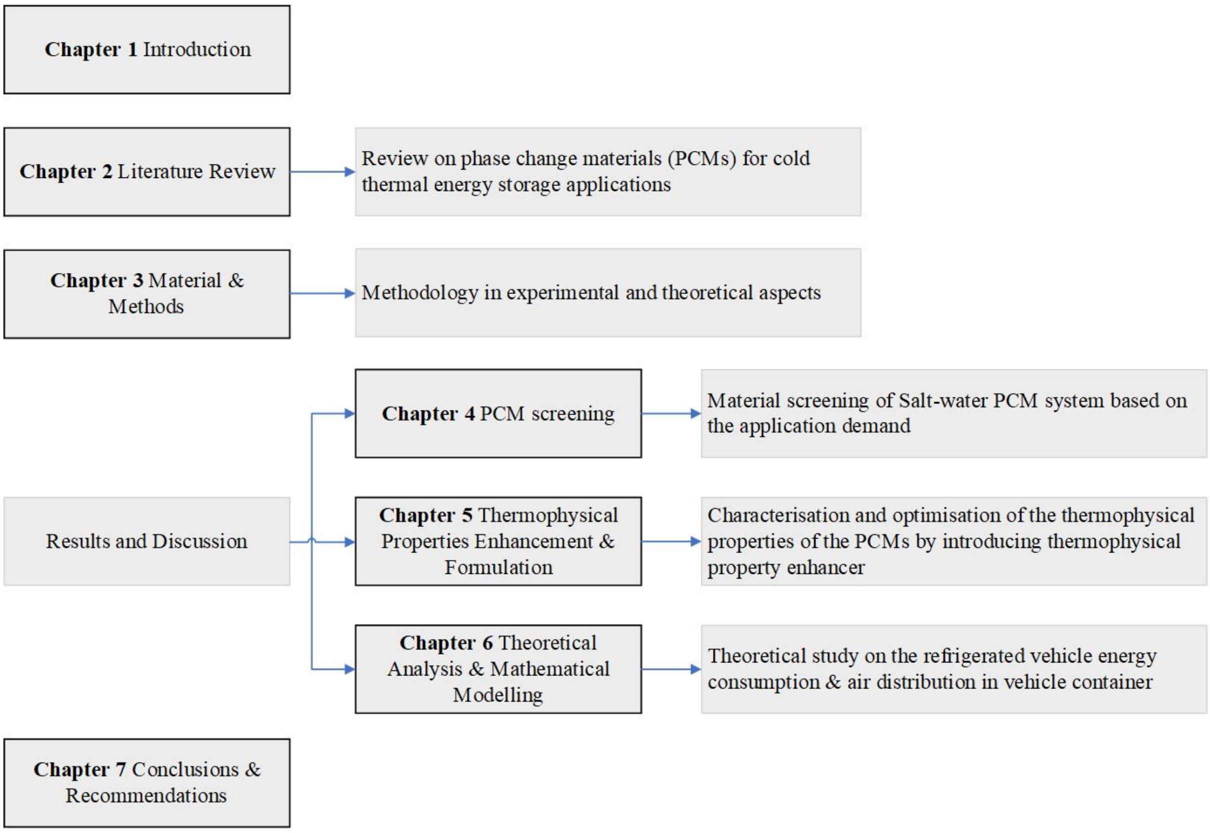

Figure 1.2: The outlines of the thesis

CHAPTER 2

LITERATURE REVIEW

2.1 Vehicle refrigeration systems

Refrigerated vehicle plays a crucial role in temperature-controlled transportation. It helps reduce the chemical and biological activity in foods and subsequent deterioration and the loss of quality, and maintain the functionalities of medicine. Refrigerated vehicles come in different forms from small insulated vans to large multicompartment trailers.

Generally, refrigerated products have their individual ideal storage temperatures. For instance, most frozen food products are stored between $-18\,°\mathrm{C}$ to $-25\,°\mathrm{C}$. The frozen temperatures of some specific perishable foods are shown in Table 2.1.

Table 2.1: The frozen temperature for some perishable food products (ASHRAE, 2010)

Product	Storage temperature (°C)
Fish	-30 to -20
Meat	-23 to -18
Butter	-23
Ice cream 10% fat	-30 to -25
Eggs	-20

One of the fundamental differences between refrigerated vehicles is cooling/heating machinery. Refrigerated vehicles have various interior cooling systems: vapour compression, cryogenic (liquid nitrogen) and eutectic based systems (ASHRAE, 2014a).

2.1.1 Vapour compression system

Conventional vapour compression (VC) technology can be traced back to the early 19th century. It is the dominant technique in the refrigeration system. The vapour compression system contains four components: compressor, condenser, expansion valve and evaporator, as shown in Figure 2.1(a).

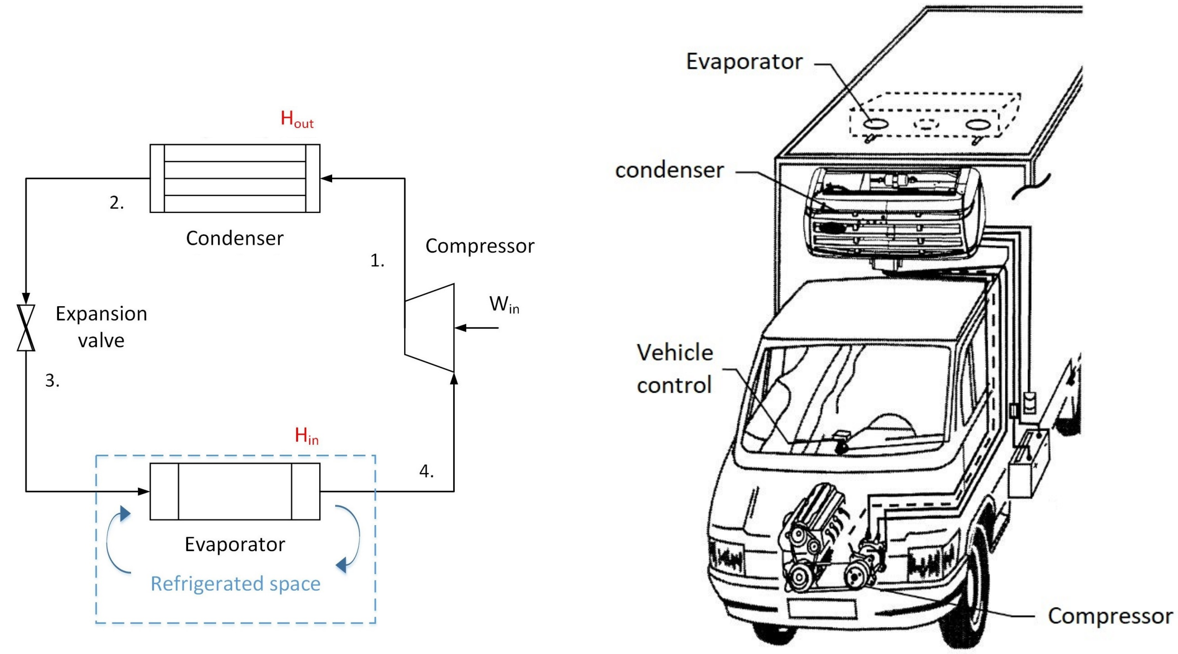

(a) (b)

Figure 2.1: (a) The flow diagram of vapour compression system (Badr, O'Callaghan, and Probert, 1990) (b) A vehicle based VC refrigeration system

In the typical single stage VC refrigeration cycle, refrigerant cycles through the closed-circuit. Mechanical energy is required to drive the compressor, where the refrigerant enters in the form of saturated vapour. Then the saturated vapour is cooled to liquid state in the condenser and releases heat to the atmosphere. After that, the saturated liquid flows through the expansion valve, in which both pressure and temperature decrease. The evaporation process in evaporator extracts heat from the refrigerated space and transfers the refrigerant back to the compressor in vapour state, which cools the refrigerated space. Figure 2.1(b) shows how a VC refrigeration system works in a vehicle system (ASHRAE, 2014a). The temperature of the refrigerated space is managed by vehicle control system through the on-off cycles of the compressor. R134a, R404a and R290 are widely used commercial refrigerants (CIBSE, 2009).

The VC system is relatively energy inefficient with noise pollution and exhaust emission (Tassou et al., 2010). Additionally, food quality and shelf life deteriorate faster because of temperature fluctuation during the long-distant transport from manufactures to retailers.

2.1.2 Cryogenic cooling system

Cryogenic cooling system is an alternative approach to mechanical VC refrigeration. It is an open-circuit system powered by a cryogenic cold source such as liquid nitrogen or liquefied carbon dioxide. The liquefied gas is stored in a cryogenic storage vessel which can be pressurised as illustrated in Figure 2.2. During the refrigeration process it is pumped to the sealed evaporator coils where the cryogenic liquid is gasified and expands, cooling down the vehicle envelope. After that, the expanded gas is exhausted to the atmosphere. The system usually has a stand-by heater that is used for temperature control, defrosting etc. Another example, as is reported by Dearman, is that part of the cryogenic liquid flows directly into the refrigeration unit and combines with a hot heat exchange fluid, which reclaims heat from the condenser, and can doubles the efficiency of the system as claimed by the developer (Dearman, 2016).

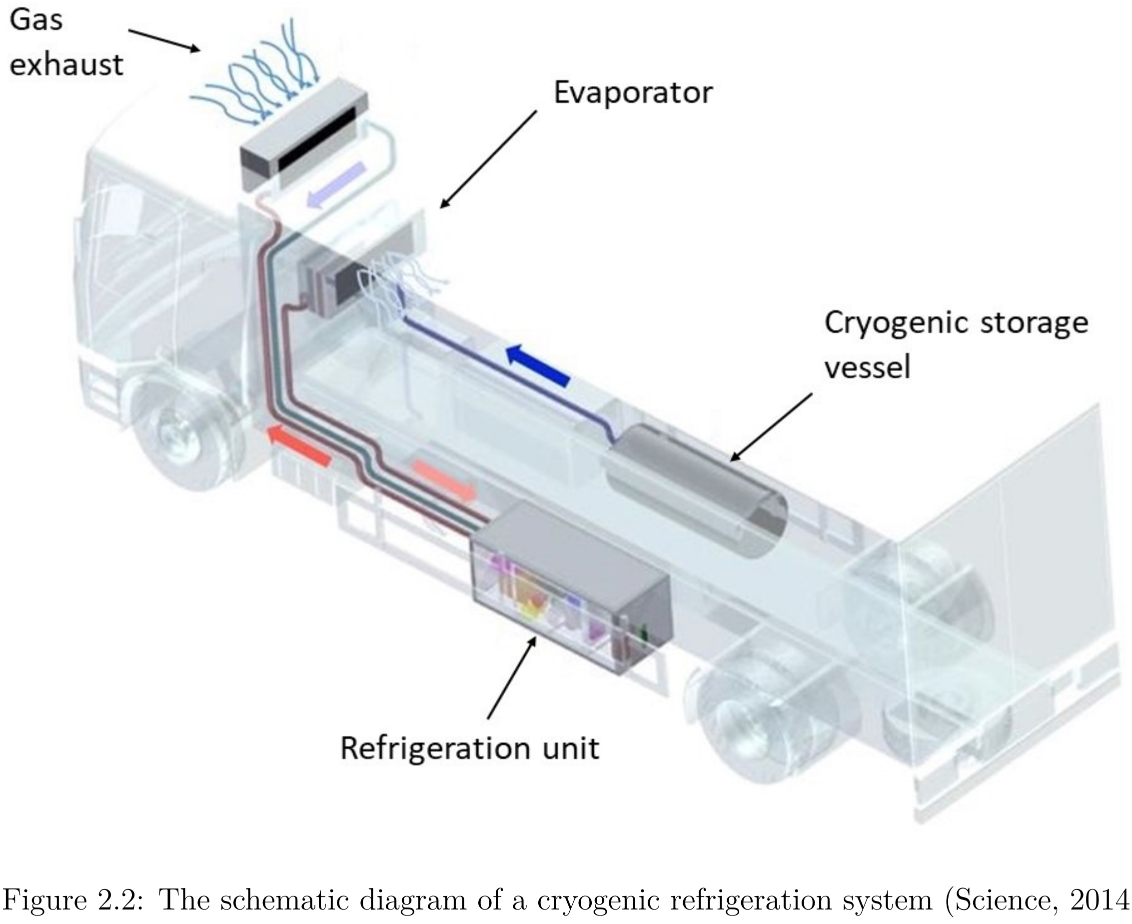

Figure 2.2: The schematic diagram of a cryogenic refrigeration system (Science, 2014)

Cryogenic cooling system reduces the fuel consumption and noise level compared with the conventional VC system. It has a higher energy efficiency, and is more eco-friendly with a longer service life. However, this system is suitable for cargo-sized vehicle only considering that the scale of the storage vessel and cost. It requires additional infrastructures for cryogenic liquid refilling refrigerant as well.

2.1.3 Eutectic system

Eutectic system is a thermal energy storage unit integrated into a refrigerated vehicle. It contains the phase change material encapsulated in hollow tubes, beams or plates in the refrigerated container (Tassou, De-Lille, and Ge, 2009). Some commercial refrigerated vehicles with different forms of eutectic system are presented in Figure 2.4, which demonstrates that the eutectic system can be located at ceiling or walls of the vehicle. According to the transport condition demand, various options of PCMs can be employed to meet different temperatures and operating time.

During transport, the eutectic system employs the PCM that provides cold energy which is stored during electric off-peak time by direct refrigeration. Figure 2.3 provides a guidance of the map of the off-peak electricity in the UK. According to Green Energy UK, it offers a 5p per kWh tariff for overnight hours and a 25p for peak time on weekdays. Moreover, the charging unit of the eutectic system can be located either on board of the vehicle or stationary, which greatly enhances versatility of the vehicle.

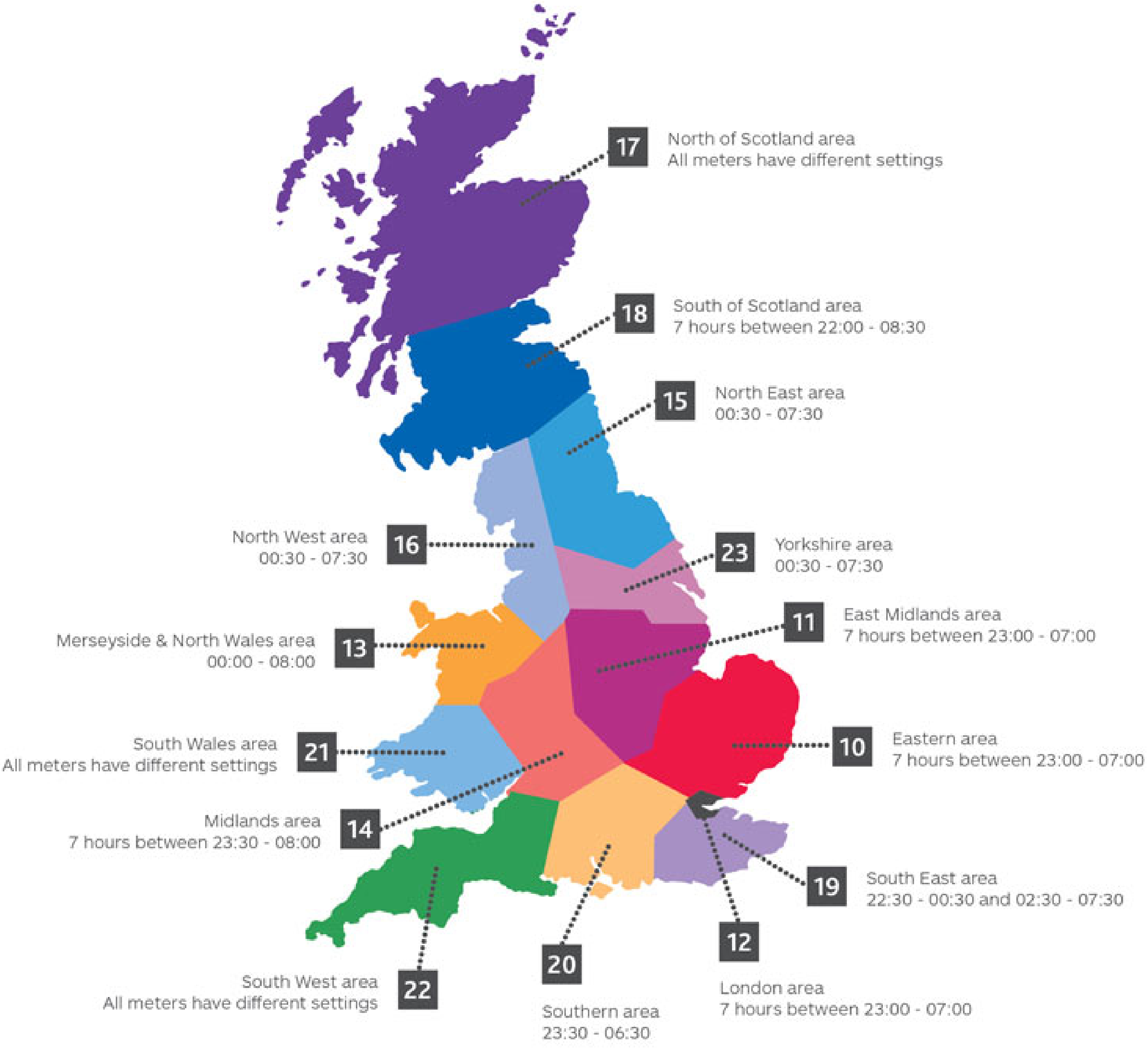

Figure 2.3: The map of economy 7 hours in the UK (Npower, 2020)

It is reported that the compressor running time is reduced by 2∼36% with the PCM installed compared with the VC system. And 20%∼27% coefficient of performance (COP) improvement of refrigeration cycle can be observed that lowers the operational cost (Khan and Afroz, 2013). As is mentioned above, the cryogenic cooling system is suitable for large vehicles, whereas the eutectic system provides more flexibility and satisfies different market demands. The long life-span of the eutectic beams contributes to the lower cost compared with the open-circuit system of the cryogenic cooling. Most importantly, its reliable isothermal behaviour and high energy storage density have made it more attractive compared with other technologies.

Eutectic system has a long life expectancy, low maintenance cost and no emission or engine noises during the transport. It is especially popular in temperature sensitive refrigeration applications for both long distance and multi-drop home deliveries. However, the energy storage density of the current eutectic system is relatively low, which results in a large and heavy eutectic unit that occupies too much of the cooling space and waste a lot of energy. Hence a light-weight replacement needs to be developed.

2.2 PCM Classification & characterisation

As is discussed above, integrating thermal energy storage (TES) technology into refrigerated vehicles can improve the performance of the cooling capability and reduce environmental impact. There are three TES techniques available: sensible heat storage, latent heat storage and thermochemical storage. Their energy storage capabilities are compared in Table 2.2.

Sensible heat storage materials store heat by rising the material temper-

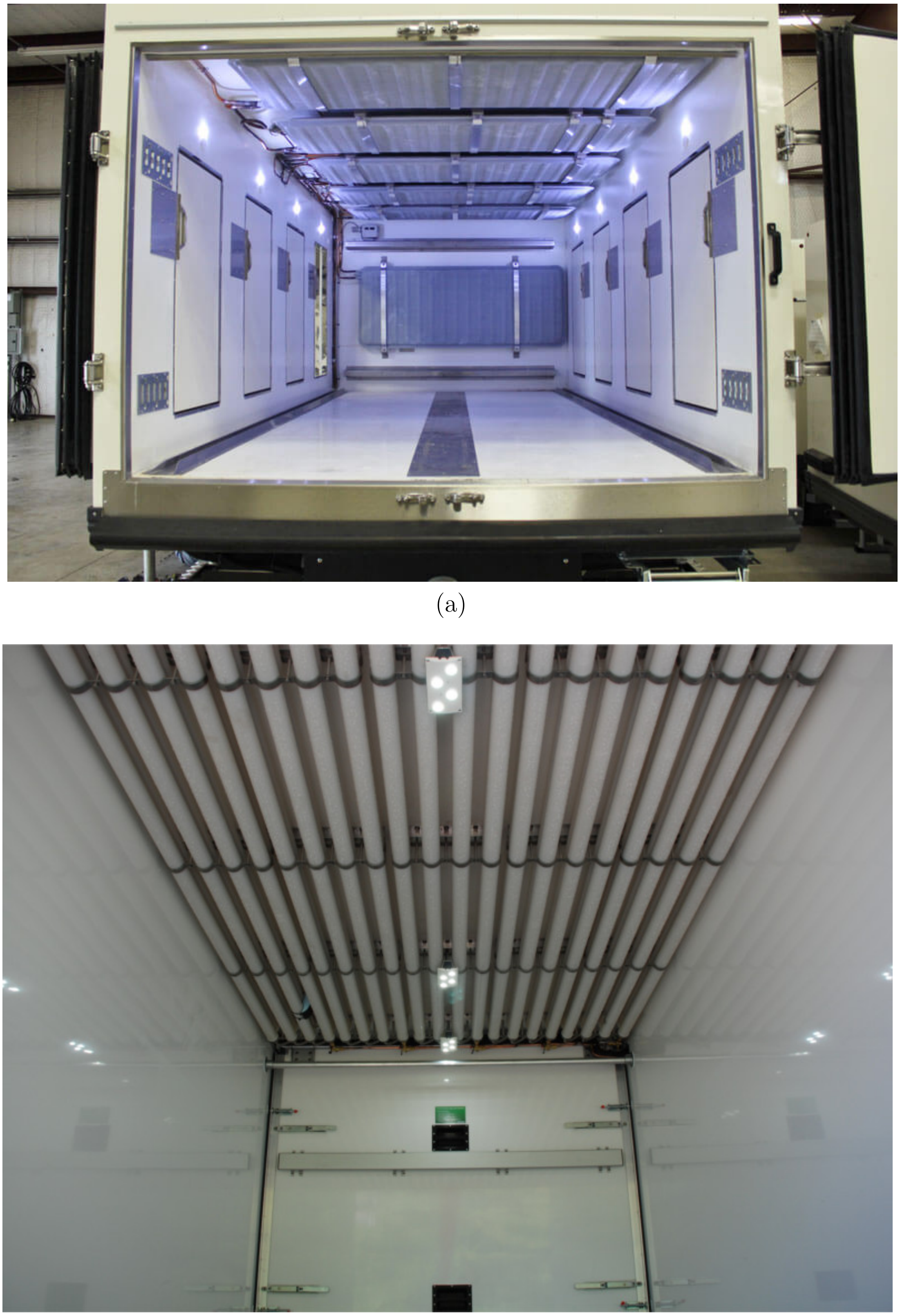
(a)

(b)

Figure 2.4: The images of (a) eutectic plates (ColdCar, 2016), (b) eutectic beams (Coachworks, 2018) on refrigerated vehicle

Table 2.2: The comparison of difference thermal storage techniques (Safari et al., 2017)

Storage type	Capacity (kWh/t)	Power (MW)	Efficiency (%)	Storage period	Cost (€/kW h)
Sensible	10-50	0.001-10	50-90	day-month	0.1-10
Latent	50-150	0.001-1	75-90	hour-month	10-15
Thermochemical	120-250	0.01-1	75-100	hour-month	8-100

ature. That is, the thermal energy that can be stored in a sensible heat storage material solely depends on the specific heat capacity and the highest temperature at which the material can operate (Lane, 1983):

$$Q_{sens} = \int_{T_0}^{T_1} mC_p dT \tag{2.1}$$

where, m, C_p are the mass and specific heat of the material, [kg], T_0, T_1 are the final temperature and initial temperature of the storage material, [K], correspondingly.

Latent heat storage materials, undergo an isothermal progress during phase change. Figure 2.5 compares the sensible heat storage and latent heat storage technologies, and gave the conclusion that, the latter can store more energy than the prior over the same temperature range. The energy density of the latent heat storage materials can be calculated with (Lane, 1983):

$$Q_{pcm} = m(\int_{T_0}^{T_m} C_p dT + \Delta H + \int_{T_m}^{T_1} C_p dT) \tag{2.2}$$

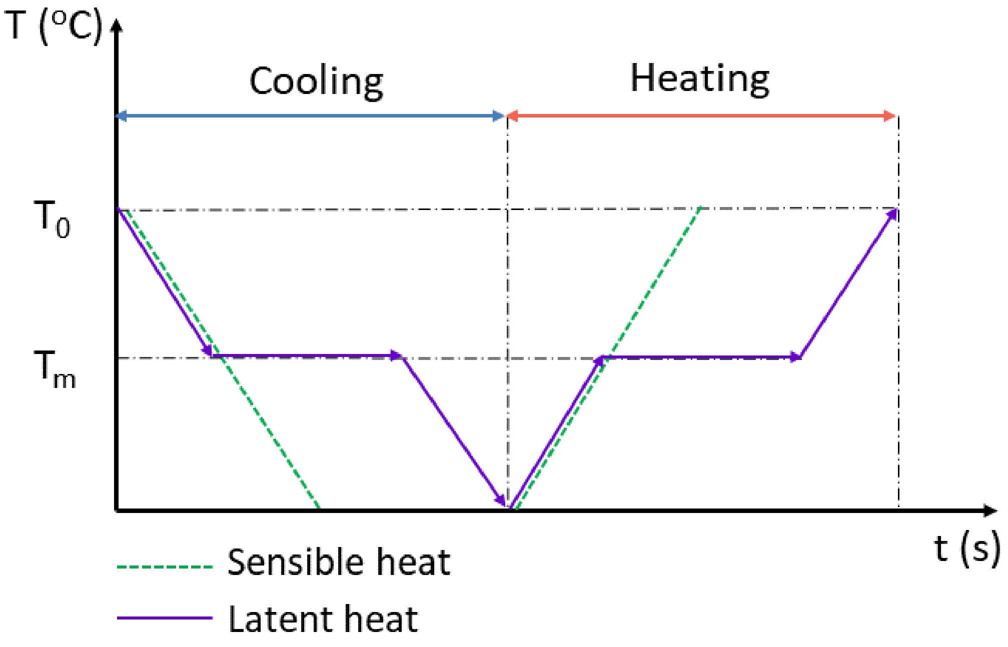

Figure 2.5: The schematic diagram of sensible heat and latent heat (Mehling and Cabeza, 2008)

where, T_m is the phase change temperature [K], ΔH is the latent heat of the material [kJ/kg].

Thermochemical storage which is based on reversible chemical reactions is mainly used at medium and high temperatures (Abedin and Rosen, 2011). The endothermic/exothermic reactions can be written as:

$$A + Q \rightleftharpoons B + C \tag{2.3}$$

and the energy stored is determined by:

$$Q_{thermochem} = m\alpha\Delta h \tag{2.4}$$

where, α is the extend of the chemical conversion, Δh is the reaction heat.

Among them, latent heat storage has gained the most attention over other TES materials because of its high energy storage capacity and constant operating temperature (Oró et al., 2012). Each latent heat storage material, also known as phase change material (PCM), has a specific phase change temperature. PCM has the potential of providing extra cooling power to refrigerated vehicles. A suitable phase change temperature is one of the most important criteria during PCM screening. Some desirable thermal dynamic, chemical, economic and environmental properties of ideal PCMs are listed in Table 2.3.

2.2.1 PCM Classification

Figure 2.6 shows that the classification of PCMs can be used in cold energy storage. They are widely applied in peak load shifting, food storage and transportation, free cooling and air conditioning systems etc (Gin and Farid, 2010; Oró et al., 2012; Veerakumar and Sreekumar, 2016; Cabeza et al., 2011). There are four classes of PCMs: liquid-gas materials, solid-gas materials, solid-solid materials and solid-liquid materials. The development of liquid-gas

Table 2.3: Criteria of selecting ideally PCMs (Zhou, Zhao, and Tian, 2012)

Properties	Criteria
Thermal dynamic	· Suitable phase-change temperature · High thermal conductivity · High latent heat of fusion per unit mass · High specific heat and high density · Congruent melting and no segregation · Little supercooling · Small volume variation and small vapour pressure
Chemical	· Completely reversible melting/solidification cycles · Long term chemical stability · Compatibility with other materials · Non-toxic, non-flammable and non-explosive
Economic	· Abundant and available · Cost-effective
Environmental	· Low environmental impact · Recycling potential

and solid-gas PCMs is hindered by the significant volume change because the gas phase is involved in the phase change process. It causes issues in encapsulation and increases the complexity of the system (Su, Darkwa, and Kokogiannakis, 2015). Because solid-liquid PCMs have higher latent heat compare with solid-solid PCMs, and during the phase change, their volume change is normally negligible, they become the most popular and effective choice in energy storage.

Solid-liquid PCMs can be divided into organic materials, inorganic ma-

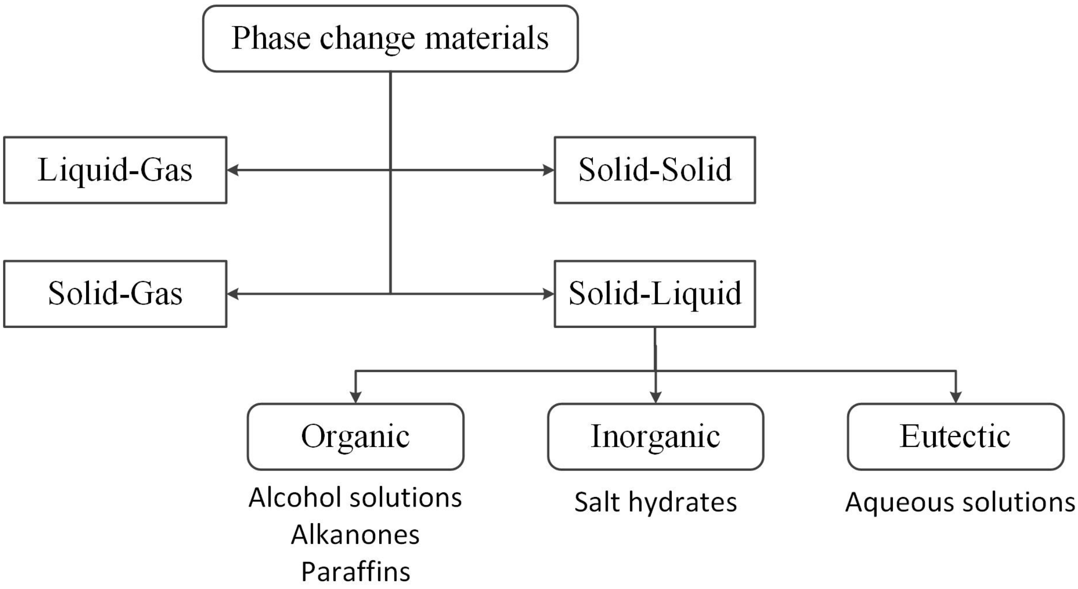

Figure 2.6: Classification of latent heat energy storage materials for low temperature applications

terials and eutectics according to their chemical compositions. Their phase change temperature and fusion heat are shown in Figure 2.7. It is indicated that for low temperature applications, proper PCMs can be selected according to their phase change temperature. Their latent heat varies from 60 to 600 kJ/kg.

2.2.1.1 Organic PCMs

Organic PCMs used in cooling application can be broadly classified as alcohol solutions, alkanones and paraffins (C_nH_{2n+2}). Generally, they are chemically stable, non-corrosive, and appears no phase separation and little supercooling problem (Veerakumar and Sreekumar, 2016). Organic materials usually have low energy storage density and low thermal conductivity. Moreover, they

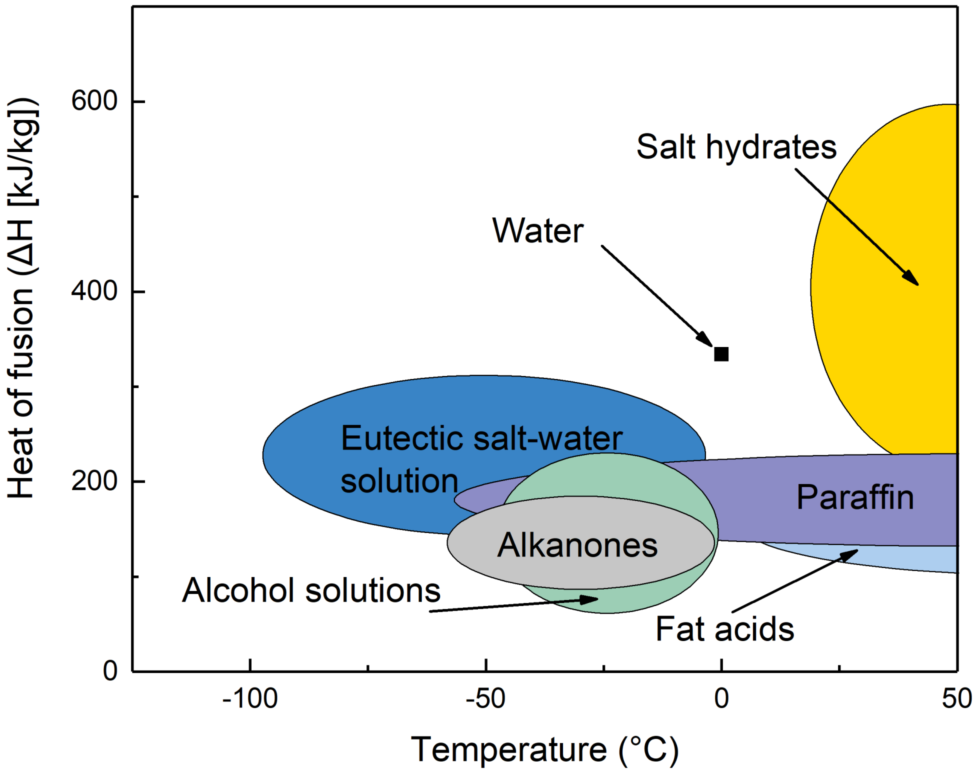

Figure 2.7: Solid-liquid materials being investigated and used as PCMs for low temperature applications (Dieckmann, 2006; Li et al., 2013a)

have potential issues because of their flammability, varying levels of toxicity and biodegradable properties.

2.2.1.2 Inorganic PCMs

Inorganic PCMs are non-flamable and cost-effective and they have higher heat of fusion, thermal conductivity and density compared with organic PCMs. Amongst them, salt hydrate is considered one of the most attractive inorganic materials that have been extensively studied by many researchers (Xie et al., 2017). Still, inorganic materials have some drawbacks, for instance, phase separation, supercooling issues and poor compatibility with some metals. To summarise, a radar chart Figure 2.8 shows the comparison between organic and inorganic PCMs.

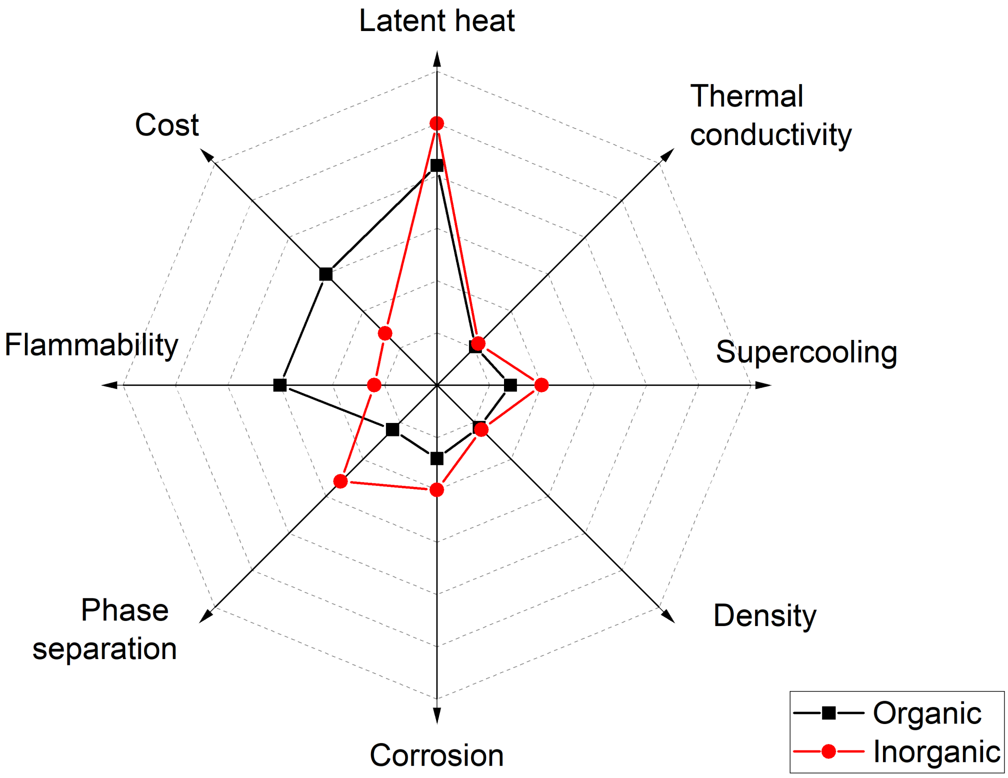

Figure 2.8: The thermoproperties comparison of organic PCMs and Inorganic PCMs

2.2.1.3 Eutectics

In most cases, a particular type of PCM has inherent disadvantages and can not meet all the application requirements, while the thermal properties can be optimised by mixing two or more PCMs to form eutectics with improved performance.

"Eutectic" is a Greek word which means "easy melting". According to the Freezing Point Depression Theory, the introduction of a new component decreases the phase change temperature of the original system. The phase change temperature decreases further when more solutes are added, which was evidently illustrated in Kumano et al.'s study. The effects of introducing organic and inorganic materials in water were displayed in Figure 2.9, respectively. It is shown that either adding organic or inorganic solutes decrease the freezing point, latent heat of water. Further more, the tendency of the latent heat decreasing is more significant in organic aqueous solutions than in inorganics at the same temperature range (Kumano et al., 2007).

The eutectic temperature is the lowest phase change temperature over the mixing ratio of all the involved components, as shown in Figure 2.10. The x-coordinate presents the composition of the component species, y-coordinate stands for the phase change temperature. It can be seen in the DSC curves that along with the composition change of the PCM, the liquidus line changes accordingly. For a certain composition following the red dot, PCM transfers from liquid state to half liquid half solid state when the temperature drops below point C. When the temperature is lower than point D, the PCM is completely frozen, and transforms into solid state. When the components have a collaborative phase transition from plain liquid to plain solid directly

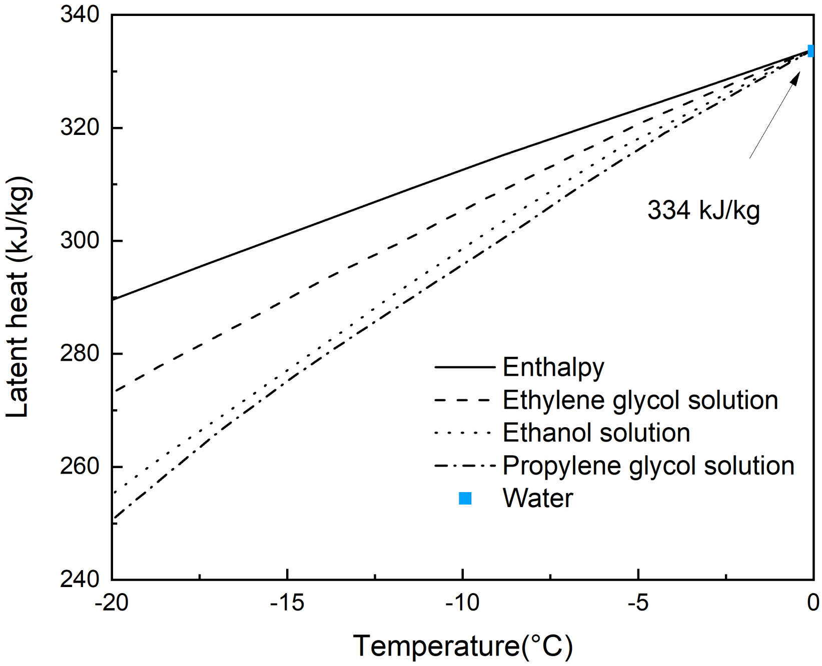

(a)

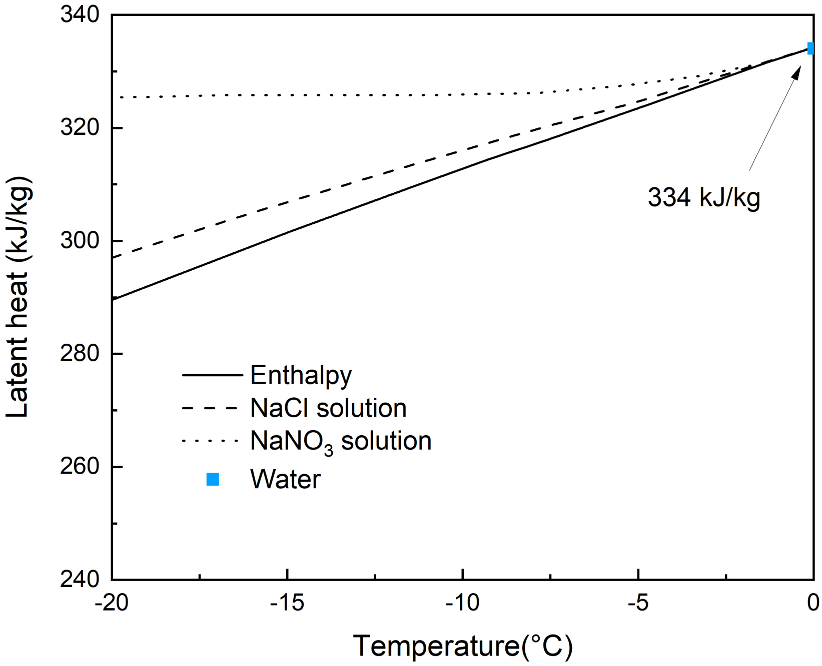

(b)

Figure 2.9: The freezing point depression phenomenon of water with (a) organic and (b) inorganic solvents

at the point T_e. Point T_e is the eutectic composition.

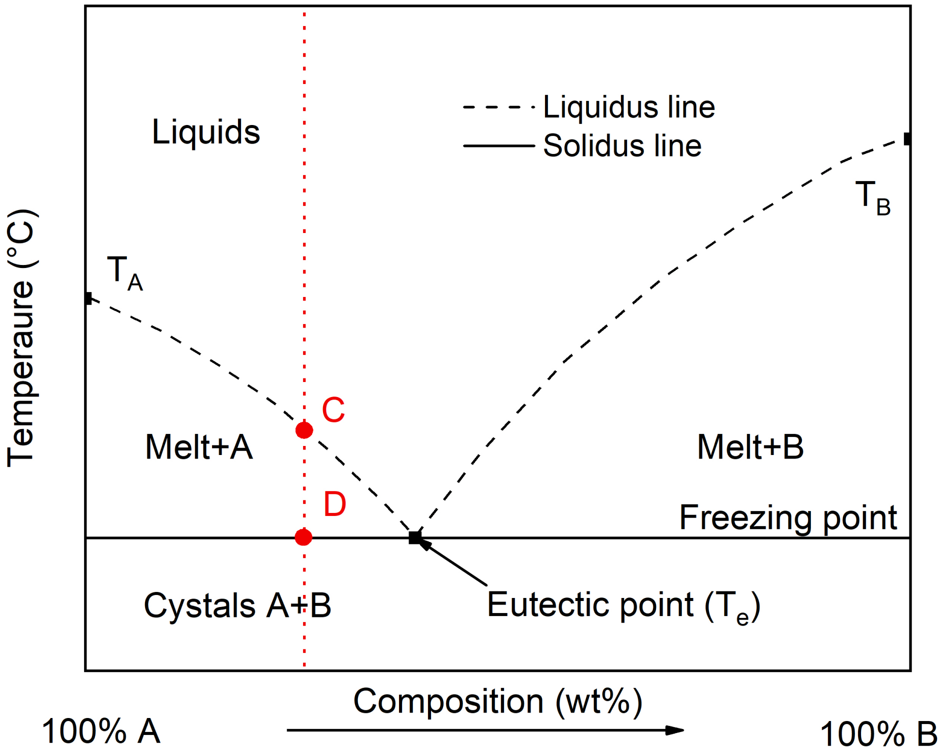

Figure 2.10: The typical phase diagram of binary PCM system

2.2.2 PCM in cooling applications

Many researchers have carried out studies on integrating PCMs with cooling applications. Yilmaz et al. (2009) developed a new binary organic PCM, they prepared different compositions of Dodecane-Tridecane, Tridecane-Tetradecane and Tetradecane-Pentadecane mixtures and analysed the thermal performance of them, respectively. The working temperatures of these mixtures are from −12 °C to 10 °C, which are suitable for cooling applications. WU et al. (2015) prepared the organic composite PCMs for cold storage. The composition of the organic PCM is caprylic acid/myristyl alcohol with mass ratio of 73.7% : 26.3%. In order to increase the thermal conductivity, they added different nanoparticles, which increased the specific heat at the same time, in the PCM.

For refrigerated vehicle application specifically, Xie, Tao, and Liu (2016) selected ammonium chloride and glycerol as the composite cold storage PCMs. The sample is divided into eight groups according to different mass ratios. The results indicated that the highest latent heat of the mixtures is 214.3kJ/kg. Afterwards, the composite PCM was placed on the hold-over plate in the refrigerated vehicle, and the vehicle maintained interior temperature for more than 48 hours with 8 tons broccoli. Similarly, Shen (2008) mixed ammonium chloride solution and glycol solution in the mass ratio of 3:2. The phase change temperature of the composite PCMs are from −16 °C to −21 °C with a high latent heat from 207 kJ/kg to 212 kJ/kg.

Liu, Saman, and Bruno (2012) incorporated the PCM into the refrigeration system on the refrigerated vehicle. They used a low cost PCM (inorganic salt-water solution) which store and release latent heat at −30.6 °C and −26.7 °C respectively, with the heat of fusion is 154.4 kJ/kg. In order to decrease the supercooling effect, fine glass powder and pumice powder were added. However, no noticeable impact was observed. The duration of the freezing is 10 h below −18 °C. Their phase change thermal storage unit is shown in Figure 2.11.

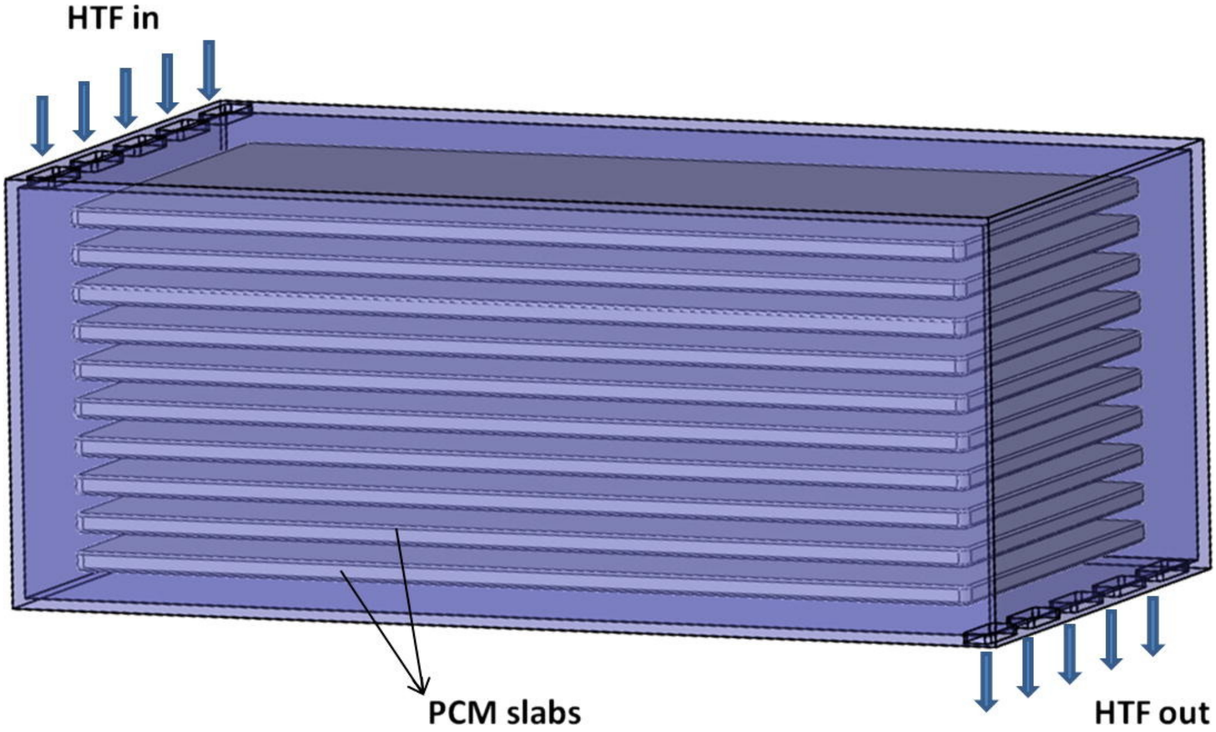

Figure 2.11: The phase change thermal storage unit in Liu, Saman, and Bruno's study

Purusothaman et al. (2017) introduced 1-dodecanol as PCM in the ceiling of the vehicle cabin in order to reduce the radiation effect. Figure 2.12 shows the thermal behaviour after inserting the PCM into vehicle ceiling. The new design helps cut off about 30% of the cooling energy demand to maintain the inner cabin temperature.

Huang and Piontek (2017) sandwiched the PCM panels into the vehicle insulator base and tested their performance under three different conditions:

Figure 2.12: The comparison image of vehicle ceiling without/with PCM

extremely high; extremely low, and alternating environment temperature. The air temperature in the vehicle cabin remains steady for the most of time under various environment temperatures.

Ahmed, Meade, and Medina (2010) used a paraffin based PCM to reduce the heat transfer across the insulated walls. The PCM was filled into the panels that were placed on the top and side walls of the vehicle. The cabin temperature was kept at 4 °C. An average reduction of the peak heat transfer rate of 29.1% and the average daily heat flow of 16.3% was obtained.

Sharma and Buddhi (2013b) tested the performance of an off-vehicle PCM refrigeration unit which contained a low cost PCM whose phase change temperature is −15.2 °C. It was shown that the refrigeration unit can maintain the space temperature below 5 °C for 2-7 h based on the configuration.

In general, PCM-based refrigerated vehicle applications can be categorised into two types: passive cooling and active cooling. The latter equips with moving parts such as pumps and fans. It buffers the temperature cycles, stores night-time coolness and helps peak load shifting. Many factors need to be considered to develop a PCM based cooling unit for refrigerated vehicles, such as the delivery time, the ambient temperature and humidity condition, time length of door opening, the quality of container insulation material, etc.

2.2.3 PCM Screening & characterisation

Phase change temperature is one of the most critical factor for PCM screening. It does not only directly affect the performance of the refrigeration system but also the quality of the stored foods. According to the demand of the refrigeration market, around 85% of refrigeration market has a maximum storage temperature at $-18\,^{\circ}\mathrm{C}$, which mainly is for transporting frozen meat and fish. Others require a storage temperature at $-25\,^{\circ}\mathrm{C}$, for goods like ice creams. With $7\,^{\circ}\mathrm{C}$ temperature gradient for heat transfer, a favourable temperature for refrigerated transport is $-25\,^{\circ}\mathrm{C}$ and $-33\,^{\circ}\mathrm{C}$, respectively. The thermal properties and cost–performance of PCMs are compared as follows.

The potential PCMs that have been studied for sub-ambient applications and their most studied thermoproperties are summarised and listed in Table 2.4. Apart from academic research, PCMs that are commercially available are investigated, too, as shown in Table 2.5. Compared with the research data, "heat storage capacity" is often used in the commercial Products to indicate the energy storage capability instead of the latent heat. However, because different suppliers calculate the "heat storage capacity" within different temperature range, it is difficult to compare the latent heat of products intuitively. Hence the experiment results in this study are compared with the data in Table 2.4. It is suggested that paraffin, alcohol solution and binary aqueous solution are the most common used PCMs in low temperature applications.

Table 2.4: Experimental and theoretic data of thermal properties of PCMs used for sub-ambient application (Zheng and Wu, 2002; Himran, Suwono, and Mansoori, 1994; Mehling and Cabeza, 2008; Li et al., 2013a; Cabeza et al., 2011; Oró et al., 2012; Toner, Catling, and Light, 2014; Jankowski and McCluskey, 2014)

PCM	Type	Composition (wt.%)	Phase change temperature (°C)	Latent heat (kJ/kg)	Specific heat (kJ/kg K)	Thermal conductivity (W/m K)	Supercooling (K)	Density (kg/m^3)	
						Liquid		Liquid	Solid
$ZnCl_2/H_2O$	Eutectic	51	-62	116.84	-	-	-	-	-
Octane	Organic	-	-56.78	181	0.25	-	-	699	-
$FeCl_3/H_2O$	Eutectic	33.1	-55	155.52	-	-	-	-	-
$CaCl_2/H_2O$	Eutectic	29.8	-55	164.93	2.966	0.560	-	1282	-
Nonane	Organic	-	-53.5	170	0.28	-	-	714	-
$CuCl_2/H_2O$	Eutectic	36	-40	166.17	-	-	-	-	-
K_2CO_3/H_2O	Eutectic	39.6	-36.5	165.36	-	-	-	-	-
$MgCl_2/H_2O$	Eutectic	17.1	-33.6	221.88	2.953	0.531	9-14	1209	-
4-Heptanone	Organic	-	-32.9	141.5	-	-	-	820	-
$Al(NO_3)_3/H_2O$	Eutectic	30.5	-30.6	131	-	-	-	1283	1251
Decane	Organic	-	-29.65	202	2.21	-	-	726	-
$Mg(NO_3)_2/H_2O$	Eutectic	34.6	-29	186.93	-	-	-	-	-
$Zn(NO_3)_2/H_2O$	Eutectic	39.4	-29	169.88	-	-	-	-	-
NH_4F/H_2O	Eutectic	32.3	-28.1	187.83	3.27	-	-	-	-
$NaBr/H_2O$	Eutectic	40.3	-28	175.69	-	-	-	-	-
Undecane	Organic	-	-25.6	177	2.207	-	-	737	-
Li_2SO_4/H_2O	Eutectic	27.9	-23	237.3	-	-	-	-	-
KF/H_2O	Eutectic	21.5	-21.6	225.2	3.4	-	-	-	-
$NaCl/H_2O$	Eutectic	22.4	-21.2	222	3.24	0.578	6.6-8.3	1165	1108
2-Octanone	Organic	-	-20.3	190.4	-	-	-	819	-
$(NH_4)_2SO_4/H_2O$	Eutectic	39.7	-18.5	196	2.75	-	-	-	-
$HCOONa/H_2O$	Eutectic	20	-18	250.2	-	-	-	-	-
$NaNO_3/H_2O$	Eutectic	36.9	-17.7	187.79	-	-	-	-	-
NH_4NO_3/H_2O	Eutectic	41.2	-17.35	186.29	-	-	-	-	-

(To be continued)

Table 2.4 – continued from previous page

PCM	Type	Composition (wt.%)	Phase change temperature (°C)	Latent heat (kJ/kg)	Specific heat (kJ/kg K)	Thermal conductivity (W/m K)	Supercooling (K)	Density (kg/m^3)	
						Liquid		Liquid	Solid
$Ca(NO_3)_2/H_2O$	Eutectic	35	-16	199.35	-	-	-	-	-
NH_4Cl/H_2O	Eutectic	19.5	-16	248.44	-	-	-	-	-
K_2HPO_4/H_2O	Eutectic	36.8	-13.5	197.79	-	-	-	-	-
$Na_2S_2O_3/H_2O$	Eutectic	30	-11	219.86	-	-	-	-	-
KCl/H_2O	Eutectic	19.5	-10.7	283	3.42	0.547	5.6	1126	1105
Diethylene glycol	Organic	-	-10(-7)	247	-	-	-	1120	-
$MnSO_4/H_2O$	Eutectic	32.2	-10.5	213.07	-	-	-	-	-
NaH_2PO_4/H_2O	Eutectic	32.4	-9.9	214.25	-	-	-	-	-
Dodecane	Organic	-	-9.6	216	2.207	0.21	-	745	-
$BaCl_2/H_2O$	Eutectic	22.5	-7.8	246.44	-	-	-	-	-
Triethylene glycol	Organic	-	-7	247	-	-	-	1120	-
$ZnSO_4/H_2O$	Eutectic	27.2	-6.5	235.75	-	-	-	-	-
$Sr(NO_3)_2/H_2O$	Eutectic	24.5	-5.75	243.15	-	-	-	-	-
$KHCO_3/H_2O$	Eutectic	16.95	-5.4	280	3.42	-	-	-	-
Tridecane	Organic	-	-5.3	196	2.207	-	-	753	-
$NiSO_4/H_2O$	Eutectic	20.6	-4.15	258.61	-	-	-	-	-
$MgSO_4/H_2O$	Eutectic	19	-3.9	264.42	-	-	4.2	-	-
Na_2SO_4/H_2O	Eutectic	12.7	-3.6	284.95	-	-	-	-	-
NaF/H_2O	Eutectic	3.9	-3.5	322.7	3.85	-	-	-	-
$NaOH/H_2O$	Eutectic	19	-2.8	265.98	-	-	-	-	-
KNO_3/H_2O	Eutectic	9.7	-2.8	280	2.75	-	-	-	-
Na_2CO_3/H_2O	Eutectic	5.9	-2.1	286	3.71	-	-	-	-
$FeSO_4/H_2O$	Eutectic	13.04	-1.8	286.81	-	-	-	-	-
$CuSO_4/H_2O$	Eutectic	11.9	-1.6	290.91	-	-	-	-	-
H_2O	Solvent	-	0	333	4.2	0.6	-	998	917

Table 2.5: Properties and manufacturers of commercially available PCM products

Product	Manufacturer	Phase change temperature (°C)	Heat storage capacity (kJ/kg)	Specific heat (kJ/kg K)	Thermal conductivity (W/m K)	Density (kg/m^3)
E-26	PCM products	-26	265	3.67	0.58	1250
SP-24	Rubitherm	-22∼-23	250 (±7.5%) (-32∼−17 °C)	2	0.6	1300 (l) 1200 (s)
HS26N	Pluss	-26	272 (-29∼−19 °C)	3.6 (l) 1.7 (s)	-	1200 (l) 1122 (s)
PCM-HS26N	SavEnrg	-26	210 (-26∼−20 °C)	3.6 (l)	1200 (l)	
-	Eutectic	Teappcm	-23	330		
Puretemp-21	Puretemp	-21				
ATS-21	-	Axiotherm	-21	320 (-30∼−15 °C)	3	0.6
1160						
PCM-30	Microtek	-30	150∼160	-	-	730
C-21	ClimSel	-24∼-21	285	-	0.33 (l) 1.45 (s)	

2.3 Salt-water based PCM system

2.3.1 Eutectic Composition

Ternary salts are commonly used in thermal storage applications (Cunha and Eames, 2016). In multi-component systems, there are both experimental and theoretical methods to determine the eutectic ternary composition.

Experimental determination Except "Edisonian approach" which stands for loads of experimental work (Kant, Shukla, and Sharma, 2016), the wet-residues method proposed by Schreinemakers (1893) is an effective way to determine the composition of the solid phase in the saturated solution. It is based on the straight-line of the mixture role in a triangular diagram.

Jiang et al. (2016) studied the ternary $Ca(NO_3)_2$-$LiNO_3$-H_2O system at 0 °C, 25 °C and 50 °C, respectively. The solution temperature was controlled by thermostats. Both liquid phase and solid phase were weighted and analysed by gravimetric titration. Huang et al. (2018) measured the solid-liquid equilibrium of $Na_2S_2O_3$-Na_2SO_4-H_2O system at different temperatures: 5 °C, 10 °C, 18 °C, 60 °C and 80 °C. The over-saturated solution was kept at certain temperature long enough. The liquid phase of the saturated solution was taken by syringe and weighted, then was diluted to analyse the chemical composition with titration method; the solid phase components are measured with X-ray powder diffraction (XRD); water mass fraction was measured with a balance. Not only the inorganic salt-water solution, Gao et al. (2018) also studied the organic ternary solution (2-Naphthaldehyde/4-Methylphthalic Anhydride/Ethyl Acetate) at 15 °C, 25 °C and 35 °C. The phase diagram of the system is determined by the isothermal saturation and schreinemakers' wet residues method.

However, the analytical error and geometrical error may occur in schreinemakers' method (Purdon and Slater, 1946). For instance, mass loss will occur when the solvent is in an open environment, as well as temperature fluctuation during liquid/solid phase transferring. The measurement uncertainty of the titration also needs to be considered. Additionally, the temperature condition of subzero degrees increases the operating complexity. Therefore, new approaches need to be established to study the multicomponent PCMs at low temperatures.

DSC is commonly employed to investigate the thermoproperties of PCMs in a wide temperature range, it can also show the trend of eutectic composition. Rycerz (2013) illustrated that the relationship of phase diagram and DSC curves during a heating or cooling test, as shown in Figure 2.13. Corresponding to Figure 2.10, on the eutectic point, the cooling and heating heat flow curves of DSC showed nice symmetric peaks during phase transition, whereas hypoeutectic concentrations exhibited two endothermic peaks: the melting at the eutectic point and the melting at temperatures above the eutectic temperature. In this case, the eutectic temperature and composition of the PCM can be determined.

Han et al. (2006) observed the same phenomenon with NaCl solutions in their study. He also pointed out that the eutectic melting has the largest heat of fusion area. Katsuki et al. (2017) employed DSC to study the low temperature ternary aqueous solution of acetic acid and sodium chloride.

Hence in the following experiment, DSC is used to obtained the eutectic point and latent heat of the five ternary aqueous solutions. Chapter 3 will further explain the fundamental and method related to DSC.

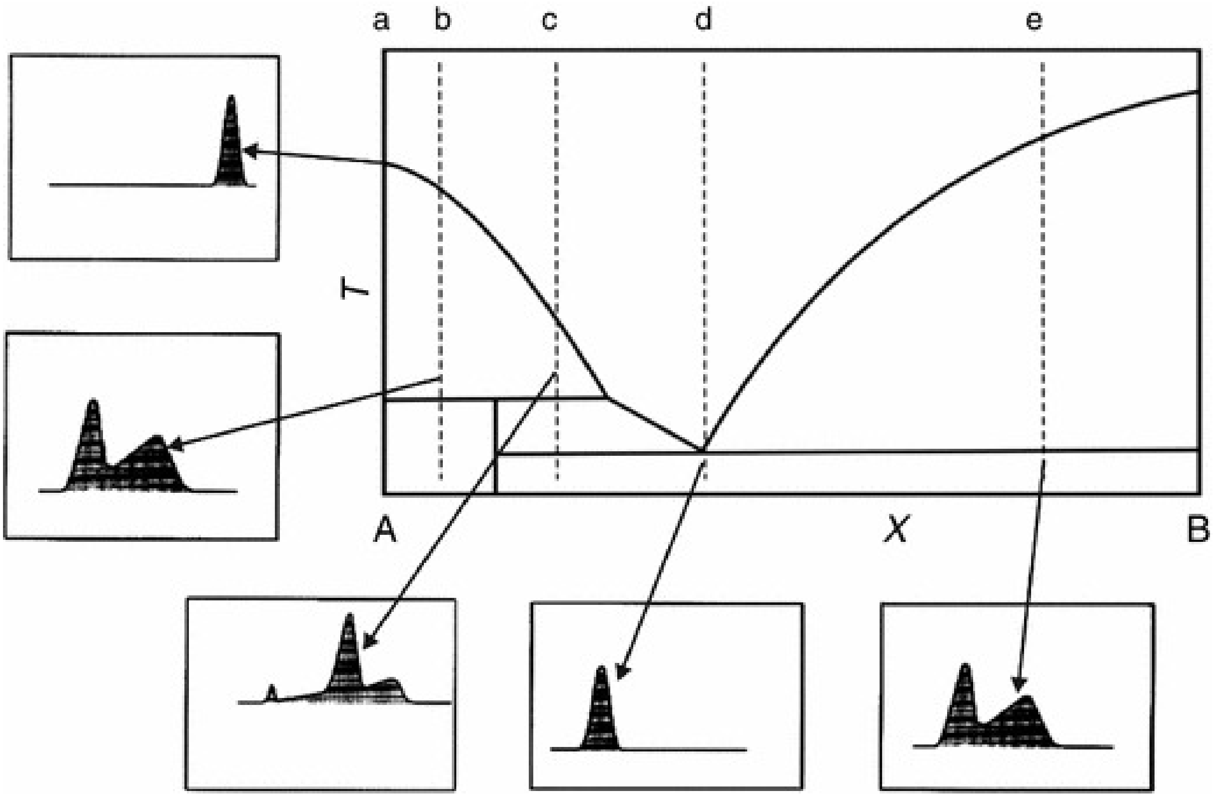

Figure 2.13: The DSC heating curve on a simple phase diagram (Rycerz, 2013)

Schmit et al. (2014) illustrated a three step method to determine eutectic composition of binary and ternary salt hydrates mixtures. They mixed ternary salt hydrates in various mass ratios of two salt hydrate to measure the eutectic point. However, in a salt water solution system, there is no fixed composition of salt-water ratio, which escalate the difficulty of the process. Katsuki et al. (2017) proposed a similar approach to the ternary aqueous solutions that consists of acetic acid and sodium chloride. They tested the mass ratios of sodium chloride in water in DSC, and then examined the mass ratios of acetic acid in the sodium chloride aqueous solutions. It results in 59 groups of samples and heavy work. Therefore, a new method was established to simplify the process.

Theoretical calculation Aside from the experimental research, the theoretical modelling methods are also applied to predict the thermoproperties of the multicomponent PCMs.

The heat of fusion of the multicomponent material H_{m} has been studied by many researchers. Zhang, Su, and Ge (1995) reckoned the fusion heat of eutectic system according to state function entropy. They found that the fusion heat of the multicomponent mixture is certainly less than the fusion heat of one component material, whilst Pasquali, Bettini, and Giordano (2007) suggested that the theoretical fusion heat of the eutectic is directly related to the percentage of each component.

Based on classical electrolyte theory, Semi-empirical model and Fundamental statistical thermodynamics, thermodynamic approaches which are used to predict the phase diagram of the multicomponent PCMs (Deng, Zhou, and Chen, 2013). Those models are widely applied in the electrolyte solution calculations. Although semi-empirical Pitzer equation is one of the most adequate prediction in the process industry, it requires a large number of adjustable parameters that come from experimental data. Unfortunately, there is little experimental data of thermoproperties of ternary aqueous solutions, especially on the subzero conditions.

In conclusion, it is currently difficult to screen and find the suitable eutectic formulation of low temperature multicomponent PCMs for a specific application in either experimental or theoretical ways. In this study, a new approach is made to provide a simple and efficient way to locate ternary salt-water eutectics, which helps find the proper eutectic formulation.

2.3.2 Challenges & solutions

The salt-water eutectic in this study contains inorganic salts that have some inherent issues that make them difficult to applied to energy storage solutions as it is illustrated in Section 2.2.1.2. Therefore, the issues regarding stability, thermal conductivity, supercooling and corrosion are discussed below.

2.3.2.1 Stability

When a new PCM is developed, the chemical and physical stability should only compromise by a minimal degree compared with the existing solutions in extended charging/discharging cycles (Rathod and Banerjee, 2013).

Phase separation is one of the stability issues that hinders the PCM commercialisation. The initiator of phase separation is demonstrated in Figure 2.10. On the red dot line, When the temperature decreases below point C, liquid phase PCM is separated into two different states because of incongruous phase change: solid A which deposits at the bottom under the action of gravity and higher B concentration liquid. Hence the freezing point of the PCM will reduced because of concentration changing after cycling. In addition, phase separation of PCMs will show a reduction of the melting enthalpy after cycling (Mehling and Cabeza, 2008).

Gelling/thickening To form eutectic composition is one of the effective ways to prevent phase separation, which is discussed in Section 2.3.1. Another method is to add gelling or thickening agents into the system to limit the substance movement (Mehling and Cabeza, 2008). Gel is more popular than solution in commercial applications based on product safety consideration. Hence it is necessary to find proper gelling or thickening agents for each PCM system.

Gelling agent is a cross-linked material such as polymer. It constructs a three-dimensional network that holds PCM together; thickening agents means adding additives to increase the viscosity of the materials. Adding thickening agent is reported to be the most effective way to prevent phase separation according to Ryu et al. (1992). The adding of thickening agent can also prevent corrosion to a great extent (Oró et al., 2013). Plenty of hydrocolloids gelling and thicken agents are studied by researchers, for instance, starch, agar, pectin as gelling agents; cellulose derivatives, gum arabic as thickening agents (Saha and Bhattacharya, 2010).

Mitsui (1997) reviewed water-soluble polymer agents for cosmetic applications as shown in Figure 2.14.

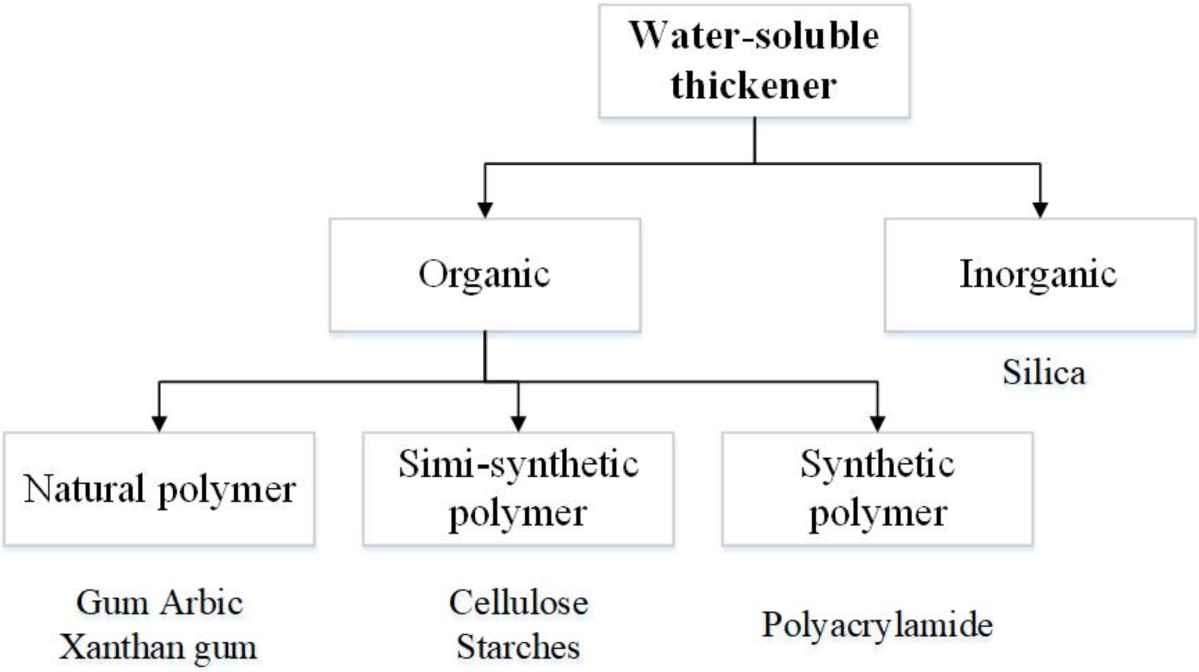

Figure 2.14: The classification of water-soluble polymer agents (Mitsui, 1997)

Li, Wu, and Tan (2012) used sol-gel method to prepare SiO_2 gel and form a stabilised paraffin-SiO_2-expanded graphite composite PCM. They found that the phase change temperature and heat of fusion decreased slightly by adding gelling agent. Gök, Yilmaz, and Paksoy (2006) applied different percentage of polyacrylamide (PAM) and gelatin gels in salt hydrates ($Na_2SO_4 \cdot 10H_2O$) stabilisation tests. The best result that achieved congruent phase change was observed in the sample with 10% agents. Hou et al. (2018) also added polyacrylamide in the $Na_2SO_4{\cdot}10H_2O$ based eutectic composition system. The amount of PAM used was 5%. Other agents, such as carboxymethyl cellulose (CMC) (Dong et al., 2018; Zhu et al., 2017), fumed silica (Shahbaz et al., 2016), sodium alginate (Liang and Chen, 2018), potassium bromide (Gao et al., 2015), etc, were reported by researchers to increase stability of the PCM.

2.3.2.2 Thermal Conductivity

Thermal conductivity is another important factor that needs to be taken into consideration in screening PCMs. It determines the heat transfer conditions in the charging/discharging dynamics. Most of the PCMs available in the market have relatively low thermal conductivity values (0.2∼1 [W/(m K)]). Normally, thermal conductivity enhancement can be achieved either through formulating multicomponent PCMs by adding high thermal conductivity materials (nucleators) or increasing the contact area between PCMs and heat transfer fluids (HTF) (Gasia, Miró, and Cabeza, 2016). Figure 2.15 showed the common enhancement techniques for optimising thermal conductivity of PCMs.

Regarding the organic PCMs, Li et al. (2013b) synthesised the polyethy-

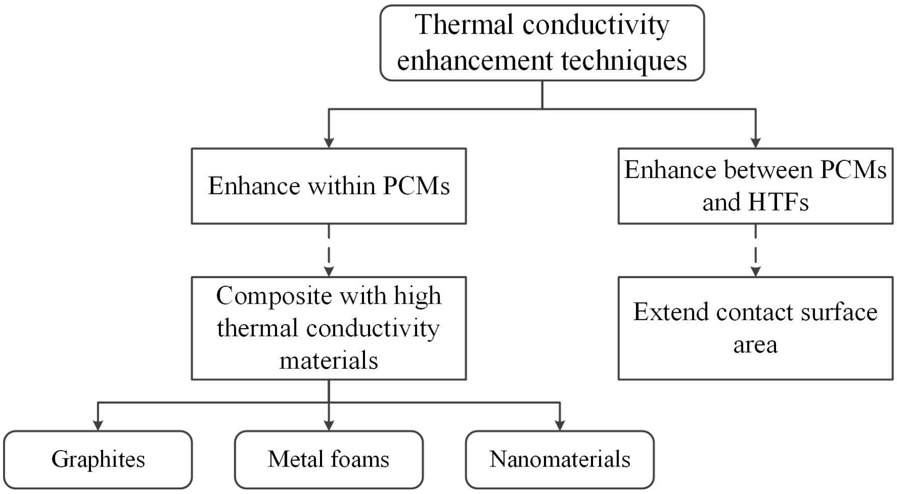

Figure 2.15: The common methods for thermal conductivity enhancement (Gasia, Miró, and Cabeza, 2016)

lene glycol/sulfonated graphene composite PCM to obtain a higher thermal conductivity. The network of sulfonated graphene fillers provide a path for travelling phonons. As a result, with the adding of sulfonated graphene, the value of the thermal conductivity rises further.

Mo et al. (2017) prepared ethylene glycol solution-based nanofluids by introducing 0.1∼0.4 wt% TiO_2 nanoparticle. Results showed that the thermal conductivity of nanofluids was enhanced by TiO_2 nanoparticle considering the acceleration effects of nanoparticle on the growth speed of water crystalloid. The increment of the thermal conductivity is proportional to the amount of nanoparticle added in the fluid. The nanofluid PCMs were developed for subzero applications. TiO_2 nanoparticle could also be added in inorganic PCMs for thermal conductivity increment. He et al. (2012) developed $TiO_2/BaCl_2/H_2O$ nanofluid as a low temperature PCM. The thermal conductivity of PCM is increased by 12.76% at −5 °C with slightly decreased latent heat and specific heat.

2.3.3 Supercooling

Supercooling leads to a lower congealing temperature. It is reported that when the heat transfer fluid decrease 1 °C in charging process, the COP correspondingly decrease by 3% (Lu and Tassou, 2013). Supercooling degree is affected by many factors, for instance, material thermal conductivity or surface roughness of the containers.

Using DSC can not properly characterise milligram-samples' practical supercooling degree, the probability of supercooling is greatly reduced because it is significantly suppressed when the sample is in small amount (Nagano et al., 2004). Hence supercooling can be studied better by T-history method which was developed by Yinping and Yi (1999). In this method, the sample amount is significantly larger than in DSC tests and the phase change process of each PCM samples can be observed clearly and directly.

These are six different T-history supercooling curves during rapid cooling displayed in Figure 2.16 (Grodzka et al., 1969). Different from Figure 2.5, practically, the crystallisation point of some curves does not lie on the phase change temperature T_m. Instead, the nucleation occurs at a lower temperature

T_s.

Both Figure 2.16 (a) and (b) represent the basis of one-phase supercooling. They have a same supercooling degree til T_s. The spontaneous solidification begins at the wall surface of the container, then the crystallisation rate depends on the thermal conductivity of the material. Since the temperature of Figure 2.16 (a) takes longer time to rise to freezing point T_m, in other words, the supercooled liquid state remains longer, it has a lower thermal conductivity than Figure 2.16 (b).

Figure 2.16 (c) is either for pure or multi-phase materials. The temperature does not rise up to T_m but has a relatively low temperature during the nucleation. It is due to the poor crystal growth rate. The heat generated by the crystallisation process is slower than liberated in this "kinetic controlled" state.

There is no supercooling presented in Figure 2.16 (d). The temperature at first decreased to T_m and then went below the freezing point before the solidification completed. This is possibly interrupted by the rapid heat removal or an insufficient sample amount. In this case, the sample weight, the location of the thermocouple and the cooling rate of the thermostat bath need to be taken into account. Also, Two-phase supercooling might have happened as well. In addition, convection can effect the maintaining of the early plateau.

It is negligible in the solidification process.

Figure 2.16 (e) and Figure 2.16 (f) present low thermal diffusivity in the liquid phase and solid phase, respectively.

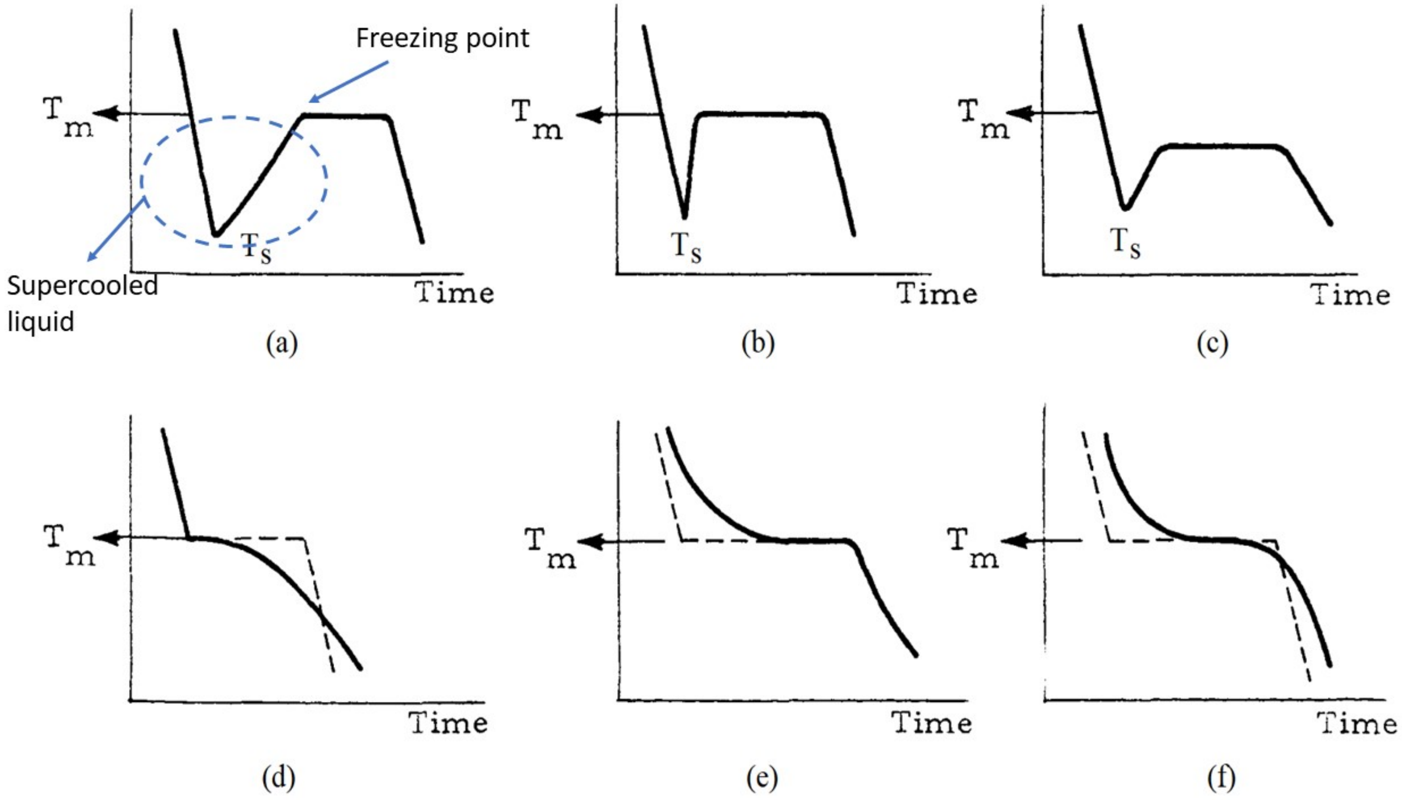

Figure 2.16: The different performance of T-history curve of PCMs (Grodzka et al., 1969)

The supercooling degree can be reduced or eliminated based on various triggering mechanisms, such as, contacting with supercooling substrate, electrical and mechanical methods (Beaupere, Soupremanien, and Zalewski, 2018). Among them, adding particles is the most reproducible technique. The particle can be either a same (seeding) or foreign material (nucleating agent) type. Seeding is the easiest way to facilitate the heterogeneous nucleation (Safari et al., 2017). However, it is hard to keep crystal of the seeding substrate solid in phage change process.

Nucleating agents have gained tremendous attention among researchers for years. The supercooling reduction by introducing nucleating agents is affected by the agent type, concentration, particle size and formulating procedure.

Ryu et al. (1992) performed extensive study on nucleating agents for inorganic salt hydrates, as shown in Table 2.6. The result shows that the adding of the nucleating agents improves the nucleating rate effectively. The degree of influence varies with the PCM-agent combinations.

In He et al.'s study, TiO_2 helped reduce the supercooling of $BaCl_2$ aqueous solution. The samples were immersed in the HTF in the thermostatic bath and the temperature was measured by thermocouples. Figure 2.17 showed the results of the supercooling degree and time decrement by adding TiO_2 nanoparticle. With the increasing of nanoparticle volume fraction, the

Table 2.6: The effect of the nucleating agent on the supercooling degree of PCMs

PCM	Tm(°C)	Nucleating agent	Supercooling (°C)	
			- nucleator	+ nucleator
$Na_2SO_4 \cdot 10H_2O$	32	Borax	15-18	3-4
$Na_2HPO_4 \cdot 12H_2O$	36	Borax	20	6-9
		Carbon		0-1
		TiO_2		0-1
		Copper		0.5-1
		Aluminium		3-10
$CH_3COONa \cdot 3H_2O$	46	Na_2SO_4	20	4-6
		SrSO4		0-2
		Carbon		4-7
$Na_2S_2O_3 \cdot 5H_2O$	57	K_2SO_4	30	0-3
		$Na_2P_2O_7 \cdot 10H_2O$		0-2

supercooling degree was further decreased (He et al., 2012).

Li, Pan, and Ying (2011) examined the effect of different nuclear agents on the supercooling degree of NaCl solution and KCl solution as temperature regulator in food storage. Results show that both SiO_2 and CuS have good performance in reducing the supercooling of KCl solution. For NaCl solution, borax is a better choice. With 3% borax, the supercooling of NaCl solution reduced ∼5 degree.

Nagano et al. (2003) did a comprehensive experiment on the effect of different supercooling agents on $Mn(NO_3)_2{\cdot}6H_2O$ system. Among 34 chlorides, nitrates, sulfates, fine powders and solvents, $MnCl_2{\cdot}4H_2O$ is the most effective additive of supercooling reduction. It also has a significant influence on

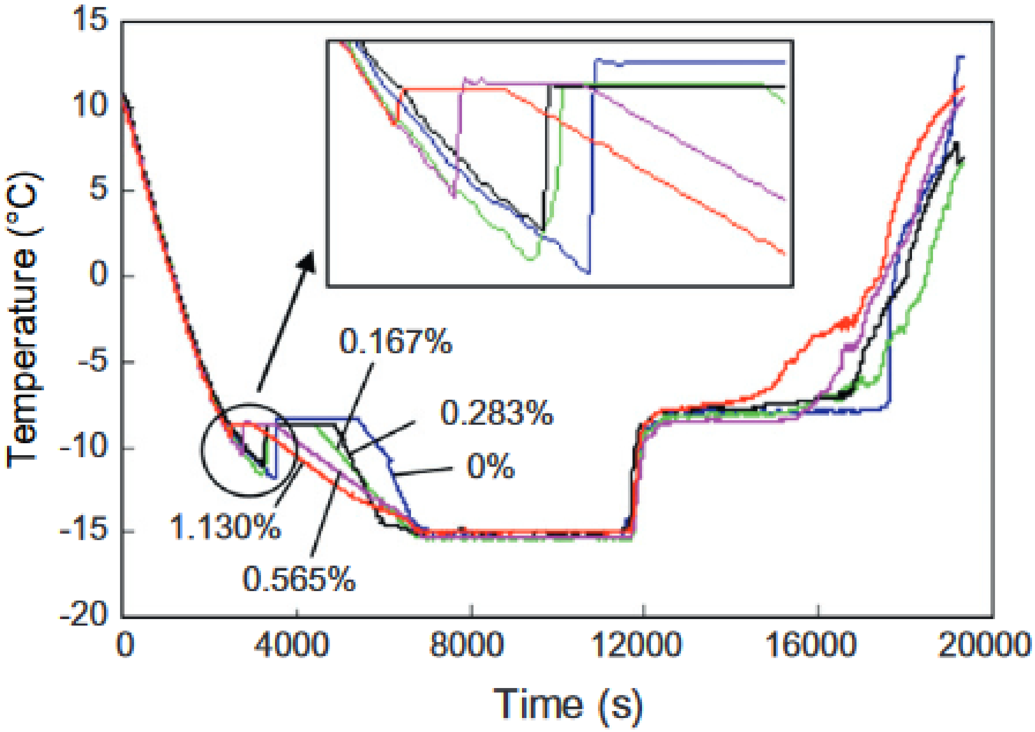

Figure 2.17: The effects of supercooling degree by adding TiO_2 into $BaCl_2$ aqueous solution

the phase change temperature and latent heat of the PCM. Although, with those research above, it has not been concluded that how the amount of nucleating agents affects the supercooling (Beaupere, Soupremanien, and Zalewski, 2018).

Nucleating agents that with a similar crystal structure to the PCM attract a lot interests. Ushak et al. (2016) studied the nucleation capacity of five nucleating agents on bischofite ($MgCl_2{\cdot}6H_2O$). They came up with a conclusion that the lattice of the crystal structure is the most important factor on nucleating agent screening. The solubility, chemical structure and the crystal system of agents make little influence in supercooling reduction. However, the adding of the agent reduces the latent heat of the PCM by displacing the active component during phase change transition (Hirschey et al., 2018).

2.3.3.1 Corrosion

The compatibility of PCM with container material is an important factor for PCM utilisation. The ionic chemical reaction may occur between salt based PCM and metal containers while oxygen is present. In this case, the oxidation experiment needs to be done in the process of screening PCM container. The sample preparing, cleaning and evaluating corrosion standard are followed by ASTM G1-03 (2017).

The corrosion rate (CR) can be calculated by mass lost per day per square meter (Cabeza, 2008):

$$\Delta m = m(t_o) - m(t), \qquad \text{(mg)} \tag{2.5}$$

$$CR = \frac{\Delta m}{A(t_o - t)}, \qquad (\text{mg/cm}^2\text{year}) \tag{2.6}$$

$$\Delta m(\%) = \frac{Mm(t_o) - m(t)}{m(t_o)} 100 \tag{2.7}$$

where, $m(t_o)$ is the initial mass of the sample; $m(t)$ is the sample mass after immersed for a certain time length t; A is the sample area.

Many corrosion studies have been performed for high temperature applications. Regrading the low temperature, people have gradually been focused on the corrosion issue in the last ten years.

Krishna and Shinde (2017) summarised the step by step methodology of testing the metal corrosion rate of low temperature phase change materials. The 30mm x 10mm x 1.5mm rectangular copper metal sheet was first pretreated with abrasive paper and rinsed with water and acetone, then immersed completely in paraffin sample for 10, 30, 60 days respectively at 80 °C. Then the metal went through chemical cleaning and gravimetric analysis based on ASTM G1 standards. At last, surface of the metal was observed by SEM.

$CaCl_2 \cdot 6H_2O$ is a promising material for power plant air-cooled condensers. Ren et al. (2017) exposured $CaCl_2 \cdot 6H_2O$ to copper, carbon steel and two kinds of aluminium for up to 16 weeks. Each set of metal was prepared in 50.8 mm x 12.7 mm x 1.6 mm, cleaned and weighted precisely. They set up three temperature range (30 °C, 50 °C, and 80 °C) for corrosion rate calculation and also evaluated the effect of corrosion rate by surface pitting and PH that pitting is temperature depended, each metal responds differently with pH increase.

Honcova et al. (2017) tested the compatibility of $Mg(NO_2)_2{\cdot}6H_2O$ with aluminium alloy container. They chose aluminium tubes(10.0 mm outer diameter x 8.0 mm inner diameter x 10mm) instead of sheets. Temperature was set close to the melting point of PCM at fist, and then simulating the cooling/heating cycles for 1179 h. the Cleaning process was following ISO 8407 standard. It is proven that aluminium alloy can be a good construction material for $Mg(NO_2)_2{\cdot}6H_2O$.

For food processes, Oró et al. (2013) researched on the corrosion performance of low temperature PCMs with common metal and polymer containers. 9 PCMs including 3 commercial products and 6 chloride salts were tested at ambient temperature (22 °C) for 1 week, 4 weeks and 12 weeks on 12 mm x 75 mm x 2 mm metal blocks under standard practice ASTM G1-03. Result showed that the selected low temperature PCMs have no obvious corrosion effect on polymers and 316 stainless steel, while copper, carbon steel and aluminium are not recommended to contain the PCMs. The following year, Moreno et al. (2014) followed the same test procedures for salt hydrates PCMs in the heat pump system in heat and cooling applications. Same metal samples were cut into 50mm x 10mm x 0.5mm plates, cleaned and immersed by PCMs in glass test tubes. Sames were stored in 22 °C and 60 °C correspondingly regarding heating and cooling conditions. Finally different recommendation for each PCM were given according to the visual phenomena and corrosion rate curve.

Ferrer et al. (2015) studied the chemical capacity test with five metals and four PCMs for building applications. The metal size used was approximately 50 mm x 1 mm x 1 mm. Experiments were carried out at 38 °C for 1, 4 and 12 weeks to calculate the corrosion rate. The recommended standard was "*Corrosion prevention and protection: practical solutions*" (Ghali, Sastri, and Elboujdaini, 2007) that if the corrosion rate <0.9, the metal was recommended for long term service with specific PCM.

Hence there is no fixed specifications and time length for corrosion test. Temperature is set according individual applications with liquidus temperatures for PCM.

The evaluation standard of the metal selection in the industry is shown as follow (Oró et al., 2013):

Table 2.7: The evaluation guide of the metal selection in industry

mg/cm^2 yr	mm/yr	Recommendation
>1000	2	Generally unsatisfactory
100 - 999	0.1 - 1.99	Satisfactory for limited monthly service
50 - 99	0.1 - 0.19	Satisfactory for limited yearly service
10 - 49	0.02 - 0.09	Satisfactory for caution use, based on the specific application
0.3 - 9.9	-	Satisfactory for long term service
< 0.2	-	Satisfactory for long term service; No corrosion was evidenced

2.4 Theory and numerical modelling

2.4.1 Cooling load calculation

The cooling load calculation is essential for optimising the cooling system. It can be calculated either in steady state or dynamic state. The static load models represent the cooling load by time-invariant values under extreme conditions, whilst the dynamic load models are based on the static model but comprehend the empirical data dynamically with hourly profile, such as the ambient temperature, relative humidity (RH), solar radiation energy and transient heat released from PCM, etc. A similar accuracy of ∼90% is anticipated by using both models according to Foster et al.'s research (Foster et al., 2013). Therefore, in this study, the static cooling loading calculation is applied to understand the energy consumption within the refrigerated vehicle. Although all sources of cooling load need to be considered in the calculation, it is impractical to include all factors. Hence the deviation of the result is inevitable (Erol, 1993).

The considered cold loads and the assumptions vary at different circumstances as illustrated in Table 2.8.

The sources with the most influence in the cold load calculation can be broken into five components: the transmission load (radiation effects),

Table 2.8: The heat sources calculated by different researchers

Condition		Calculation*	Reference
Cold room	Chilling	$Q_t + Q_i + Q_p + Q_m + Q_m + S$ (10%)	(Akdemir, 2008)
		$Q_t + Q_i + Q_p + Q_r + S$ (10%)	(Raj and TK, 2018)
		$Q_t + Q_i + Q_p + Q_r + Q_m$	(Evans et al., 2014)
		$Q_t + Q_i + Q_p + Q_r + Q_m + S$ (10-15%)	(Sakare, 2014)
		$Q_t + Q_i + Q_r + Q_p + Q_m + S$ (10%)	(MRao, 2015)
Container	Chilling	$Q_t + Q_i$	(Huang and Piontek, 2017)
Vehicle	Freezing	$Q_t + Q_i + Q_r + Q_m$	(Liu, Saman, and Bruno, 2014)
		$Q_t + Q_i + Q_p + Q_m + S$ (25%)	(Sharma and Buddhi, 2013a)

*Q_t: Transmission load
Q_r: Radiation load
Q_i: Infiltration load
Q_p: Product load
Q_r: Respiration load
Q_m: Miscellaneous load
S : Safety factor

infiltration air load, product load, miscellaneous load (internal load and equipment-related load) and the safety factor (ASHRAE, 2014b).

The transmission load is related to the materials and construction of the walls, the refrigerated space and surface area, the air motion and the temperature difference between the container and ambient air. Some researchers have calculated the transmission load through walls, roof and floor separately based on the different constructing materials and radiation conditions. According to ASHRAE (2014b), The radiation effect can conveniently be compensated by adding a few degrees to the ambient temperature in the transmission load calculation in most cases.

The infiltration load indicates the air loss which is due to the density or pressure differences between the cold air and ambient air through the cracks and small gaps of the vehicle's exterior surfaces. The infiltration load and associated equipment load account for more than half of the total refrigeration load of the warehouse related applications (ASHRAE, 2014b). There are various empirical models to help predict the density difference based infiltration load. As regards to Foster et al.'s investigation (Foster et al., 2003), the model developed by Gosney and Olama (GOSNEY and QLAMA, 1976) provides the most accurate prediction of the fully established flow within experimental error for cold room. This model is further quoted in *ASHRAE Handbook-Refrigeration* for a fully established flow (ASHRAE, 2014b). The pressure difference based infiltration flow, however, when exposed to wind or under mechanical air exhaust, uses the direct flow equation for correlation. Different assumptions were made by searchers for the air velocities calculation (ASHRAE, 2014b; Çengel and Ghajar, 2011; Kharagpur, 2016), which will be discussed in Section 6.1.

Miscellaneous load is composed of of internal load and equipment related load. The internal load represents all electrical energy dissipation such as heat gain by fan motor, lights and human occupancy. Equipment related load is the heat generated by refrigerating equipment, for instance, the heat for forced-air circulation and defrost. They are both determined by the operating conditions.

The product load consists of the heat removed from the perishable food/vegetable and the product respiration for a chilling scenario. It varies widely according to the type of commodity and can be neglected in pre-cooled frozen products (Çengel and Ghajar, 2011). safety factor is generally 10% to 25% of the total heat energy load. *ASHRAE Handbook-Refrigeration* provides a comprehensive induction on the refrigerated facility loads.

2.4.2 Modelling

The temperature distribution that plays an important role in keeping a homogeneous environment inside the container has significant impact on the quality of the transported goods. Because of the cost and technique issues (Patankar, 1980), the temperature distribution is difficult to measure based on empirical data. Therefore, there are some numerical approaches to investigate the heat transfer in refrigerated applications. Computational fluid dynamics (CFD) method is emerged as a preferred tool which provides a wealth of details (Moureh, Menia, and Flick, 2002).

According to Tassou, De-Lille, and Ge's research (Tassou, De-Lille, and Ge, 2009), the frequent door opening is the major cause of the energy dissipation. It is reported that the adding of air curtain efficiently minimises the temperature fluctuation along the doorways (Tso et al., 2002). Hence various studies have been focusing on the performance of the air curtains in recent years.

For instance, Liebers et al. (2017) investigated the heat loss reduction by installing air curtains in buses. A major reduction of the energy loss was achieved for more than 20 seconds. Ye et al. (2017) studied the performance of the air curtain on a large space building. The use of air curtain reduced the air infiltration and maintained the indoor heat comfort. The computational fluid dynamics (CFD) numerical simulation has been employed to study the airflow patterns. In the refrigeration applications, Cao et al. (2010) proved that introducing the air curtain into the open vertical refrigerated display cabinets decreased the cooling loss by 19.6% and the energy consumption by 17.1%. Similarly, Zhijuan et al. (2013) found that the velocity of air curtain is inversely proportional to the goods temperature in display cabinet by running 2-D CFD simulations. Belleghem et al. (2012) carried out a CFD simulation on the vertical single-jet air curtains in room. They evaluated the impact factors of the air curtain and found out that the outlet momentum is the major one. In an optimal condition, air curtain helps reducing the heat transfer of the cold room to 20%. Laguerre et al. (2014) investigated the effects of the input variables and equipment parameters on cold-chain applications. Results showed that increasing the turbulence of the air curtain will reduce the load temperatures and increase the energy consumption. Liang et al. (2015) established a 3-D CFD model with a velocity of air curtain from 0 m/s to 4 m/s. It is suggested that air curtain can help reduce the heat loses within a proper velocity range. However, When the value of velocity is higher than a certain value, it will aggravate the air circulation and increase energy consumption. Unfortunately, few studies have focused on the effects of the air curtain under different circumstances or optimising the air curtain design based on refrigerated vehicle. Hence in this study, different working conditions are considered when calculated the performance of air curtain. Not only the airflow velocity, but also the influence of nozzle width and jet angle on the door opening are also studied.

2.5 Summary

It is suggested that temperature controlling is essential for the refrigerated transportation. Varies refrigeration cooling systems are applied in current refrigeration market. Three mainstream cooling system were discussed and compared, which include vapour compression system, cryogenic cooling system and eutectic system. The eutectic system that employs phase change material calls attention because of its decent isothermal behaviour and versatile application scenarios.

The implement of eutectics is a latent heat storage technology, which is part of TES. TES consists of sensible heat storage, latent heat storage and thermochemcial storage. The advantage and disadvantage of three techniques were discussed. Latent heat storage material, also called PCM, was studied. The selecting criteria, classification and available commercial cases are reviewed. For -25$\sim-45\,°$C and -33$\sim-45\,°$C refrigerated transportation specifically, several PCM candidates were screened. The main characteristics of PCM were listed and surrounding methodologies by researchers were summarised.

Based on refrigeration application, the cooling load calculation and CFD modelling were introduced. One for understanding the energy demand of refrigerated vehicle and the other is for simulating the air distribution within vehicle container. The theory behind was explained as well as relevant research.

However, study on PCMs for subzero energy storage applications is far from conclusive. In contrast to the ever expanding demand for subzero energy storage applications, PCMs with favourable thermophysical properties are seldom researched. Furthermore, the thermophysical properties of the commercial products on the market is not competent enough in many cases because of its low energy density. PCMs with favourable thermophysical properties that suit the temperature range are in need, For instance, a high latent heat, low supercooling degree and enhanced thermal conductivity, etc.

The impact of thermal load and product loading on the energy dissipation is studied mostly based on stationary applications such as refrigerated cabinet. Because the operation environment and condition between stationary and mobile applications are different, the impact on vehicles should be studied specifically to provide a better understanding of the energy dissipation of refrigerated vehicles.

This PhD study is therefore focused on locating suitable PCM candidates for established refrigerated temperature range, thermoproperties characterisation and optimisation. In addition, investigating the thermal load and product loading effect on refrigerated vehicle.

CHAPTER 3

MATERIAL & METHODS

This chapter explains the methodology in this study for both experimental and theoretical perspectives. This chapter is divided into three sections. Section 3.1 presents the thermophysical characterisation techniques with corresponding instruments. Section 3.2 introduces the chemicals used and material preparation techniques. Section 3.3 explains the details of mathematical models, analysis principles and parameters.

3.1 Characterisation techniques

As discussed in the previous section, pure PCMs or binary eutectics are widely addressed in the literature. However, sometimes they cannot meet the temperature demand of a certain application and the corresponding PCMs have yet to be discovered, hence ternary PCMs are studied in order to meet the requirement and get a better performance. Double decomposition reaction will occur when a material causes parts of the other ionic elements exchange and form new compound. To acquire a stable ternary system, the double decomposition reaction needs to be avoided when adding the third material. Thus a proper base PCM and addition PCM candidate should carry following profits:

- Soluble in the solvent at aiming temperature;
- Chemical stable and relatively cheap;
- A higher phase change temperature than desired temperature;
- Same cation or anion of two PCMs;
- A relatively higher fusion heat

To characterise and analyse these thermophysical properties of samples, various techniques are implemented with the help of the equipment listed in Table 3.1. The instruments are well calibrated before testing. Besides, each experiment was conducted multiple times to reduce the bias error. The principles of the main techniques will be discussed in the following section.

Table 3.1: Equipment employed in the experiment

Instruments	Function	Manufacture
Differential Scanning Calorimetry (DSC)	Phase change temperature Latent heat, specific heat	Mettler Toledo
K type thermocouple		TC Direct
Laser Flash Apparatus (LFA)	Thermal conductivity	Netzsch
TA dilatometer	Cycling stability	Anton Paar
Thermostatic bath	Supercooling	Huber
Reometer	Viscosity	Anton Paar
X-ray diffraction (XRD)	Crystal structure	Siemens
Digital weighing balance	Weight	Mettler Toledo
Ultrasonic bath/ Magmatic stirrer	Dispersion	Fisher Scientific
Density meter	Density	Anton Paar
3D printer	Model building	Formlabs

3.1.1 Phase change temperature & latent heat

Differential Scanning Calorimetry (DSC) plays a critical role in thermoanalytical research. As illustrated in Figure 3.1, the same gas atmosphere is set on both sides of the furnace. Before the characterisation, a blank experiment normally runs first with the identical program and the same crucible type as a background curve. Then, sample is placed in the Al_2O_3 sample pan aside with the reference pan. They are heated simultaneously by the furnace. The dynamic signals of heat flux of both sample and reference are detected with heat flux sensor. 3 tests for each sample are carried out to obtain a repeatable and representative results. The cooling temperature range is from ambient temperature to -75°C depending on the crystallisation temperature of the sample. Since the value of the latent heat is affected by the heating rate and sample mass of DSC testing (Boettinger et al., 2011), accordingly in this study, the cooling rate of all tests is set of 5°C/min, sample mass was ~1 mg. Instrument error in DSC is typically ±0.5 °C~1 °C.

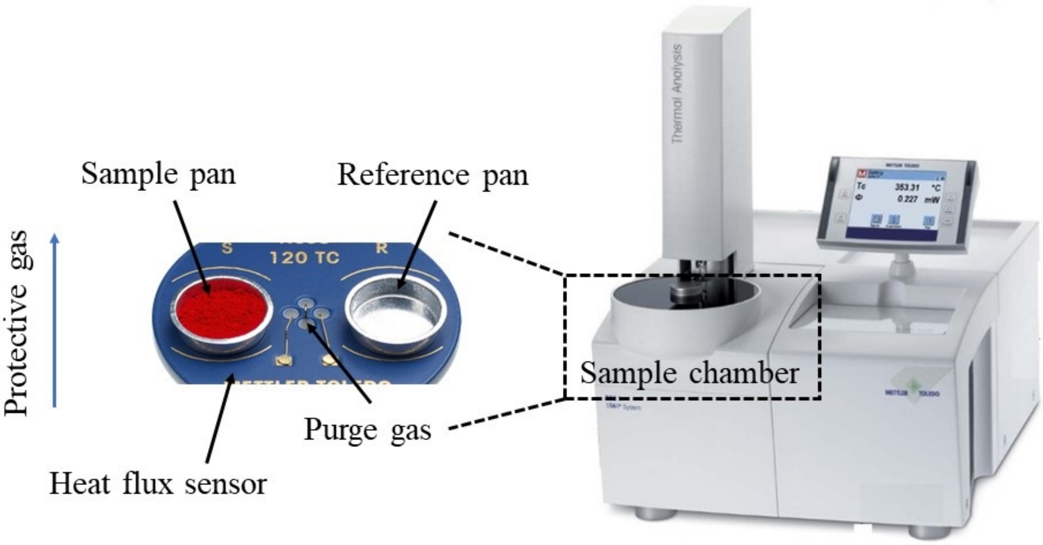

Figure 3.1: The schematic diagram of DSC chamber

Figure 3.2 shows a typical DSC curve of a complete solid-liquid-solid phase change process of the sample. The endothermic peak and exothermic peak are corresponding to the sample melting and crystallisation process, respectively. It detects the phase change temperature of the sample and indicates the latent heat by integrating the amount of heat absorbed or released per unit sample during phase transition.

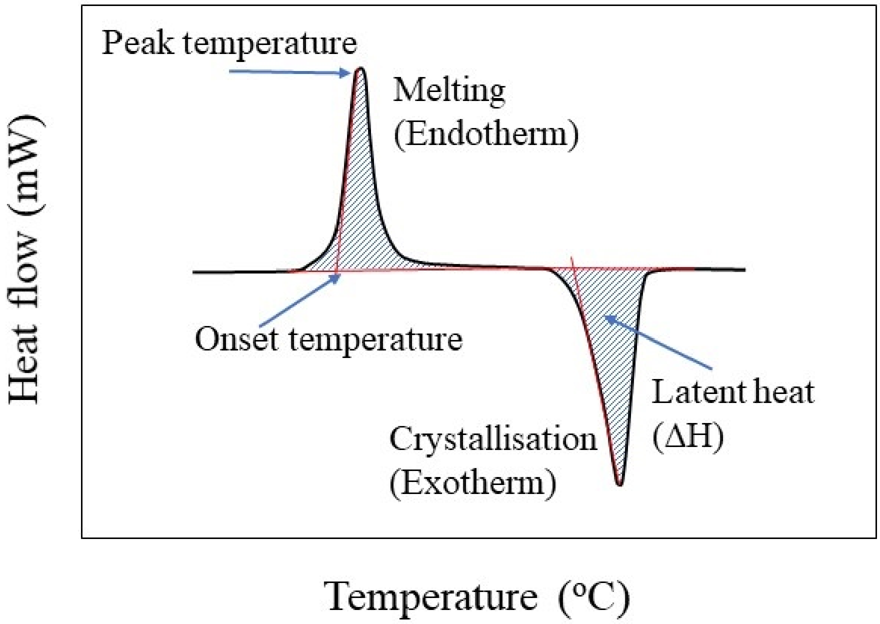

Figure 3.2: The typical DSC curve of phase change process

For measuring the phase change temperature and phase change behaviour, two points are analysed: the peak temperature and onset temperature. If the studied sample is pure or a eutectic system, the phase change curve shows a single symmetry peak. In some cases, the DSC peak shifts with the change of the heat rate or sample weight as illustrated in Figure 3.3. It is suggested that the peak value of the melting temperature affects the heat rate and sample weight significantly. In general, a more rapid temperature change or a larger sample mass will result in a broader melting curve. However, the intersection of the tangents of the peak, otherwise stated as the onset temperature, is remained unchanged. Hence the onset temperature is served as the phase change temperature of the sample. In some cases, when the peaks are too broad, the peak temperature is more precise to determine the phase transition (Toledo, 2010).

3.1.2 Specific heat capacity

DSC can also measure the value of specific heat capacity of samples. The specific heat capacity ($\mathrm{C_p}$) is the amount of heat needed of one unit of mass of the sample to rise the temperature by 1 degree. The METTLER TOLEDO DSC 2+ uses sapphire method for the sample $\mathrm{C_p}$ determination. Three measurements are required in sapphire method: blank, sapphire and sample measurements. Based on the correction by blank curve, the $\mathrm{C_p}$ value of the sample is compared and calibrated by the $\mathrm{C_p}$ of the sapphire.

3.1.3 Thermal conductivity

Different approaches have been made to perform the thermal conductivity measurement such as steady-state or transient methods. However, each of these techniques has their own advantages and disadvantages as well as its inherent instrument limitations (Palacios et al., 2019).

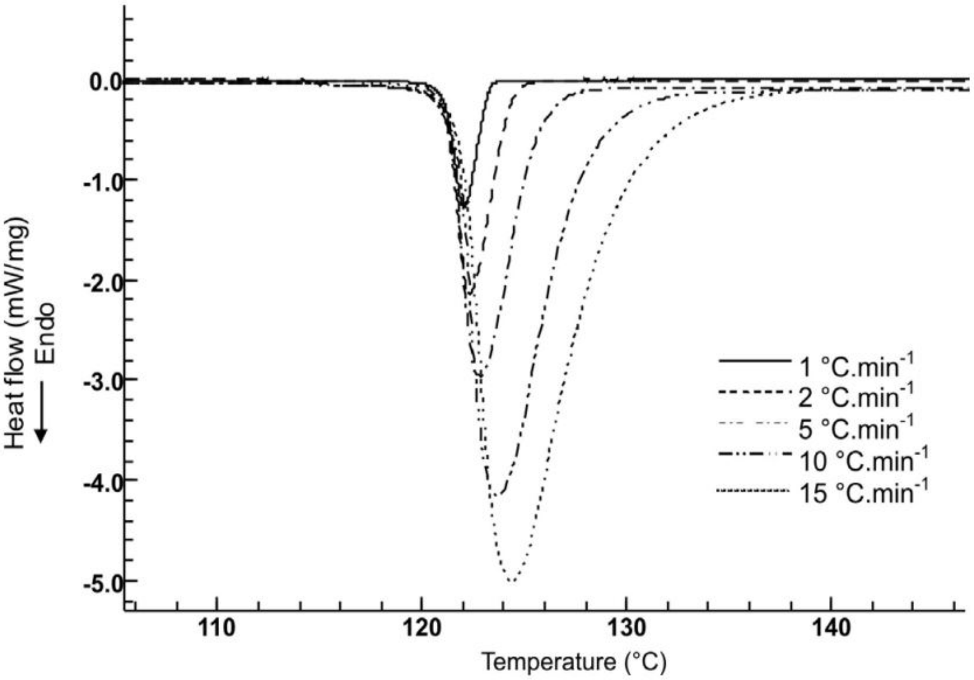

(a)

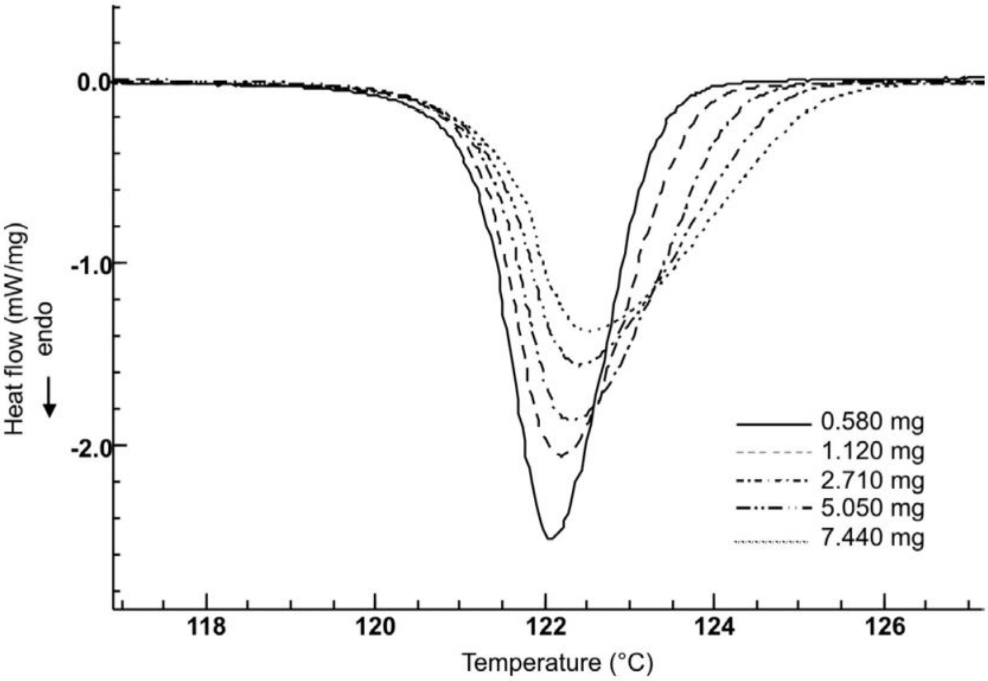

(b)

Figure 3.3: The DSC curve shifting due to (a) changing heating rate (b) different sample weight (Araújo et al., 2010)

Laser flash method measures a wide temperature range from $-120\,^{\circ}\mathrm{C}$ to $2800\,^{\circ}\mathrm{C}$. It is accurate, easy handled, and capable of measuring the thermal conductivity of small solid, liquid or powder samples. The schematic diagram of NETZSCH LFA 427 is shown in Figure 3.4.

The LFA tests are conducted at ambient temperature. The absolute accuracy of the LFA method is $\sim$3%. 5 individual measurements were taken per temperature in each test for improving accuracy. Liquid samples were placed in a Pt/Rh holder with a diameter of 12.7 mm and a thickness of 0.505 mm. Graphite coating was required on both top and bottom surfaces of the holder to achieve a homogeneous entry and release of energy of the samples. During the measurement, the laser pulse by a laser beam source hits the bottom of the plane sample. Then the temperature change at the top of the sample is monitored by infrared sensor as a function of time. Accordingly, thermal diffusivity along the thickness dimension of the sample can be obtained from relative temperature increase.

Thermal diffusivity is computed by:

$$\alpha = 0.1388\frac{x^2}{t_{0.5}} \tag{3.1}$$

Where x is the sample thickness and $t_{0.5}$ is the time value at half temperature increase (signal height) as illustrated in Figure 3.5.

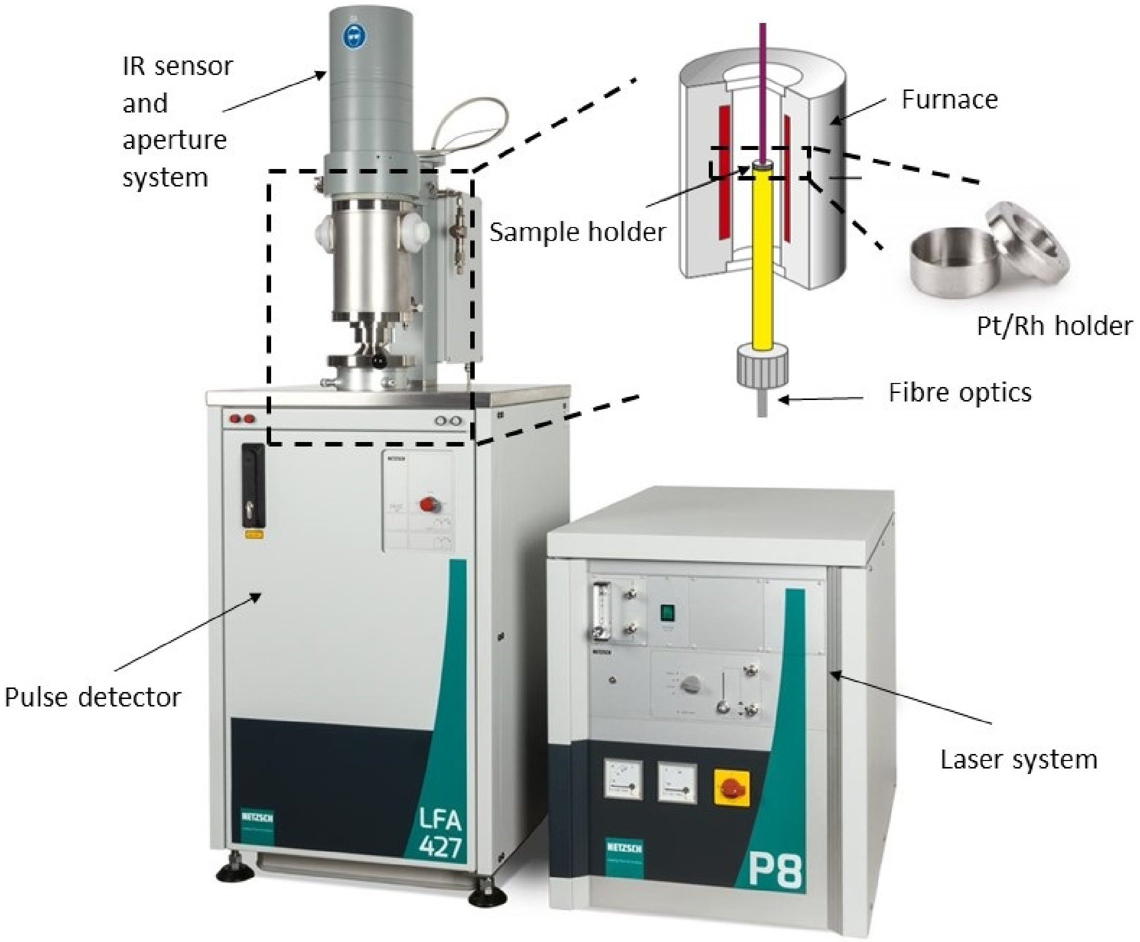

Figure 3.4: The schematic diagram of LFA

And then, the thermal conductivity of sample λ is calculated by Equation 3.2.

$$\alpha = \frac{\lambda}{\rho C_p} \tag{3.2}$$

Where, α is sample thermal diffusivity, ρ and C_P are the density and specific heat of sample, respectively.

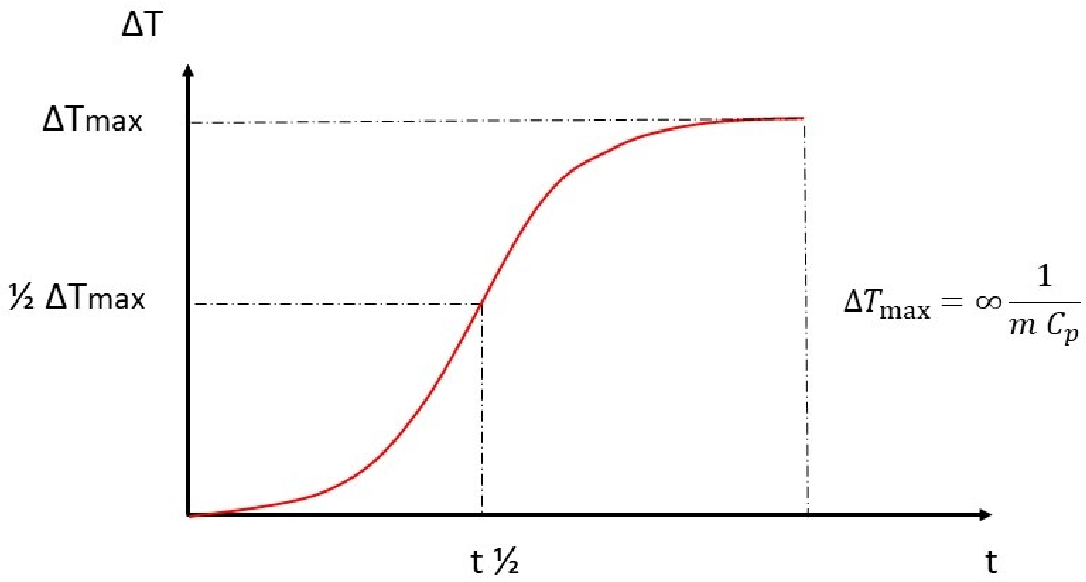

Figure 3.5: The LFA measuring curve of time and relative temperature increment

3.1.4 Supercooling

As shown in Figure 3.6, the T-history method was performed in a temperature controlled thermostatic bath cycling with cooling agent whose phase change temperature was lower than studied temperature range, silicon oil in this case. Samples were held in a 50 ml conical plastic tube and the weight of the sample is 10 g. Plastic tubes are fixed on the tube rack to ensure that the samples can be fully immersed in the cooling agent. The isothermal temperature for cooling the material is −40 °C, samples were crush cooled to −40 °C in the thermostat bath and exposed in the air during heating process. The temperature change of the samples was measured by thermocouples. They were located at the central cylinder, same position of each samples. The fully charging/discharging process was conducted 3 times for a stable T-history profile. The voltage signal was received every 20 s and was sent to the control computer.

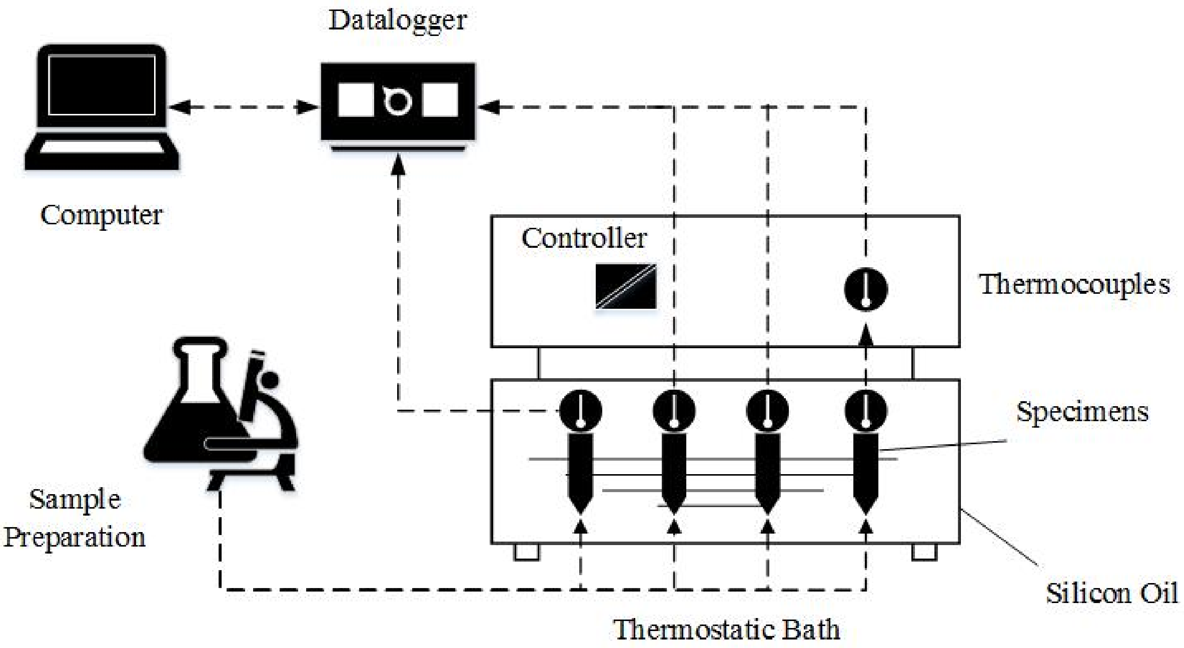

Figure 3.6: The flow chart of T-history method

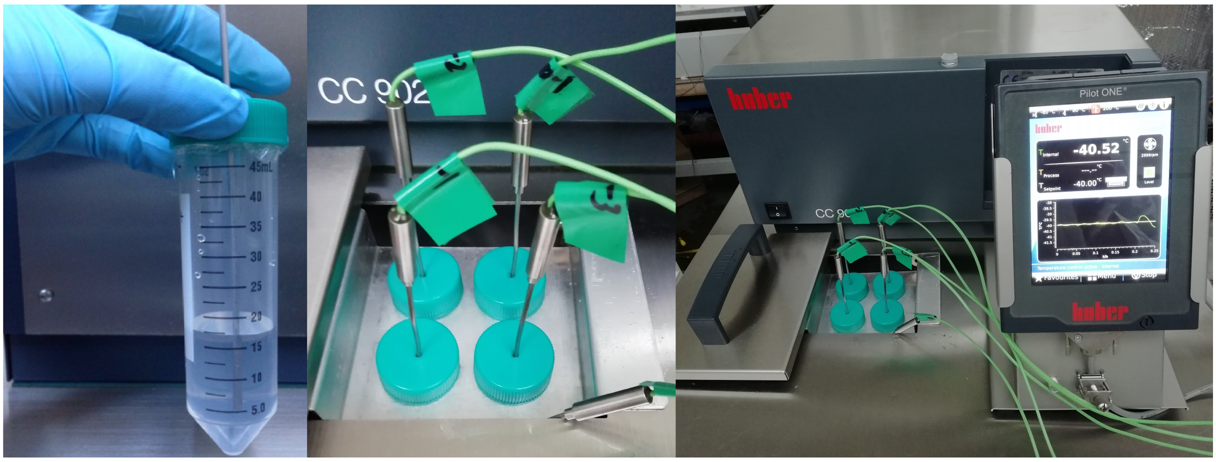

Figure 3.7: The set up of T-history experiment

Figure 3.7 displays the photographs during T-history measurement. Thermocouples applied in the experiment is 2 mm radius and well calibrated with 6th order polynomial fitting in advance. The measurement error is within ±1 °C. In order to fix the testing tubes and thermocouples, a tube rack and two thermocouple holders were created correspondingly, as presented in Figure 3.8. The tube rack was made by stainless steel plate and thermocouple holders were built by 3D printer after measuring the dimension of the thermocouple and tube. It has been proven that the latter holder hold the thermocouple better. It also saves printing material.

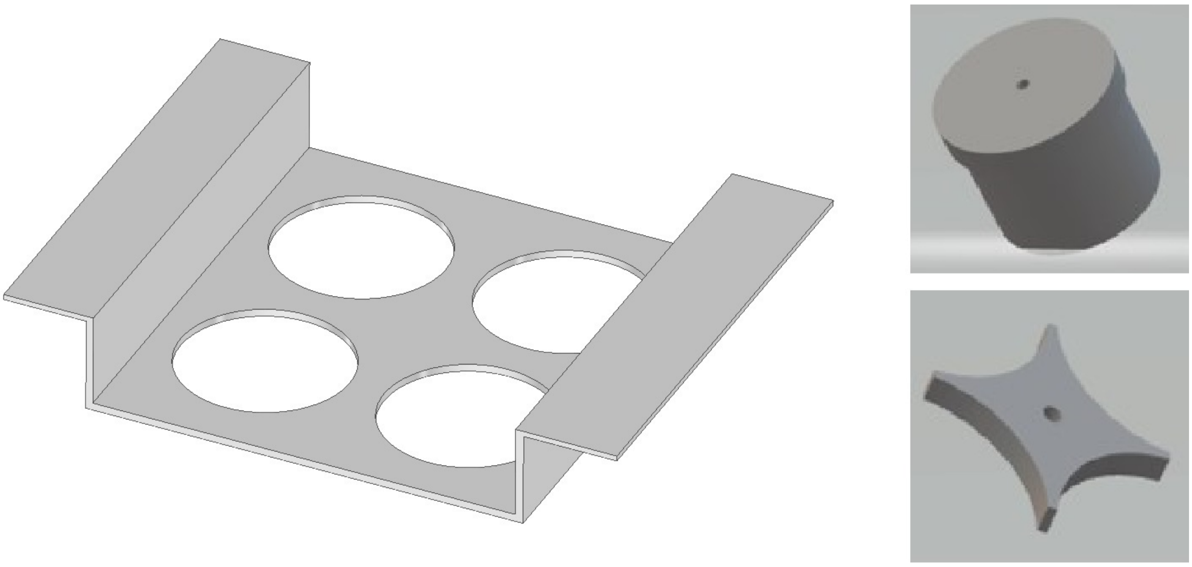

Figure 3.8: The stopper shaped (a) and star shaped (b) holder designed for the thermocouple fixing

3.1.5 Corrosion

The procedure for the corrosion test is following ASTM G1-03 (2017). Four different metals: stainless steel 316, stainless steel 304, aluminium and copper

K65 were cut into 30 mm x 10 mm x 1 mm metal plate. Before the corrosion test, the metal plates were pre-cleaned by acetone for removing oily stain on the surface. 3 metal plates were tested in each group for the reliability check. Metal plates were weighted and fully immersed in 100 g studied solution at ambient temperature for 7, 28, 84 days respectively. Then they were took out, cleaned and weighted again. The weight loss of metal plates after different time periods were evaluated by the analytical balance with precision of ±0.1 μg before and after the corrosion test. The estimated data used is based on the average results of each group.

3.2 Material Preparation

3.2.1 Chemicals

Inorganic salts that are used in this study, as is discussed in Section 2.2.3, are among the most favourable candidates for cold storage applications because of their thermophysical properties and stability.

Other reagents used in this study include distilled water, nucleating agents and water-soluble gelling agents. The distilled water is produced by water still equipment. Most of the chemicals used in this study were of high purity analytical grade ($\geq$ 98%), purchased from Sigma-Aldrich. Further details are

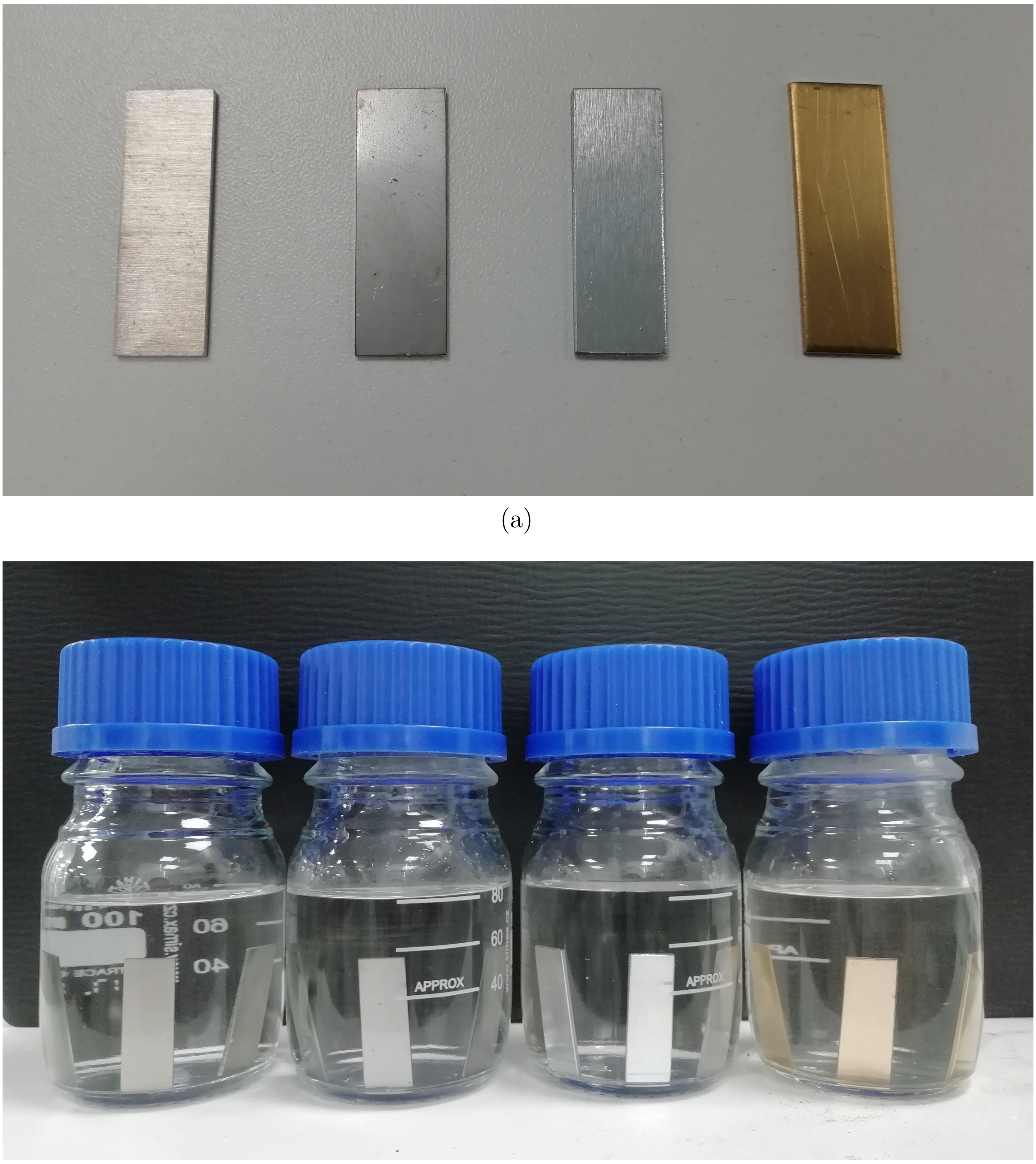

(a)

(b)

Figure 3.9: The set up of corrosion experiment. From left to right is stainless steel 316, stainless steel 304, aluminium and copper K65, respectively

shown in the Table 3.2.

Table 3.2: Chemicals data in this study

	Ingredients	Formula	CAS number
Inorganic salts	Sodium Chloride	$NaCl$	7647-14-5
	Ammonium chloride	NH_4Cl	12125-02-9
	Potassium chloride	KCl	7447-40-7
	Sodium sulphate	Na_2SO_4	7757-82-6
	Magnesium chloride	$MgCl_2$	7786-30-3
Nucleating agents	Borax	$Na_2B_4O_7 \cdot 10H_2O$	1303-96-4
	Diatomite earth	SiO_2	68855-54-9
	Fumed silica	SiO_2	112945-52-5
Gelling agents	Xanthan gum	-	11138-66-2
	Carboxymethyl cellulose (CMC)	-	9000-11-7
	Starch	$(C_6H_{10}O_5)_n$	9005-25-8
	Polyacrylamide	$(C_3H_5NO)_n$	9003-05-8

3.2.2 Preparation

A typical 3D phase diagram is presented in Figure 3.10, where the temperature decreases towards the centre of the phase diagram. The ternary eutectic point lays at the lowest point of the ternary system. Each binary system is directed into the ternary points through the boundary curves.

In this case, two binary systems were formulated first and then mixed with the third to form the ternary system as illustrated in Figure 3.11. The sample preparation was conducted at ambient temperature:

· Inorganic salts were formulated from powder forms of substances with

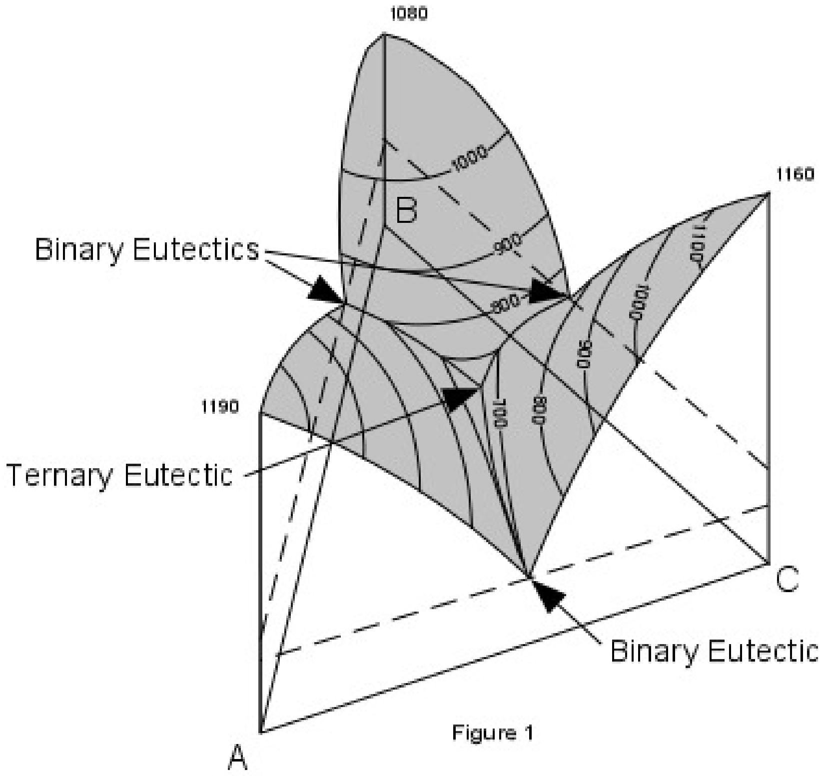

Figure 3.10: A typical 3D ternary phase diagram with isotherms (Nelson, 2011)

different eutectic mass or molar ratios.

- Magnetic stirrer was employed in this step to agitate the mixture until a homogeneous solution is obtained and no segregation particles can be observed.

- The ternary salt-water solutions were prepared according to their mass fraction by mixing the binaries.

- The nucleating agents, thermal conductivity enhancer and the thickening agents were added into the uniform solutions for thermal properties enhancement. The agents were weighted and added into the aqueous solutions.

- In order to ensure the agents are well dispersed, samples were shaken by hand and then left in the ultrasonic bath for∼20 minutes. The turbidity of the solution can be observed.

- The thickening agents should be added at the end.

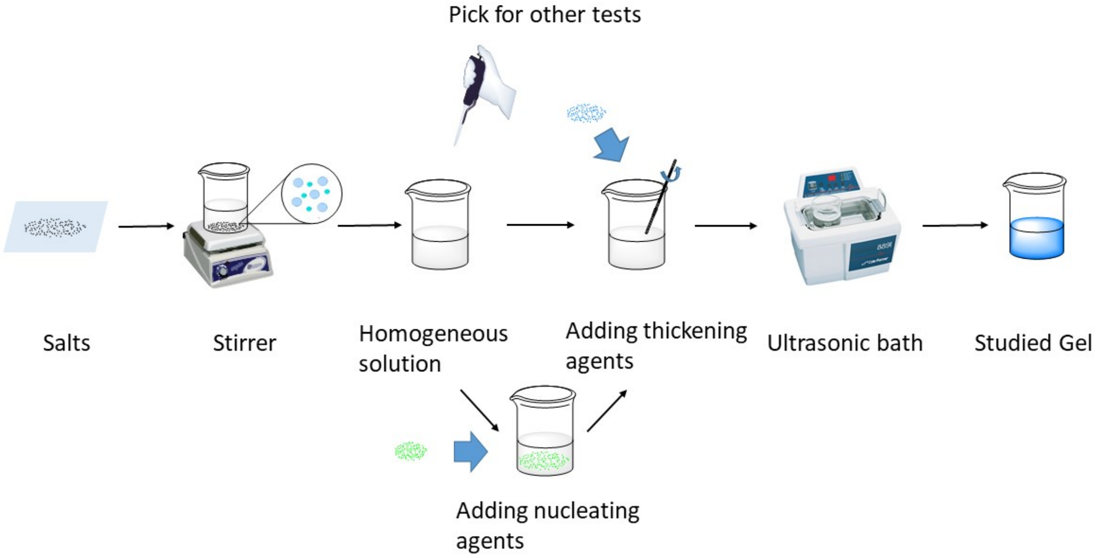

Figure 3.11: The procedure of sample preparation

3.3 Theoretically analysis & modelling

3.3.1 Cooling load calculation

The theoretical base of the cooling load calculation has been illustrated in Section 3.3.1. It consists of five main components: transmission load, infiltration load, product load, miscellaneous load and the safety factors. In this study, the cooling load of a typical commercial vehicle on a 8 h-long trip was calculated according to the specification provided by Hubbardproduct. 100 mm polyurethane board is employed as insulation material for refrigeration space.

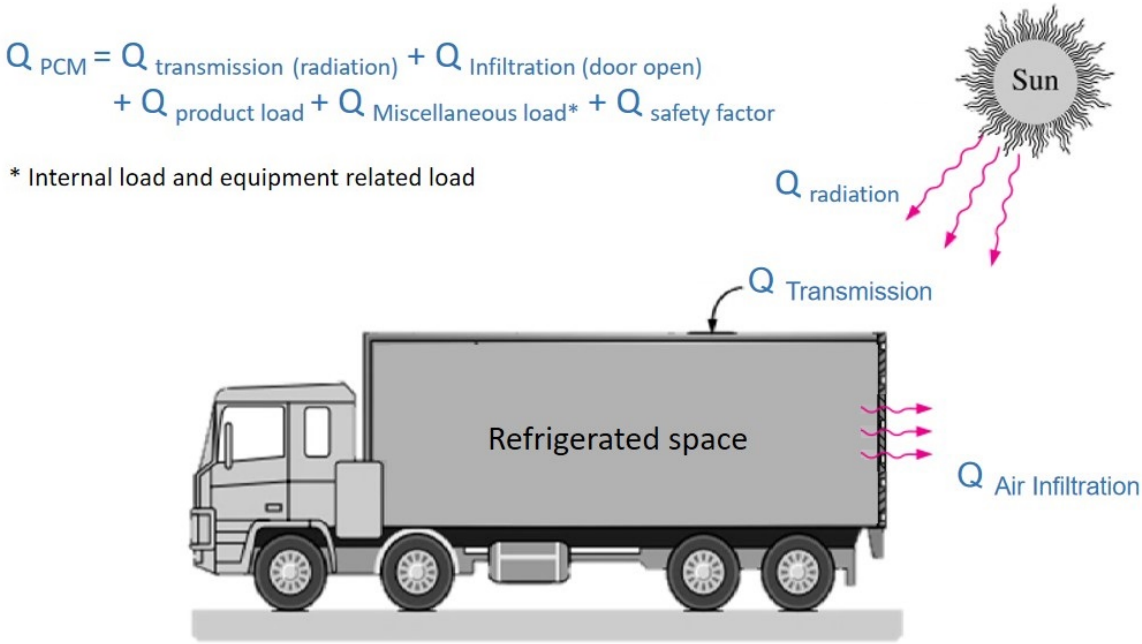

Figure 3.12: The cold load for pre-cooled refrigerated transport

3.3.1.1 Transmission Load

The heat energy lost by conduction through an opaque walls (Q_t) [W] is equal to:

$$Q_t = UA_o\Delta T \tag{3.3}$$

where,

U = overall heat transfer coefficient [W/(m^2 K)];

A_o = outside surface area of the container [m^2];

ΔT = temperature difference between air in refrigerated space and ambient air [K]

The overall heat transfer coefficient U depends on the thermal conductance coefficient of the materials used in the container wall. The coefficient of heat transmission of a multi-layer insulation can be calculated by Equation 3.4.

$$U = \frac{1}{\frac{1}{h_i} + \sum \frac{x}{\lambda} + \frac{1}{h_o}} \tag{3.4}$$

where,

h_i = heat transfer coefficient of inside surface [W/(m^2 K)];

x = thickness of the isolation layer used in the wall [m];

λ = thermal conductivity of the insulation layer [W/(m K)];

h_o = heat transfer coefficient of outside surface [W/(m^2 K)]

For still air, the value of h_i is commonly defined as 1.6 w/(m^2 °C); h_o is associated with air velocity (vehicle speed). When it is the moderate movement condition on which the velocity is 25 km/h, h_o is equal to 6 (ASHRAE, 2014b). To simplify the equation, the thermal resistances of container metal, coefficients h_i and h_o are negligible, as these factors have a relatively small influence on the result.

The temperature difference for the solar radiation effect can be added according to Table 3.3.

Table 3.3: The temperature added for cooling load calculation by radiation effect in different orientations (ASHRAE, 2014b)

Surface type	East wall (K)	South wall (K)	West wall (K)	Roof (K)
Dark-coloured surfaces				
Slate roofing Tar roofing Black paint	5	3	5	11
Medium-coloured surfaces				
Unpainted wood Brick Red tile Dark cement Red, gray or green paint	4	3	4	9
Light-coloured surfaces				
Write stone Light-coloured cement Write paint	3	2	3	5

3.3.1.2 Infiltration Load

The calculation of infiltration load was conducted under different scenarios: In the absence of wind, the infiltration load is calculated by ASHRAE (2014b):

$$Q_i = qD_tD_f(1 - E) \tag{3.5}$$

where, q is the following air exchange assumption promoted by Foster et al.

(2003) listed in Equation 3.6.

$$q = 0.221A(h_i - h_r)\rho_r(1 - \rho_i/\rho_r)^{0.5}(gH)^{0.5}F_m, \qquad \text{(W)} \quad (3.6)$$

where,

A = doorway area, [m^2]

h_i, ρ_i = the enthalpy and density of infiltration air, respectively, [J/kg] [kg/m^3]

h_r, ρ_r = the enthalpy and density of refrigerated air, respectively, [J/kg] [kg/m^3]

g = gravitational acceleration constant, 9.81, [m/s^2]

H = doorway height, [m]

F_m = the density factor, determined by:

$$F_m = \left[\frac{2}{1 + (\rho_r/\rho_i)^{1/3}}\right]^{1.5} \quad (3.7)$$

D_t and D_f are the factors of doorway open-time and flow, respectively. They indicate the influence of constantly or frequently door opening. D_t can be calculated by:

$$D_t = \frac{(\omega\Theta_P + 60\Theta_o)}{3600\Theta_d} \quad (3.8)$$

where,

ω = number of doorway passages

Θ_p = door open/close time, [s]

Θ_o = door opening time, [min]

Θ_d = time period, [h]

The value of D_f is equal to 1 when the actual air exchange is fully established. D_f is recommended to be 0.8 when the temperature differential larger than 11°C. E is the effectiveness of doorway protective device, air curtain for instance. E can be 0.95 or higher with a newly installed doors (Hendrix, Henderson, and Jackson, 1989; Downing and Meffert, 1993). It may drop rapidly to 0.8 on freezer doorways and 0.85 with other doorways according to the traffic and maintenance conditions (ASHRAE, 2014b).

In a negative pressure scenario, air may flow directly through the doorway. This heat gain is stated in *ASHRAE Handbook-Refrigeration* (ASHRAE, 2014b). Instead of using Equation 3.5, It can be determined by:

$$Q_i = \dot{V} A (h_i - h_r) \rho_r D_t \tag{3.9}$$

A is the small leakage area of the loading doors. It varies from 0.03 m^2 to over 0.1 m^2 per door depending on the door maintenance. The time length that the doors are partially or fully opened needs to be considered for a high merchandise movement (ASHRAE, 2014b).

The average air velocity $\dot{V}$ is generally determined by a known pressure difference between the inside and outside of the walls or external force across the doorway. $\dot{V}$ has a typical value of 0.3 to 1.5 m/s.

The method of estimating the pressure difference has a significant uncertainty, so a more practical way is to estimate the air changes per hour (ACH) (Çengel and Ghajar, 2011), which is equal to:

$$ACH = 3600\frac{\dot{V}}{V} \tag{3.10}$$

where $\dot{v}$ is the volume flow rate of the infiltrating air [m^3/s], V is the volume of the refrigerated space [m^3].

With air change method, the infiltration load is calculated from sensible and latent components of changing air. Çengel and Ghajar (2011) and Kharagpur (2016) provide different calculation method as illustrated in Equation 3.11 and Equation 3.12:

$$\begin{aligned} Q_i &= \dot{V}\rho_i((h_i - h_r) + h_w\Delta w) \\ &= \frac{ACH}{3600}V\rho_i((h_i - h_r) + h_w\Delta w) \end{aligned} \tag{3.11}$$

$$Q_i = \dot{V}\rho_i(C_p\Delta T + h_w\Delta w) \tag{3.12}$$

where,

C_p = specific heat of the infiltrating air, [J/kg K];

h = water vaporisation heat, [J/kg];

Δw = air humidity ratio difference between ambient and refrigerator, [kg/kg dry air] The value of Δw is determined from the psychometric chart.

Given the refrigerating condition, the metabolic influence of the product can be ignored. In conclusion, the total heat energy required for a refrigerated vehicle is the sum of those aforementioned variables plus a safety factor. A 10% safety factor was added in the calculation for the extreme operating conditions. The calculation was done by Matlab to analysis the cooling load of the refrigerated vehicle.

3.3.2 Modelling

3.3.2.1 Theoretical basis

A 2D transient model was employed to study the performance of the air curtain on the cooling dissipation reduction. The study is based on three fundamental governing equations: conservation of Mass, conservation of momentum and the energy equation. The air circulation in the refrigerated space is calculated as natural convection and the circulating air is considered as the incompressible ideal gas. The calculating details are explained as follows.

Conservation of Mass (Continuity)

The overall mass balance is represented by continuity equation, in which the accumulation of the mass within a control volume (CV) per unit time is equal to the mass convection in and out. It is expressed as Equation 3.13.

$$\frac{\partial \rho}{\partial t} + \nabla \cdot (\rho \boldsymbol{u}) = S_m \tag{3.13}$$

Where ρ is the density [kg/m^3], ∇ is the spatial derivative operator that presents the different dimensions, $\boldsymbol{u}$ is the flow velocity vector. S_m is the additional source term that generated by liquid vaporisation etc.

For the steady state, the equation can be simplified into

$$\nabla \cdot (\rho \boldsymbol{u}) = 0 \tag{3.14}$$

Conservation of Momentum (Navier-Stokes)

The conservation of momentum follows Newton's 2_{nd} Law.

It is discribed by

$$\frac{\partial (\rho \boldsymbol{u})}{\partial t} + \nabla \cdot (\rho \boldsymbol{u}\boldsymbol{u}) = -\nabla P + \nabla \cdot \bar{\bar{\boldsymbol{\tau}}} + \rho \boldsymbol{g} + \boldsymbol{F} \tag{3.15}$$

where, P is the static pressure, $\bar{\bar{\boldsymbol{\tau}}}$ is the stress tensor, the source term $\rho \boldsymbol{g}$

is the gravitational body force, $\boldsymbol{F}$ includes the external body forces or other model-dependent source terms.

The stress tensor $\bar{\bar{\boldsymbol{\tau}}}$ is given by:

$$\bar{\bar{\boldsymbol{\tau}}} = \mu[(\nabla \boldsymbol{u} + \nabla \boldsymbol{u}^T - \frac{2}{3}\nabla \cdot \boldsymbol{u} I)] \tag{3.16}$$

where μ is the molecular viscosity, I is the unit tensor.

Energy Equation

The energy transport for solidification/melting problems is calculated by

$$\frac{\partial(\rho H)}{\partial t} + \nabla \cdot (\boldsymbol{u}\rho H) = \nabla \cdot (\lambda \nabla T) + S_h \tag{3.17}$$

where, T is the temperature [K] and S_h is the volumetric heat source. Specifically, the second term is carried out by convective energy transfer such as rotation and translational motion. The enthalpy H stands for the thermal storage density which consists of sensible heat h and latent heat ΔH. They can be calculated respectively as follows:

$$h = h_{ref} + \int_{T_{ref}}^{T} C_p \, dT \tag{3.18}$$

where h_{ref} is the sensible heat of the reference, T_{ref} is the reference temperature, C_p is the specific heat of the PCM under a constant pressure.

$$\Delta H = \gamma L \tag{3.19}$$

where L is the whole latent heat of the PCM and γ is the liquid fraction varies from 0 to 1. By which means

$$\gamma = \begin{cases} 0, if\ T < T_{solidus}, \\ 1, if\ T > T_{solidus}, \\ \frac{T - T_{solidus}}{T_{liquidus} - T_{solidus}}, if\ T_{solidus} < T < T_{liquidus} \end{cases} \tag{3.20}$$

Natural convection

The air circulation in the refrigerated space is essential in the study on the performance of the PCMs. Hence the modelling of natural convection is included in this study. The circulating air is considered as the incompressible ideal gas as the pressure change is negligible compared with the operating pressure p_o, which indicated that the density of air is operating pressure dependent only.

$$\rho = \frac{p_o}{\frac{R}{M_w} T} \tag{3.21}$$

where,

M_w is the molecular weight of the gas. R is the universal gas constant =

8.314 J/(mol K).

In this case, buoyancy and gravitational forces are the major driving forces of the density gradients within fluid in this circumstance. The operating density ρ_o is introduced into the momentum equation to stabilise the system, where the body-force term S_M is equal to Equation 3.22. The operating density is selected to be close to the average fluid density.

$$S_M = \underbrace{(\rho - \rho_o)\boldsymbol{g}}_{\text{Buoyancy}} \tag{3.22}$$

$\boldsymbol{g}$ is the gravitational acceleration [N/kg].

The strength of the buoyancy force is determined by the Rayleigh number. It indicates the transition of laminar flow to turbulence flow.

$$R_a = \frac{g\beta\Delta T L^3 \rho}{\mu\alpha} \tag{3.23}$$

where,

β = the thermal expansion coefficient, [K^{-1}];

L = the characteristic length of the object, [m];

μ = the kinematic viscosity of the material, [m^2/s];

α = the thermal diffusivity of the material, [m^2/s];

$$if\ R_a \begin{cases} < 10^8,\ laminar flow, \\ \approx 10^9,\ transition, \\ > 10^{10},\ turbulent flow \end{cases} \tag{3.24}$$

The mathematical model uses the finite volume method that evaluates over small control volumes. The procedure of the pressure based solution methods is shown in Figure 3.13. The accuracy of simulation results is related to the boundary conditions, cell zone conditions and material properties.

3.3.2.2 Model setup (Cong et al., 2019)

The schematic diagram of a commercial refrigerated vehicle container is illustrated in Figure 3.14. The research object is a typical refrigerated container with an 0.1 m insulation wall layer. It is assumed that the perishable products and container are pre-cooled to the desired temperature (5 °C). Goods were placed in the left domain inside the refrigerated container while the right domain was occupied with the stationary air of 5 °C when the door is closed. The ambient temperature outside the container was set to 35 °C. The thermophysical properties of air and pre-cooled goods are listed in Table 3.4.

The dashed lines in the sectional view in Figure 3.14 show the location of the rear door. Grilles are installed at both the top and bottom of the doorway. When the door opens, the cold air (set as 5 °C) is ejected from the

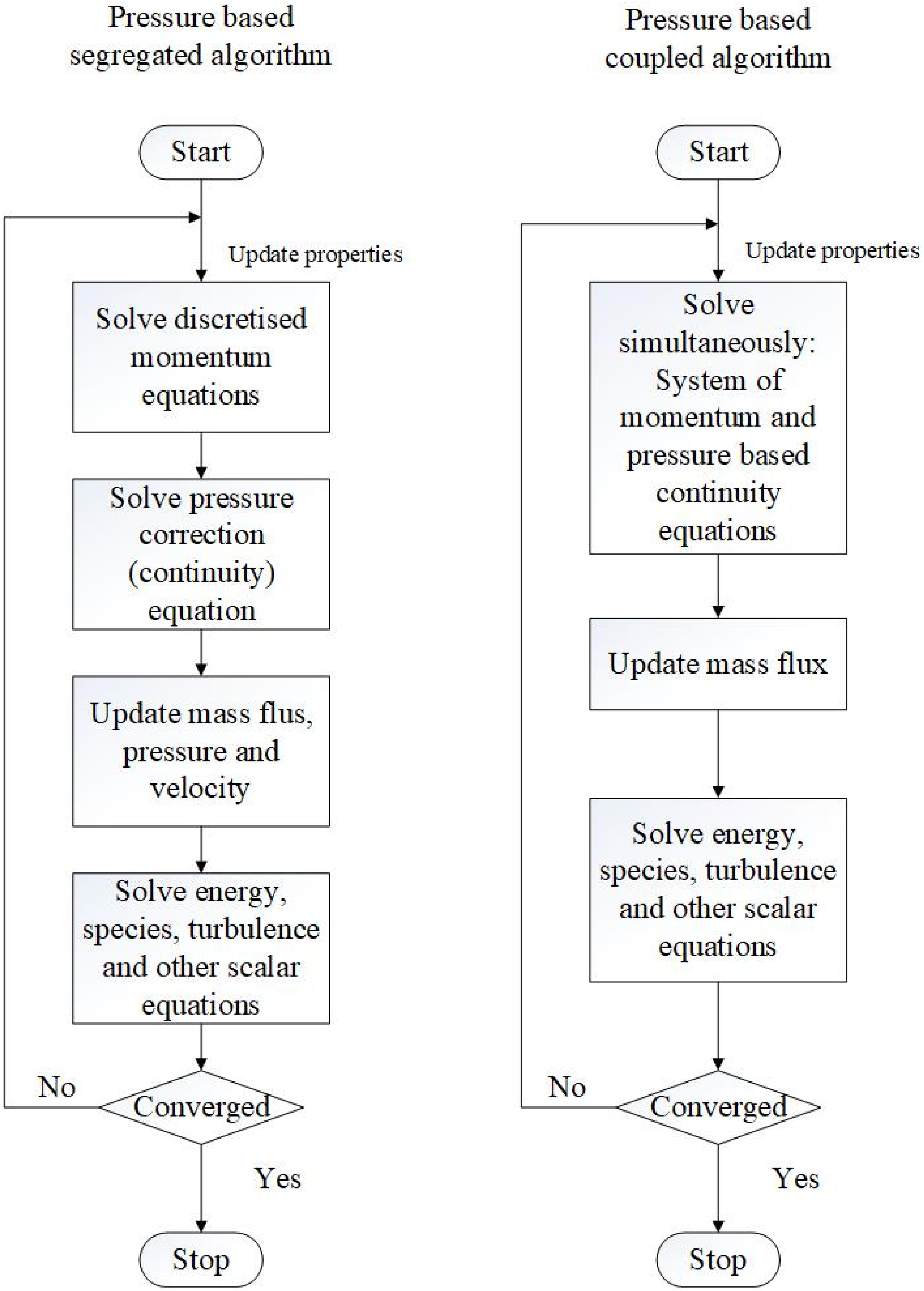

Figure 3.13: The procedure of the pressure-based solutions

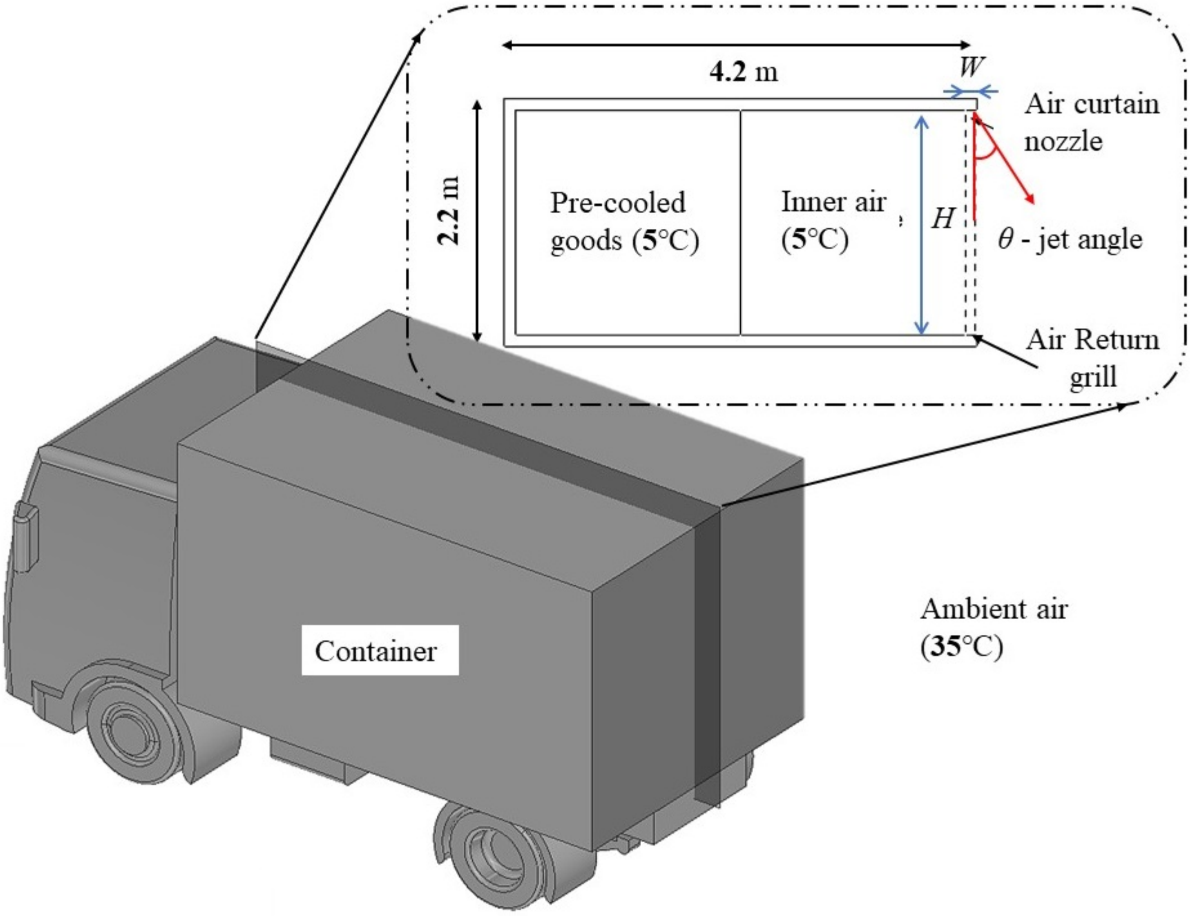

Figure 3.14: The three-view drawing of one PCM beam group

top grille (i.e., nozzles) and returns through the bottom grille. A jet-type air curtain is therefore formed at the open doorway. The cold air can be supplied by a refrigerated system or a high-pressure air storage tank with a throttling device. The latter can respond to the door opening more rapidly and efficiently. The cold air can also be a reused by-product from the cryogenic applications, such as liquid air energy storage or cold energy recovery during regasification of liquefied natural gas. The moment when the door is opened is regarded as the initial time in the simulations, also known as t = 0 s. The

Table 3.4: Thermoproperties of air and pre-cooled products

	Air	pre-cooled goods
Density (kg/m^3)	Incompressible-ideal gas	540
Specific heat (J/kg K)	1006.43	2193
Thermal conductivity (W/m K)	0.0242	0.14
Viscosity (kg/m s)	1.7894 x 10^{-5}	

air at atmospheric pressure is assumed to be incompressible ideal gas and Newtonian fluid. The temperature difference between the air outside and inside the container leads to a horizontal gradient of air density. The density gradient combined with the action of gravity induces natural convection of air and is accompanied by a heat transfer when the door is opened. Gravity was considered in this simulation along the opposite direction of the Y-axis. The addition of the air curtain introduces forced convection of air. The transient mixed convection of air is governed by the three conservation equations (as illustrated in Section 3.3.2.1).

The computational domain is extended from the container toward outside. The ground is treated as the bottom boundary of the extended domain, while the boundaries in other directions are extended far enough until their positions have little or no influence on the air motion or temperature distribution inside the cavity. The temperature is kept at 35 °C and the air velocity is zero on the ground, while the temperature is also kept at 35 °C. The shear stress is zero at the other extended hypothetical boundaries. Adiabatic and nonslip boundary conditions are assumed at both the internal and external surfaces of the insulation wall layer. Temperature continuity and heat flux conservation are applied at the interface of the pre-cooled products/air in the numerical simulations. The velocity boundary is given at the air curtain grille/nozzles, where the inlet air velocity (v) varies from 0 m/s to 4 m/s. The pressure boundary is given at the air return grille. Our preliminary simulations indicate that the pressure value has a little effect on the air curtain. To avoid consuming excessive power to maintain the pressure at the air return grille, the pressure is set as 0.9 bar which is close to the atmospheric pressure. The inner height of the container, the nozzle width, and the jet angle are denoted by H, W, and θ, respectively. The definition of the jet angle is the angle between the air velocity direction at the nozzle and the opposite direction of the Y-axis. The angle is negative when the air velocity tilts inwards. In addition, the nondimensional parameters such as Reynolds number and relative nozzle width (W/H) are introduced in the paper to extend the applicability of the study.

Since every cross section of the container parallel with the cross section as shown in Figure 3.14 has the same boundary conditions except for the cross section close to the side wall of the container. Their flow patterns and temperature distributions should be nearly the same. In order to save computational resources, a two-dimensional (2D) model based on the cross section as shown in Figure 3.14 is adopted for the simulations in this study. The simulations were carried out through the commercial CFD software FLUENT 18.2, which is based on the finite volume method. The Semi-Implicit Method for Pressure Linked Equations (SIMPLE) scheme was selected as the solving method. The standard k–ϵ model was employed to account for turbulent behaviour of air convection. The second-order upwind type was used to discretise momentum and energy equations. The convergence criteria were that the residuals of continuity, momentum, and energy equations at each time step achieved 10^{-3}, 10^{-3}, and 10^{-6}, respectively. Once the convergence criteria were met at each time step, the transient solutions were obtained. The time step was set as 0.2 s. The velocity and temperature of air were calculated within 1 min after the door was opened.

Grid independence

The extended computational domain with structural grids is shown in Figure 3.15. The structural grids are generated by the meshing software ICEM with refinement in the regions near the doorway and the solid/fluid interfaces, because the heat and mass transfer phenomenon is more complicated than in other regions.

First, the independent test of the extended computational domain was

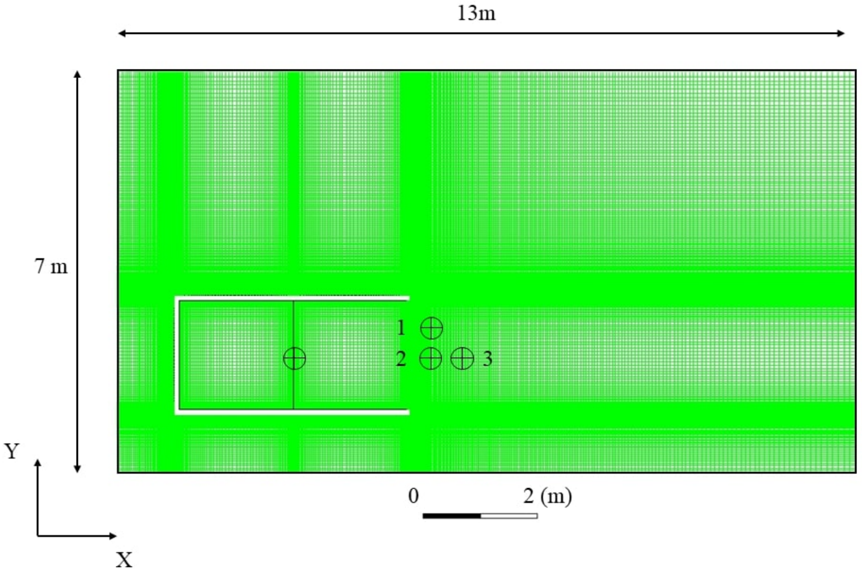

Figure 3.15: the computational domain, grids, and the position of the monitored points marked by ⊕

conducted based on four different computational domains with the sizes of 10 m × 5 m, 13 m × 5 m, 13 m × 7 m, and 16 m × 9 m in length × height. The similar grid resolution was employed for the four computational domains. The predicted average air temperatures inside the container under the four extended computational domains are summarised in Table 3.5 (a). It can be found that the average air temperature difference inside the container between the third and fourth computational domains is less than 0.3 °C. Therefore, further simulations in this study were accomplished under the third computational domain (i.e., 13 m × 7 m).

Second, the independence of the grid was examined on the basis of four different grid sets with about 63,000, 75,000, 86,000, and 98,000 cells. The

Table 3.5: Results of the independent test of the computational domain (a) and grids (b) for the average air temperature ($\bar{T}$) inside the container at t = 30 s

(a)

Domain size (m)	$\overline{T}$ (°C)	Difference (°C)
10 x 5	6.50	-
13 x 5	7.32	0.82
13 x 7	7.86	0.54
16 x 9	8.08	0.22

(b)

Grid number	$\overline{T}$ (°C)	Difference (°C)
63,000	6.98	-
75,000	7.51	0.53
86,000	7.86	0.35
98,000	7.97	0.11

predicted average air temperatures inside the container under the four grid sets are summarised in Table 3.5 (b). It can be seen in this table that the difference of the average air temperature inside the container is less than 0.2 °C between the third and fourth grid sets. Thus, the following simulations in this study were accomplished under the third grid set (i.e.,86,000 cells). The independent tests of the computational domain and grids provide a good trade-off between computation accuracy and time. The monitoring points of temperatures are also displayed in Figure 3.15. One is located at the air–goods interface and three points labelled by 1, 2, and 3 are located outside the container. Point 2 is located at the middle position of the doorway along the Y-axis and at 0.5 m away from the doorway along the X-axis. Point 1 and Point 3 are located at 0.5 m above Point 2 and at 0.5 m on the right of Point 2, respectively. Besides, the average air temperature inside the container was also monitored.

CHAPTER 4

RESULTS AND DISCUSSION: PCM SCREENING

This chapter presents the screening procedure of salt-water PCMs at −25 °C and −33 °C, respectively. In Section 4.1 PCMs with different compositions are compared and screened. Section 4.2 discusses the process of achieving eutectic point of two PCM systems.

Conforming to the Theory of Freezing Point Depression, the PCM with a lower phase change temperature can be formulated by mixing multicomponent together. Hence PCMs with a slightly higher phase change temperature than the favourable temperate and large energy storage density are considered. As it is discussed in Section 2.2.3, $-25\,^{\circ}\mathrm{C}$ and $-33\,^{\circ}\mathrm{C}$ is the favourable PCM phase change temperature for refrigerated application. Potential PCM candidates are selected within this temperature range from Table 2.4.

Following the selection criteria reported in Section 2.2, eutectic $MgCl_2$ salt-water solution is suitable for $-33\,^{\circ}\mathrm{C}$ refrigeration because of the applicable phase change temperature and larger energy storage density compared to other organics and nitrate salt solutions. However, the eutectic ratio of the $MgCl_2$ salt-water solution were claimed differently in literature. This will be discussed with more details in Section 4.1.2.

Although the organic material - undecane has a more favourable phase change temperature near$-25\,^{\circ}\mathrm{C}$ than others, its latent heat and density are much lower than salt-water solutions. Li_2SO_4, KF and NaCl eutectic solutions are high latent heat eutectic PCMs. Among them, Li_2SO_4 solution is expensive and highly hygroscopic whilst KF solution is poisonous and highly corrosive. Hence, NaCl aqueous solution is chosen to be the base material among these candidates.

Both $MgCl_2$ and NaCl salt-water solutions have a relatively high fusion heat, non-toxic, safe for food delivery, available and inexpensive, suitable for commercial use. The thermophysical properties of selected binary eutectic PCMs are studied. In addition, since the phase change temperate of $MgCl_2$ salt-water solution is favourable, in further studies, it can be mixed with thermal property enhancement agents directly to optimise the performance. For NaCl salt-water solution, further steps are needed to decrease the phase change temperature to be applicable to the application.

Section 2.3.1 illustrated the screening process of the ternary salt-water solutions that formed of two binaries. It was started with eutectic NaCl solution as the first component in the formulations. Then the second component was determined by applying the selecting criteria listed in Section 2.3. And the experimental solubility data of each selected solvents was researched and presented in Figure 4.1. Extension lines derived in Figure 4.1 demonstrated their solubility of each compound at $-25\,°C$.

The solubility curves of most salts appear linear responding to the temperature changes. For sodium sulphate and sodium carbonate, the slope of solubility curve changes noticeably through the the solving process because the phase transitions occur (Beckmann, 2013).

In this case, $NaNO_3$, NH_4Cl and KCl eutectic solutions are selected as

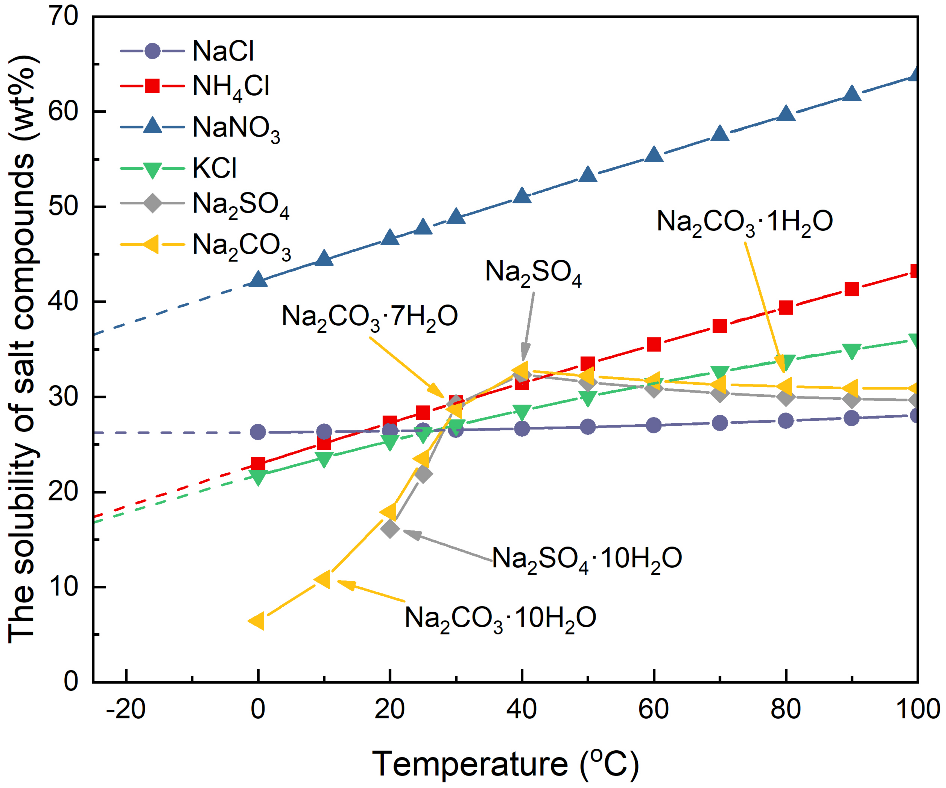

Figure 4.1: The solubility of the selected inorganic compounds in water (Lide, 2010)

the potential second component. Na_2SO_4 eutectic solution is also tested as reference. Their thermophysical properties are examined using DSC and compared with the value in literature. The deviation of DSC result indicates that the binary PCM candidates delivered acceptable thermophysical properties.

Table 4.1: The thermophysical properties comparison of PCMs from literature and experiment

PCM	Eutectic composition (wt%)	Phase change temperature (°C)		Latent heat (kJ/kg)	
		Lit	Exp	Lit	Exp
$MgCl_2/H_2O$	17.1	-33.6	-33.0	211.18	197.4
	22	-33.5	-33.1	-	179.4
$NaCl/H_2O$	22.4	-21.2	-21.56	222	211.46
$NaNO_3/H_2O$	36.9	-17.7	-17.65	188	187.8
NH_4Cl/H_2O	19.5	-16	-15.24	248.44	248.06
KCl/H_2O	19.5	-10.7	-10.9	283	260.38
Na_2SO_4/H_2O	12.7	-3.6	-3.32	284.95	273.13

4.1 PCM composition

4.1.1 Ternary eutectic solution for −25 °C

For −25 °C application, the properties of four PCM additives for NaCl solution are as follows: $NaNO_3$ solution has a lower latent heat than the base material; KCl and Na_2SO_4 solutions have a favourable latent heat while the latter is less soluble at sub-zero temperatures.

Firstly, a proper ternary salt-water system with desired phase change temperature was investigated. The second, components are formulated with specific eutectic mass or molar ratios and mixed with eutectic NaCl solution in a series of different ratios: 3:1, 2:1, 1:1, 1:2, 1:3. Mixing the compatible binary solutions yields ternary salts-water solutions. The thermophysical properties of ternary salts-water solutions are characterised by DSC.

Figure 4.2 shows the phase change temperature and latent heat of four different ternary salt-water systems. The control group NaCl solution is marked black.

It can be seen in Figure 4.2(a) that the phase change temperature of the eutectic NaCl solution decreases with the addition of the second component and the extent of the decrease depends on the mass ratio. The ternary salt-water solutions have a phase change temperature range of $-21\,^{\circ}\mathrm{C}$ to $-27\,^{\circ}\mathrm{C}$. The phase change temperatures of these different combinations have the following sequence: NaCl-Na_2SO_4 solution > NaCl-KCl solution > NaCl-NH_4Cl solution > NaCl-$NaNO_3$ solution. The results also indicate that as long as the same components are presented in the ternary system, the PCMs tend to have a invariant onset temperature of the phase transition (at certain pressure) (Perry and Chilton, 1973), with which the eutectic phase change temperature can be predicted. Moreover, NaCl-Na_2SO_4 solution has the highest phase change temperature of $-21\,^{\circ}\mathrm{C}$ and NaCl-$NaNO_3$ solution has the lowest which is around $-27\,^{\circ}\mathrm{C}$. A conclusion can be drawn that a larger temperature difference of two components leads to smaller change of phase change temperatures. If two components have a large temperature difference, the one with a higher temperature is likely to suffer from insoluble

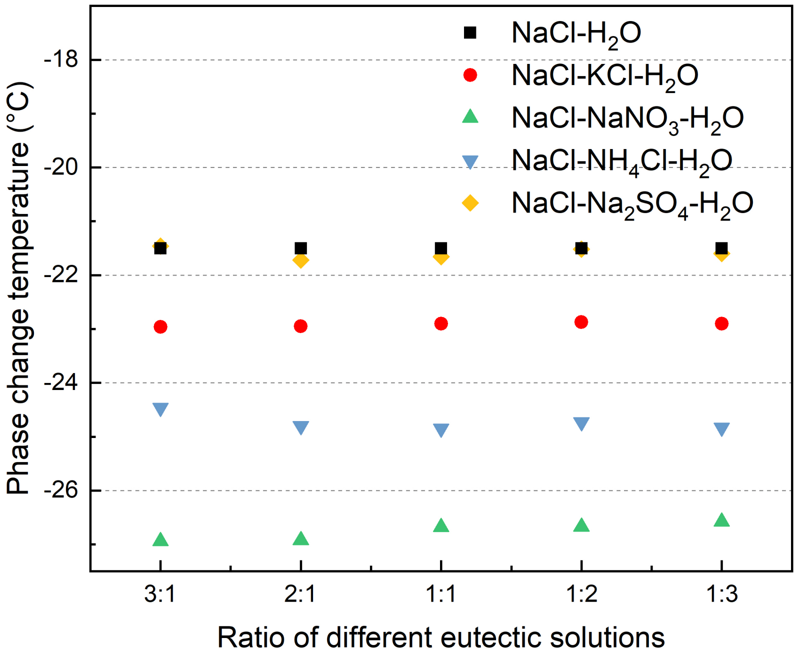

(a)

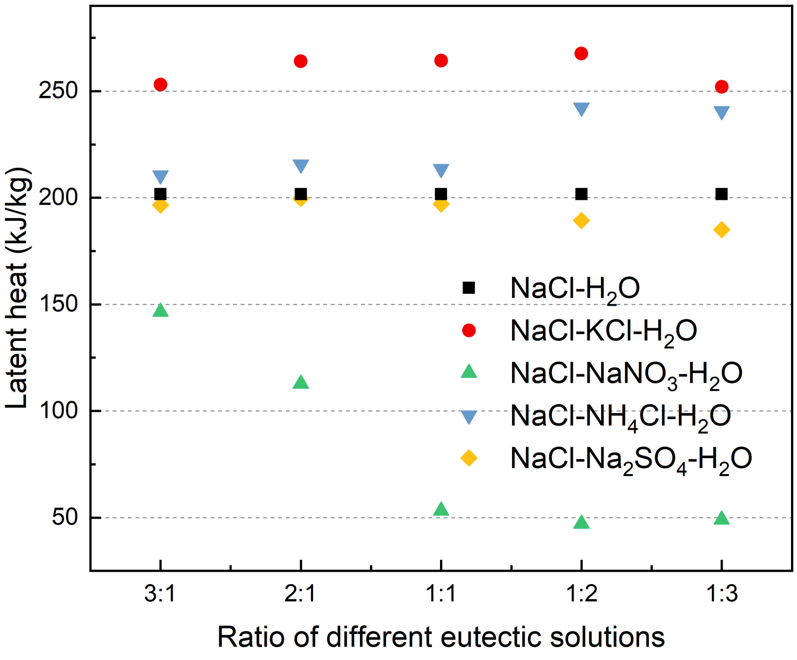

(b)

Figure 4.2: The DSC results of (a) the lowest melting temperature and (b) latent heat of different ternary aqueous solutions

issues after mix.

Figure 4.2(b) shows the latent heat of four ternary systems. The NaCl-KCl solution has the highest heat of fusion among the four PCMs with the phase change temperature of −23 °C. Compared with the NaCl solution, an increase of heat of fusion is observed in the NaCl-NH_4Cl solution, that of the NaCl-Na_2SO_4 solution has no obvious difference, whereas that of the NaCl-$NaNO_3$ solution decreases. DSC peaks show asynchronous phase change in some of the formulations, which leads to phase separation after long-term use, for example, the ratio of NaCl aqueous solution and $NaNO_3$ aqueous solution at 3:1. Additionally, there is minor difference between the NaCl-Na_2SO_4-H_2O solutions and the base solution in both figures because of the solubility issue of Na_2SO_4 at low temperature demonstrated in Figure 4.1.

In sum, it is evident that both NaCl-KCl and NaCl-NH_4Cl solutions show a larger latent heat than the NaCl solution. The latter has a more favourable phase change temperature close to −25 °C. As a result, NaCl-NH_4Cl solution was chosen to be the studied ternary system. Some researches have studied the eutectic composition of the same ternary system at different temperatures (Cui, 2009). But no experimental date can be found at this temperature so far.

In order to obtain the eutectic composition, a series of experiments were done with different salt ratios at a heating rate of 5 °C/min. Their DSC heating curves were shown in Figure 4.3. It is suggested that with the same components, the ternary systems tend to begin phase change at around −25 °C. Both eutectic NaCl solution and NH_4Cl solution present single symmetric peaks. With the introducing of the second component, asynchronous peaks appear because of the incongruent melting behaviour. Peaks are moving closer and overlapping with each other when the ternary system approaching the eutectic composition. In the end, the eutectic ternary composition gains an unique melting point and yields the lowest melting temperature. This property is also used as the theory to analyse the eutectic point by DSC.

However, identifying the overlapped peaks for the adjacent compositions of the eutectic points with DSC is challenging. In the case of Figure 4.3, the DSC curves of the solutions that has 60% to 80% of NaCl solution look similar as they have only one peak each. This brings uncertainty to the eutectic formulation. Therefore, further work needs to be done to obtain more precise eutectic formulation of the NaCl-NH_4Cl system.

A slow heating rate in DSC helps us have a better understanding of the phase change phenomenon, so the program is set to 1 °C/min. At the same time, the ratio interval of the NaCl solution was shortened to 5%, that are 55%, 60%, 65%, 70%, 75%, 80% and 85% compositions. Results are shown

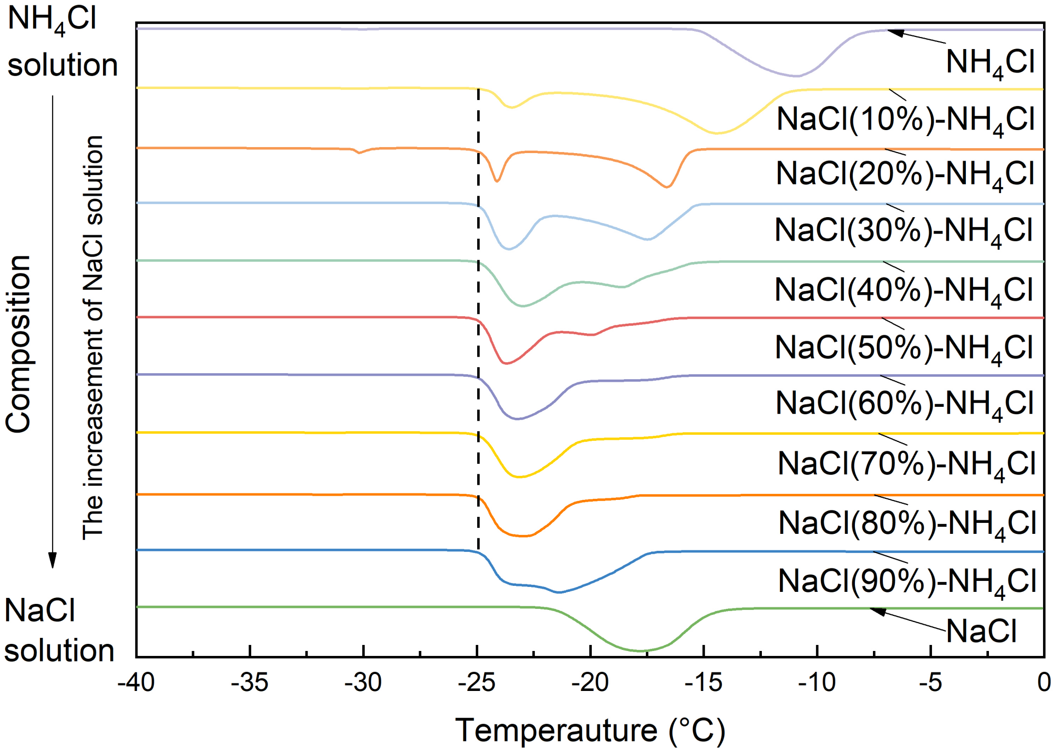

Figure 4.3: The DSC heating curve of NaCl-NH_4Cl solution with various salt component ratios

in Figure 4.4(a). The 55%, 80% and 85% compositions present overlapped peaks during melting process. But still no obvious differences appear in other groups.

On top of that, further experiments were done with 60% - 75% compositions at a lower heating rate of 0.1 °C/min as shown in Figure 4.4(b). All four compositions exhibit single transition peaks at similar phase change temperature. Among them, 70% NaCl solution presents a relatively symmetric peak whereas others to some extent have shoulders because of the peak overlapping. 70% of NaCl solution has shown the best performance.

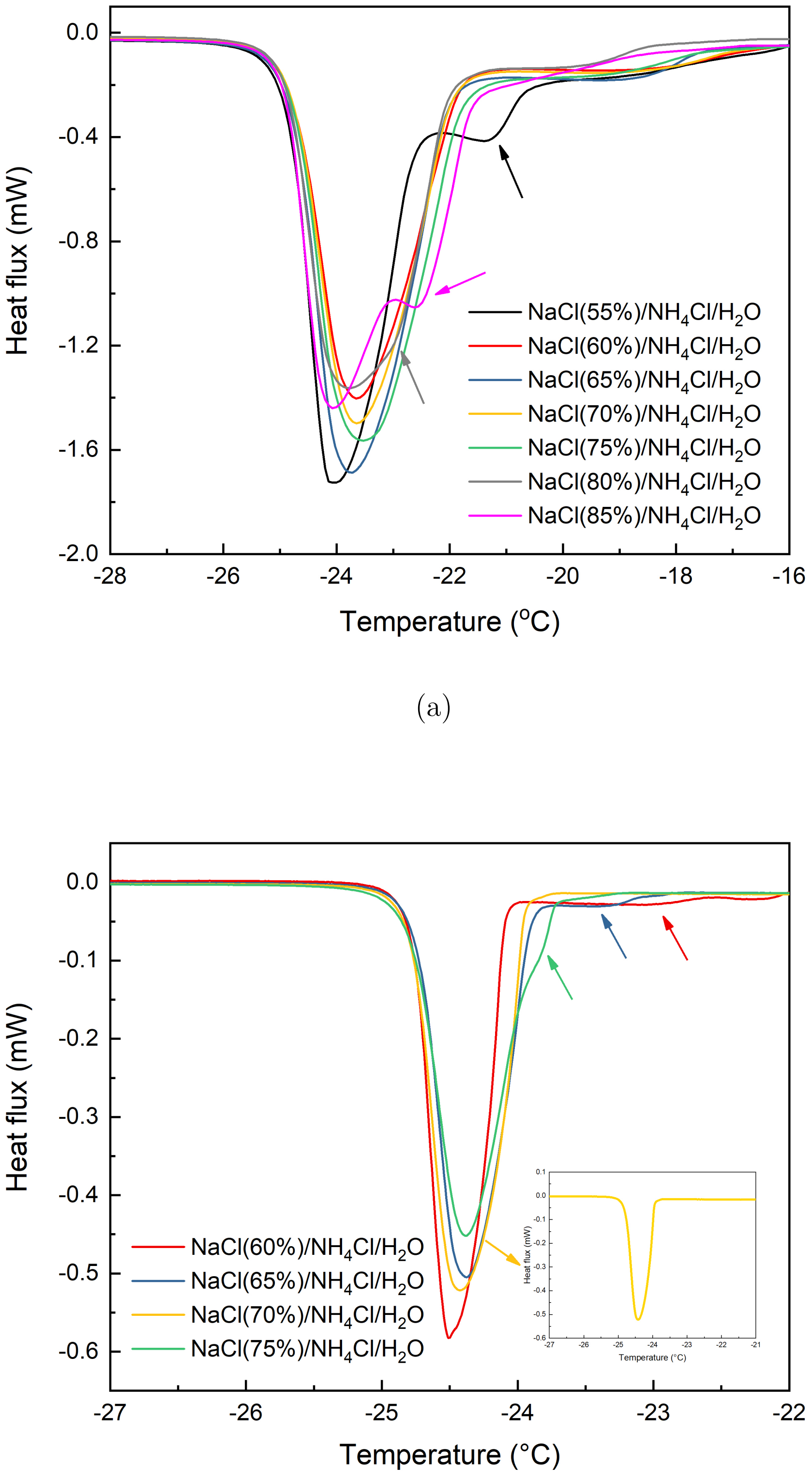

(a)

(b)

Figure 4.4: The DSC heating curve of NaCl-NH_4Cl solutions at a heating rate of (a) 1 °C/min (b) 0.1 °C/min

The binary solutions used as initial components are saturated solutions at their eutectic temperature. There is no evidence shown that the ternary solution remains saturated after mixing and cooling. As a result, the solubility of the salt solvent in water is investigated.

In the literature, the solubility data of the NaCl-NH_4Cl solution at different temperatures was collected and illustrated in Figure 4.7. The temperature range is from $-10\,°C$ to $100\,°C$. The x, y coordinates are the mass ratio of two different salt solvents in 100 kg water, respectively. Zeng and Li (2015) applied mixed-solvent electrolyte (MSE) thermodynamic model to calculate the solid-liquid equilibrium of NaCl-NH_4Cl-H_2O system at $0\,°C$, $50\,°C$ and $100\,°C$. The predicted fitting curve is in good agreement with the turning points of the experimental data. There is an exception that when the temperature is $-10\,°C$, the turning point does not follow the trend. It indicates that at sub-zero temperatures, the solving behaviour is different than at other temperature ranges.

As a result, to study the experimental data, the data of salt components in NaCl-NH_4Cl-H_2O solution was analysed in Figure 4.6. It is depicted that the total salts content is reduced evenly with the temperature decreasing. The two salt components have opposite tendency with the temperature change. While the solubility of NaCl in NaCl-NH_4Cl-H_2O ternary system increases

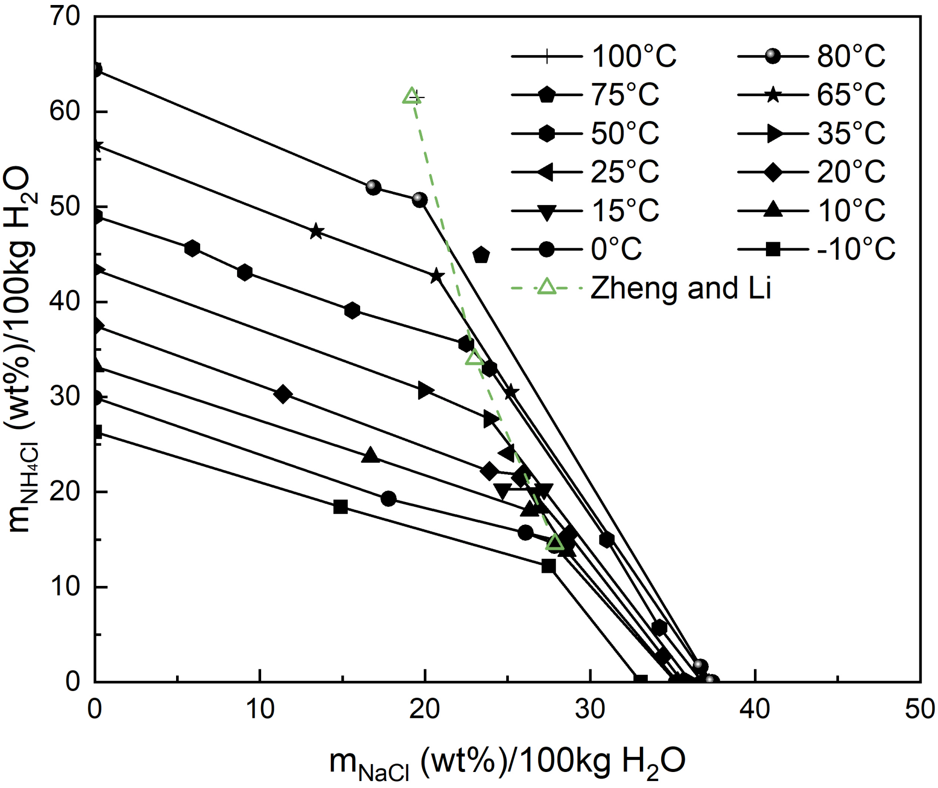

Figure 4.5: The solubility of NH_4Cl and NaCl in water at various temperatures (Seidell, 1919)

with the reduce of the temperature, that of NH_4Cl decreases. Besides, the components content in the ternary system were nearly linear against the temperature. Except when the temperature is −10 °C, the addition of NH_4Cl lowers the solubility of NaCl in the system.

Three extended fitting lines were drawn according to the existing data and their equations are shown in Table 4.2. In case of 4th order polynomial fitting, the R factor of both NaCl and NH_4Cl curves are greater than 0.99. Then when the temperature is −24.8 °C, three intercept points can be obtained

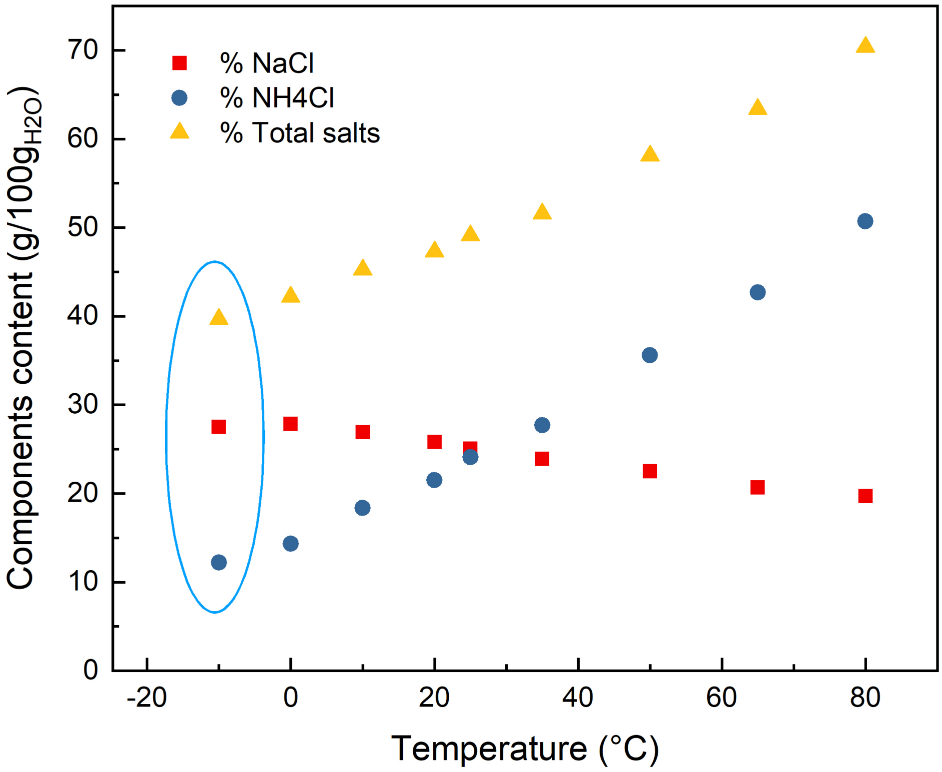

Figure 4.6: The fitting curve of the salts content in NaCl-NH_4Cl-H_2O ternary system at different temperatures

according to the fitting curves in Table 4.2.

Table 4.2: The equations of three component content fitting curves

Components	NaCl	NH_4Cl
linear	= -0.0977 x T + 27.417 (R^2 = 0.9787)	= 0.4354 x T + 14.159 (R^2 = 0.9894)
2^{nd} Polynomial	= -2e-4 x T^2 - 0.083 x T + 27.331 (R^2 = 0.9819)	= 0.0016 x T^2 + 0.3215 x T + 14.824 (R^2 = 0.9991)
4^{th} polynomial	= -4e-7 x T^4 + 7e-5 x T^3 - 0.0039 x T^2 = - 0.0381 x T + 27.665 (R^2 = 0.9972)	= 8e-8 x T^4 - 2e-5 x T^3 + 0.0034 x T^2 = + 0.2936 x T + 14.679 (R^2 = 0.9994)

* T is the temperature [°C]

Afterwards, based on Figure 4.7, the three fitting dots at $-24.8\,°C$ were drawn in the same coordinate system in Figure 4.7. Also, the sample with different salt component ratios in the NaCl-NH_4Cl solution system was marked in the figure.

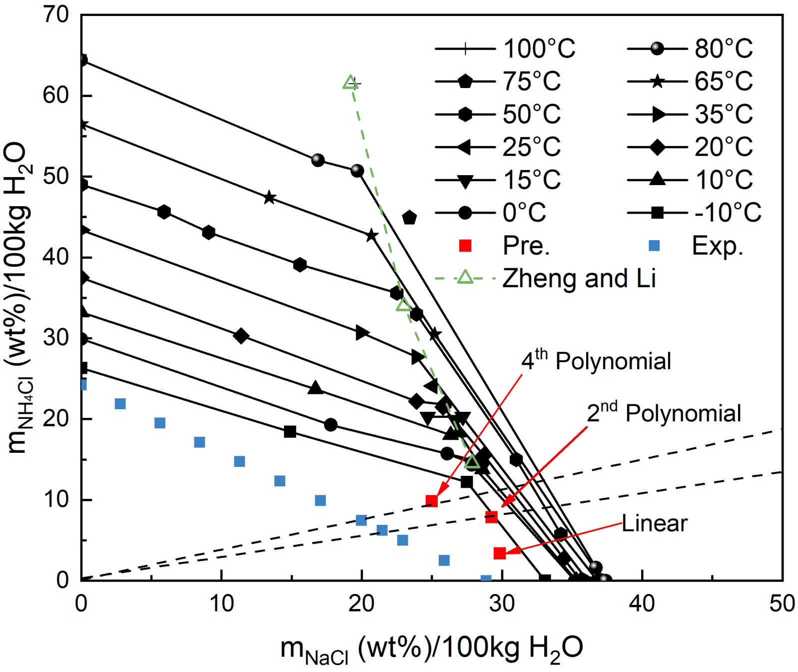

Figure 4.7: The solubility of NH_4Cl and NaCl in water at various temperatures with fitting points

Especially, the 2nd and 4th order polynomial fittings were found on the extended dash lines containing 75% and 70% NaCl, respectively. In each dash line, the salt composition is constant. The 4th order polynomial fitting is in good agreement with the behaviour of saturated composition that has the same salt component ratios system (70% NaCl) at its eutectic composition. Therefore, the turning point of the trend line is found at the sub-zero temperatures.

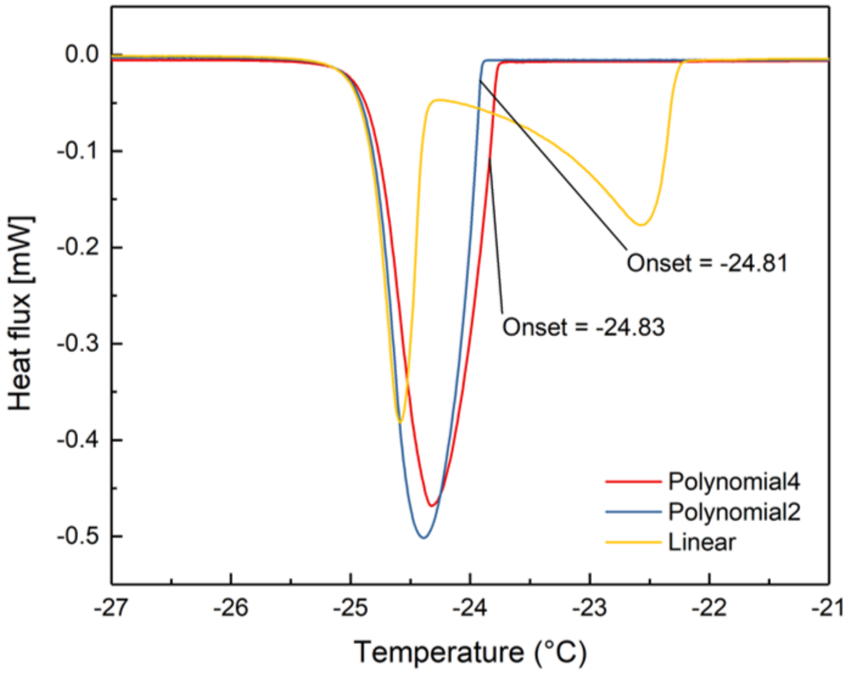

Figure 4.8: The DSC heating curve of the three prediction points

Based on the prediction above, DSC is applied to demonstrate the different thermal behaviours of three predicted compositions with 0.1 °C/min. As is illustrated by Figure 4.8, the linear prediction shows multi-peaks whereas others have the single symmetric peak. No obvious differences were found between 2^{nd} and 4^{th} order polynomial groups. Their onset temperature is $\sim -24.8\,°\text{C}$. The T-history experiment was conducted to further validate the four corresponding compositions. A complete charging/discharging T-history cycle of the four compositions was illustrated in Figure 4.9.

When cooling at a static temperature (the temperature of the thermostat

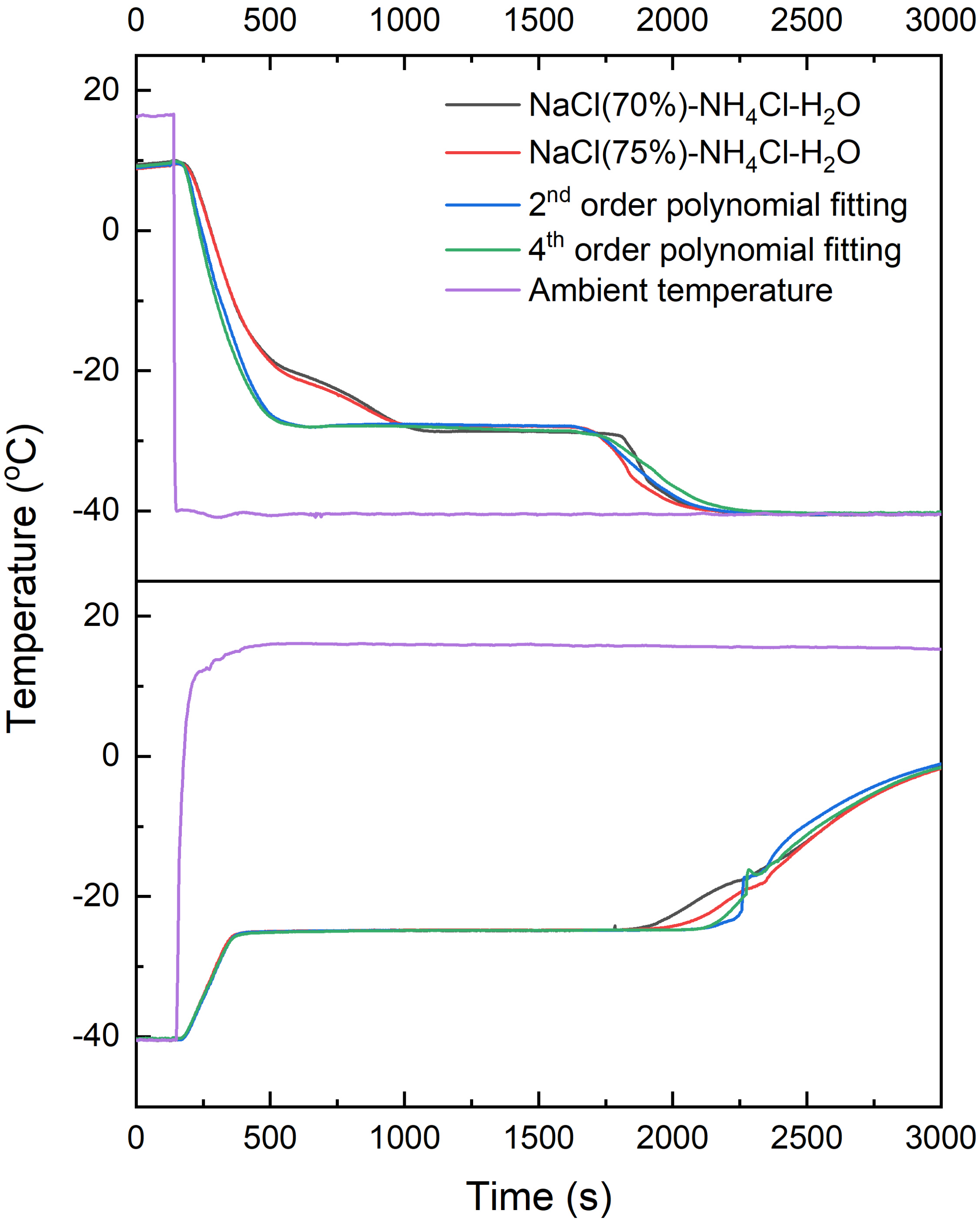

Figure 4.9: the T-history curves of the four compositions

bath is −40 °C), the 70% and 75% NaCl content groups show an asynchronous crystallisation. Their first pair of inflection points occur at ∼−21 °C which is the phase change temperature of eutectic NaCl solution. This indicates that the ice and NaCl crystallised from the solution first. The rest of the liquid freezes to solid phase subsequently and the temperature drops down to the eutectic temperature. On the other hand, 2nd and 4th order polynomial fittings appear similar crystallisation performance from ambient to eutectic temperature directly. It takes ∼50 mins to fully charge the PCMs that presented in these four curves. The charging time of the 2nd and 4th ordered polynomial fittings are slightly faster than the other two. The freezing temperature of these four compositions are ∼−28 °C, while the supercooling degree of the substance is 3 °C. For the discharging process, four compositions present similar melting temperature at ∼−24.8 °C, which agrees with DSC results. The length of the plateau represents the value of the latent heat. The evolution of the latent heat value is 2nd order polynomial fitting ≈ 4th order polynomial fitting > 75% group > 70% group.

Moreover, Figure 4.10 shows the experimental phenomenon of four compositions in the first completed charging/discharging cycle. According to Figure 4.9, after ∼ 1700 s, the charging process is completed. The sample temperature gradually drops down to the temperature of thermostatic bath.

The transparent liquid sample froze to white solid as illustrated in Figure 4.10 (left). The sample melts during the discharging process. Specifically, in Figure 4.10(b) (right), precipitate is observed in the solution after the thermal cycle. It indicates that the points on the 2$^{\text{nd}}$ order polynomial predicts over-saturated at the eutectic temperature. Hence the eutectic point of NaCl-NH_4Cl solution system was determined. 4$^{\text{th}}$ order polynomial composition is the eutectic composition of the ternary NaCl-NH_4Cl solution. The mass ratio of three components are: 18.54%, 7.29% and 74.17%, respectively.

The phase change temperature and latent heat of the eutectic ternary PCM is examined with DSC. As discussed in Section 3.1.1, because the results vary with different measurement protocols, in this experiment, the temperature program is set within 25 °C to −60 °C. The curves and values of sample are presented in Figure 4.11, Table 4.3, individually.

Table 4.3: The phase change temperature and latent heat values of eutectic NaCl-NH_4Cl solution

	Freezing temperature (°C)		Melting temperature (°C)		Heat of fusion (kJ/kg)	Specific heat (kJ/(K kg))
	Onset	Peak	Onset	Peak		
NaCl-NH_4Cl solution	-48.37	-46.85	-25.10	-18.55	226.42	3.25

The sample which went through a complete phase change process in DSC was crystallised first and then melted. A highly symmetric peak is shown

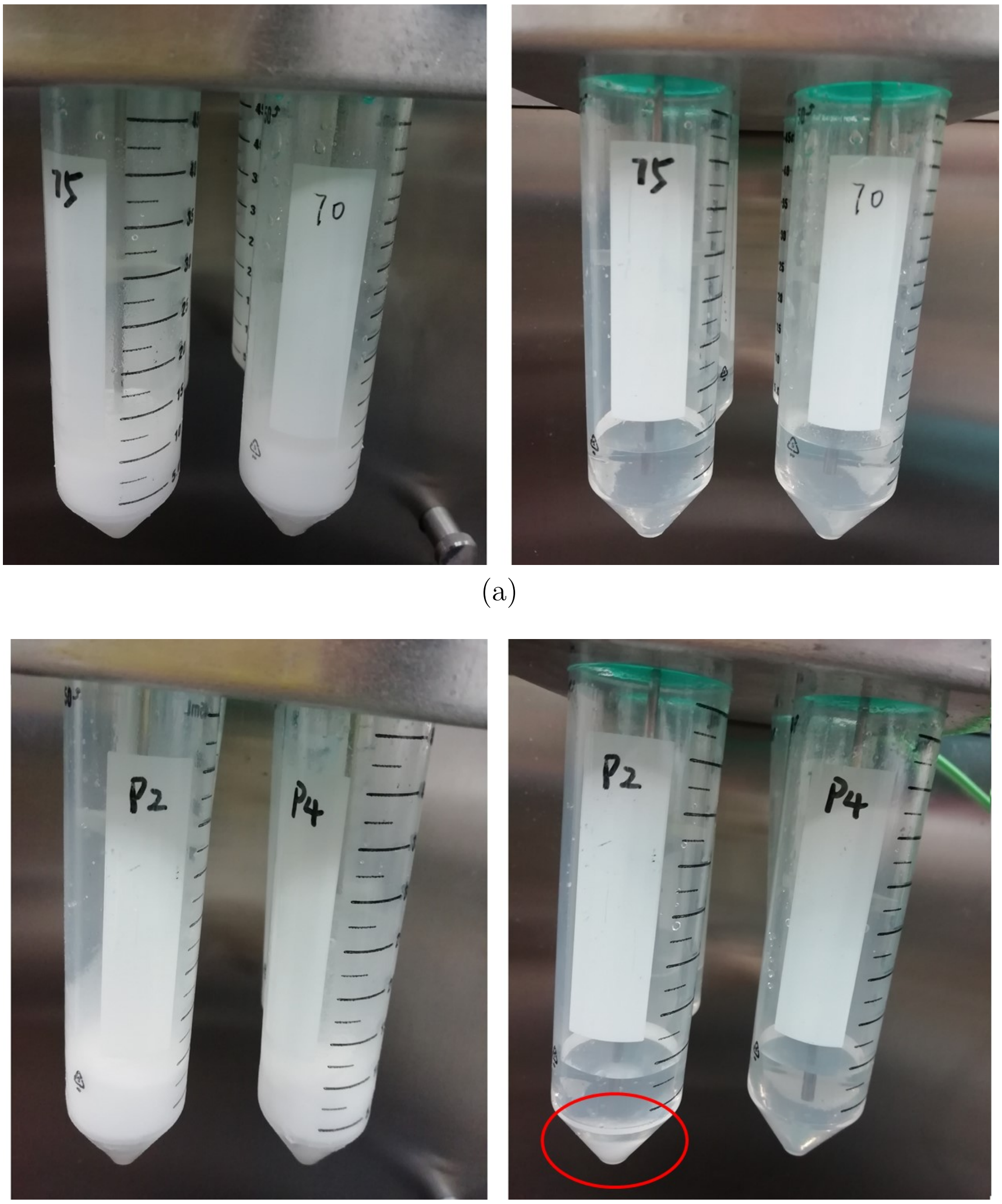

(a)

(b)

Figure 4.10: The experimental phenomenon of (a) 70% and 75% NaCl content groups and (b) 2nd and 4th ordered polynomial fittings after cooling and remelting

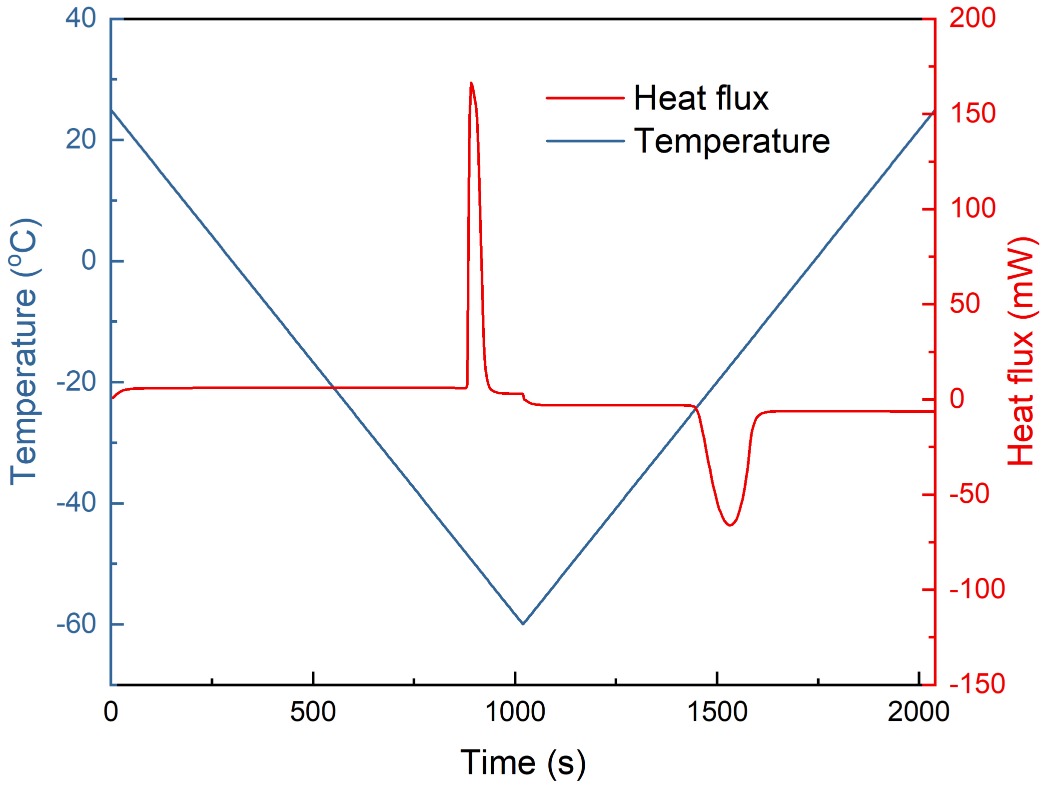

Figure 4.11: The DSC curve of the eutectic NaCl-NH_4Cl solution between 25 °C and −60 °C

during melting process, which indicated a congregate melting process. The reaction kinetics of the melting process is slower than crystallisation, which was indicated by exhibiting a broader peak in the melting process. The melting temperature of the eutectic NaCl-NH_4Cl solution is −25.10 °C with a fusion heat at 226.42 kJ/kg. The supercooling phenomenon occurred during cooling process, which results in an incompatible freezing and melting temperature. It will be discussed in Section 5.2.

4.1.2 Binary eutectic solution for −33 °C

As is mentioned in Section 4.1, binary eutectic $MgCl_2/H_2O$ solution is found suitable for −33 °C application. Multiple $MgCl_2/H_2O$ formulations that all are claimed to be the compositions were found in literature. In order to validate it, the $MgCl_2$ solution melting curves of different salt ratios are tested as presented in Figure 4.12 and Table 4.4.

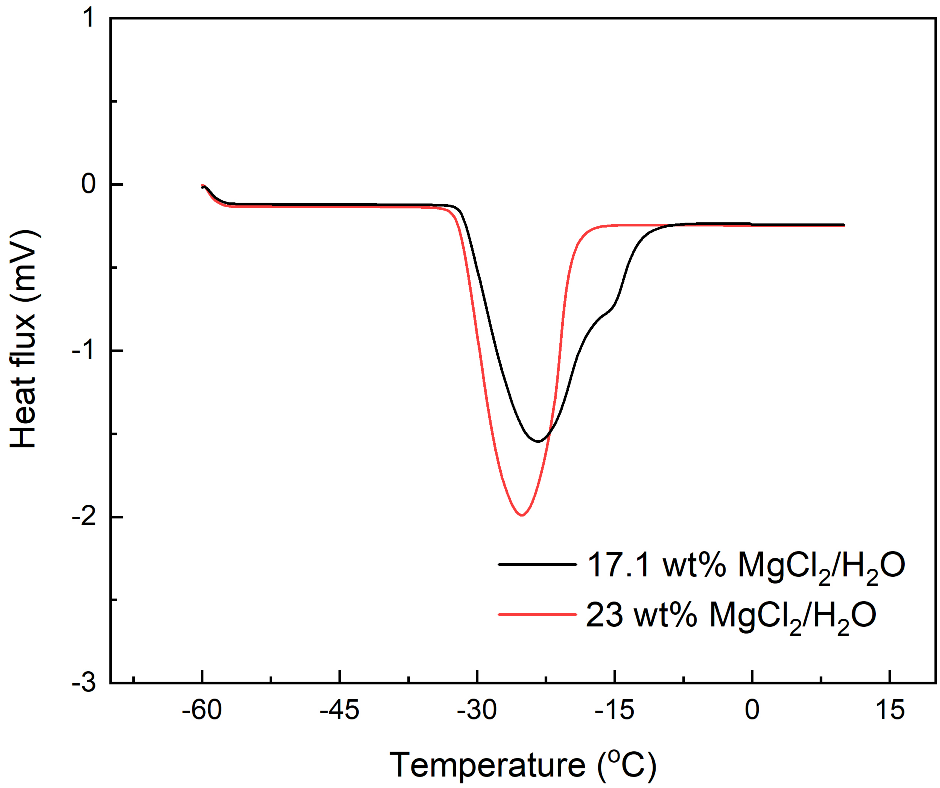

Figure 4.12: The DSC curve of $MgCl_2$ solutions with different salt ratios

Both samples have similar onset temperature near −33 °C. The one with 23 wt% $MgCl_2$ salt ratio displayed a symmetric phase change curve while the

Table 4.4: The thermophysical properties values of $MgCl_2$ solution

	Freezing temperature (°C)	Melting temperature (°C)	Heat of fusion (kJ/kg)
17.1% $MgCl_2$ solution	-52.72	-32.0	197.4
23% $MgCl_2$ solution	-48.37	-32.1	179.4

other shows multi-peaks. A conclusion can be drawn that 23 wt% $MgCl_2$ salt ratio is the eutectic composition of the $MgCl_2$ solution. The study also found that the supercooling degree and specific heat is negative correlated to the salinity of the salt-water based PCM.

However, there is a considerable difference between literature and experiment of the $MgCl_2$ solution latent heat value. One possible reason of it is that the $MgCl_2$ solutions are synthesised by dissolving the anhydrous $MgCl_2$ powder in distilled water. The hydrolysis of $MgCl_2$ in water is an intense exothermic reaction. Although double layer jacketed beaker with circulating water is used to control the temperature during the formulation process, it can be seen clearly that the loosely black precipitate is generated at the bottom of the solution, as is illustrated in Figure 4.13. This reaction also results in the releasing of HCl vapour from the solution. Hence It will effect the latent heat value of the sample and further result in the phase separation during the cycling. The chemical reaction can be represented by:

$$MgCl_2(s) + H_2O(l) \xrightarrow{\text{Heat}} Mg(OH)Cl(aq) + HCl(g)$$

Figure 4.13: The $MgCl_2$ solution after prepared by dissolving the anhydrous $MgCl_2$ powder in distilled water

$MgCl_2{\cdot}6H_2O$ is one of the hydrates of $MgCl_2$. It is stable under normal temperatures and pressures conditions. Accordingly, instead of anhydrous $MgCl_2$ powder, $MgCl_2{\cdot}6H_2O$ was employed in formulating $MgCl_2$ solution.

It is confirmed that the eutectic $MgCl_2$ solution formulated from $MgCl_2{\cdot}6H_2O$ has a reasonable latent heat value and no visible aggregation.

With 49 wt% of $MgCl_2{\cdot}6H_2O$ powder in distilled water, eutectic $MgCl_2$ solution is formed. The phase change temperature and latent heat are shown in Figure 4.14.

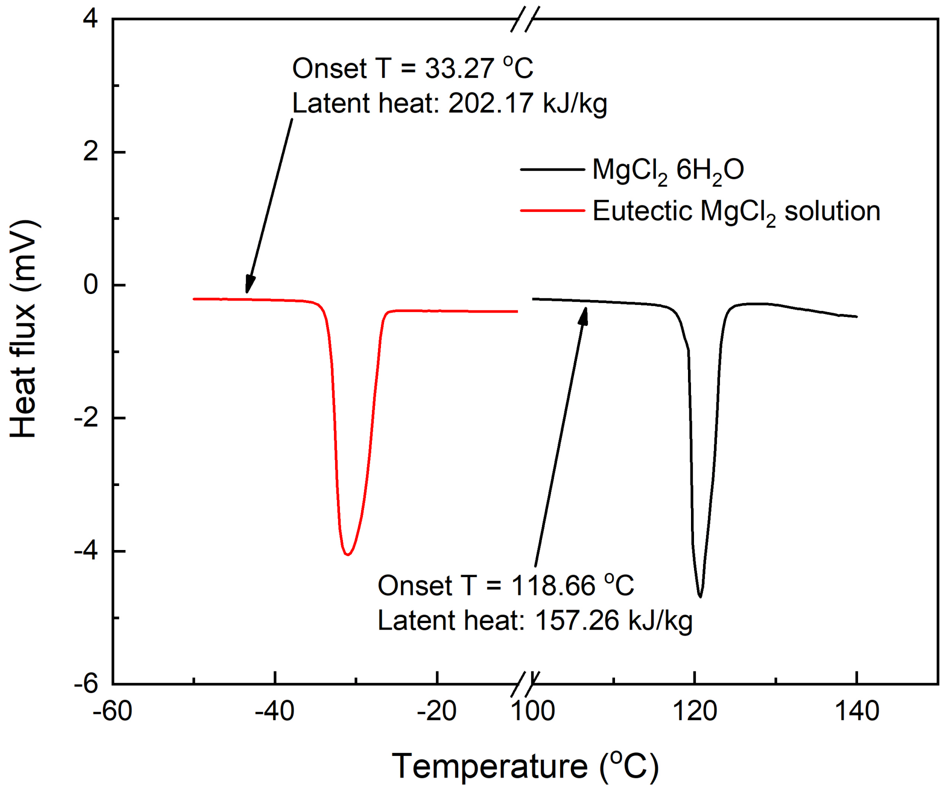

Figure 4.14: The phase change temprature and latent heat of $MgCl_2 \cdot 6H_2O$ and the eutectic $MgCl_2$ solution

Table 4.5: The phase change temperature and latent heat values of $MgCl_2$ solution

	Freezing temperature (°C)		Melting temperature (°C)		Heat of fusion (kJ/kg)	Specific heat (kJ/(K kg))
	Onset	Peak	Onset	Peak		
$MgCl_2$ solution	-74.99	-74.97	-33.38	-32.05	204.35	2.96

4.2 Eutectic point

The XRD analysis of the salt-water PCMs is conducted. Different crystallising temperature was applied for each sample based on their thermophysical properties. It is $-40\,^{\circ}\mathrm{C}$ for eutectic NaCl-NH_4Cl solution while $-60\,^{\circ}\mathrm{C}$ for eutectic $MgCl_2$ solution. The crystalline phase of both PCMs located at 10 to 60 2theta degree in the pattern was illustrated in Figure 4.15 and Figure 4.16, individually. Coloured arrows are introduced in the profiles to indicate the matching phases between standard materials and the eutectic systems.

The XRD patterns shows that eutectic NaCl-NH_4Cl solution consists of $NaCl{\cdot}H_2O$, NH_4Cl and ice. The eutectic $MgCl_2$ solution contains $MgCl_2{\cdot}12H_2O$ and ice. It can be seen from the XRD spectrum that although ice is a common component in both eutectics, it forms different structures due to the molecule interactions or under different temperate conditions.

4.3 Summary

The potential PCMs for both $-25\,^{\circ}\mathrm{C}$ and $-33\,^{\circ}\mathrm{C}$ vehicle transportation were investigated. Two most favourable salt-water based PCMs have been screened at each favourable temperature ranges: eutectic NaCl-NH_4Cl solution and eutectic $MgCl_2$ solution. A new approach for identifying the ternary eutectic point was illustrated in this chapter. It simplifies the experiment procedures and provides an accurate eutectic composition ratio. The phase change temperature and latent heat of the eutectic formulations were characterised by DSC. Their bulk material composition was detected by XRD.

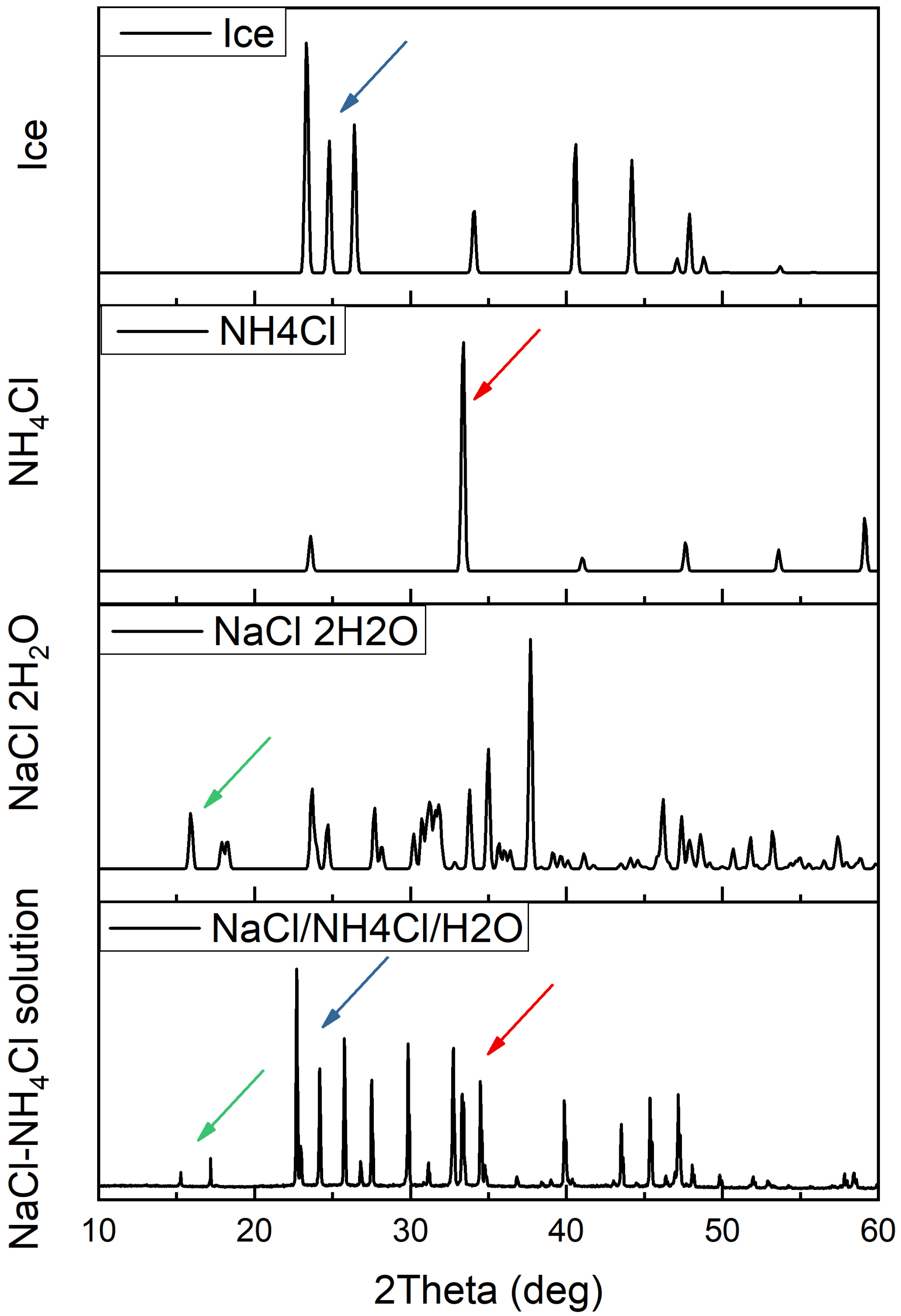

Figure 4.15: the XRD pattern of the NaCl-NH$_4$Cl solution system

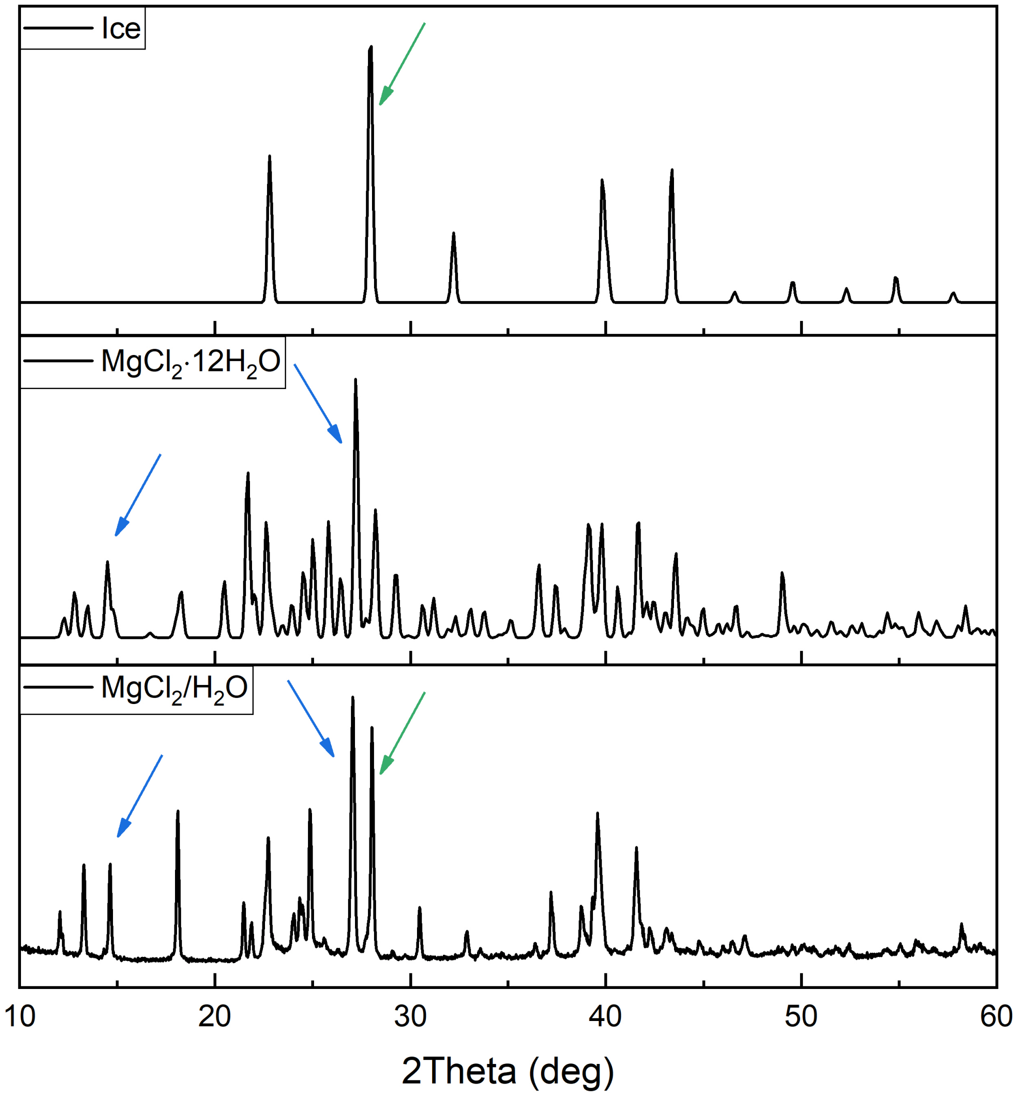

Figure 4.16: the XRD pattern of the NaCl-NH_4Cl solution system

CHAPTER 5

RESULTS AND DISCUSSION: THERMOPHYSICAL PROPERTIES CHARACTERISATION & ENHANCEMENT

This chapter discusses the thermophysical properties of PCMs observed in experiments as well as the enhancing and optimisation method. Section 5.1 discusses the the thermal conductivity enhancement introduced by adding graphite based enhancers. Section 5.2 shows the effective methods of suppressing supercooling in the PCMs. Section 5.3 exhibits that the introduction of thickening/gelling agent can improve the stability of PCMs. Section 5.4 shows the corrosion effect of PCMs on four common used metal materials.

5.1 Thermal conductivity & specific heat

With the screening process of eutectic salt-water solutions, further steps are taken to suppress the negative impact. Generally, low thermal conductivity hinders the heat storage and release rate of the PCM (Qureshi, Ali, and Khushnood, 2018). Because graphite is widely recognised as a thermal conductivity enhancer, it is introduced into PCM system in this study.

NaCl-NH_4Cl-H_2O ternary systems with different shapes of graphite are compared and tested: graphite powder (GP), graphite flakes, expanded graphite powder (EG). Four composites with 0.5 wt%, 1%, 2% and 4 wt% of each graphite enhancer were mixed with the ternary solution, respectively.

It can be observed in the diagrams, the flake-state graphite segregates as soon as it is added into the solution whilst graphite powder with relatively smaller particle size is well dispersed. Hence, in order to get a homogeneous system, powder state graphite was selected as thermal conductivity enhancer.

The thermal conductivity experiment was conducted with LFA. As explained in Section 3.1.3, their specific heat needs to be tested in advance. Table 5.2 presented the DSC results of each samples.

The phase change temperature, latent heat and specific heat of the ternary solutions decrease by introducing foreign graphite particles. The more graphite added in the ternary system, the lower the latent heat is. It is because this

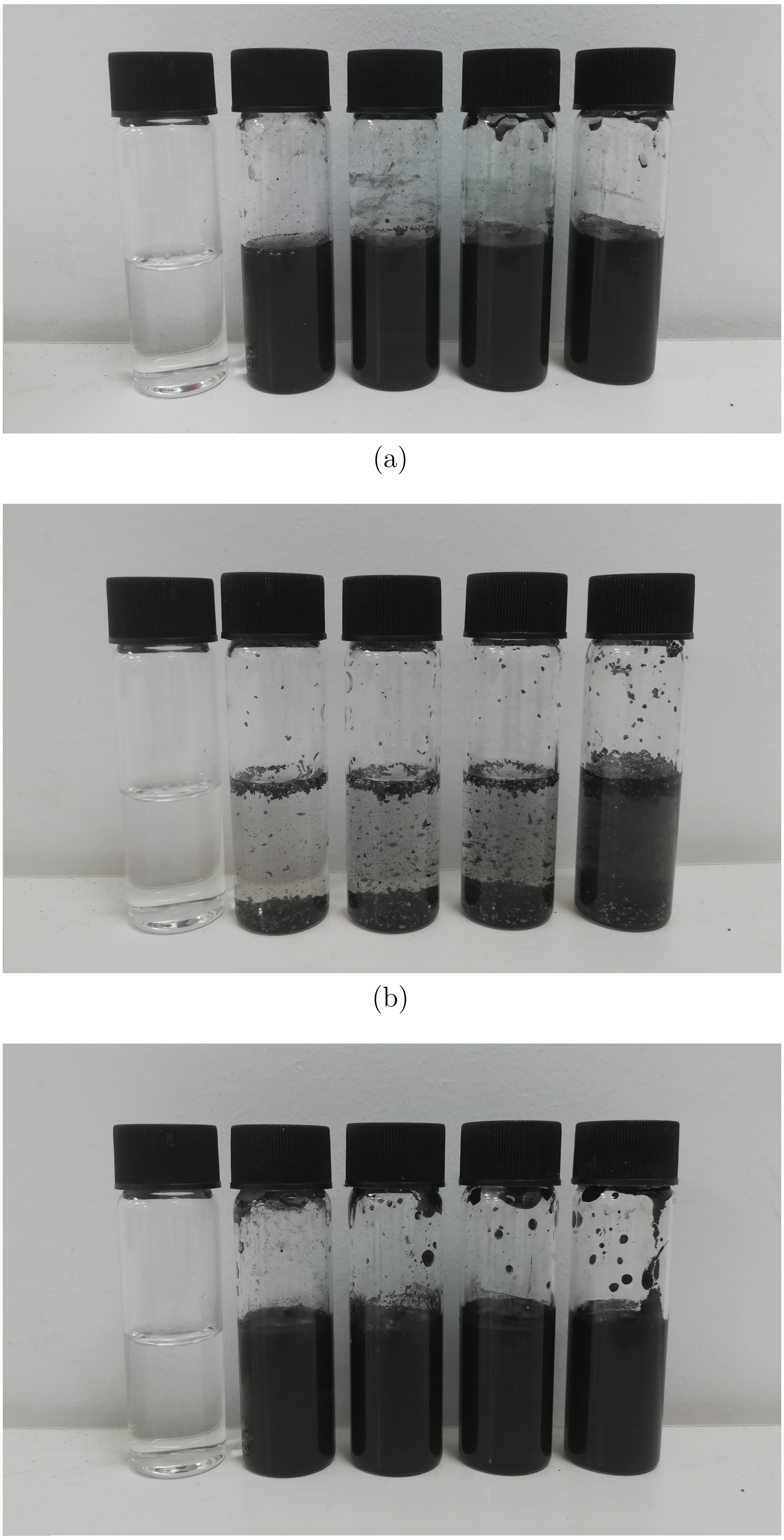

(a)

(b)

(c)

Figure 5.1: The thicken performance by adding graphite powder (a) graphite flake (b) and expanded graphite powder (c)

Table 5.1: The effect of the nucleating agent on the supercooling degree of composite $NaCl\text{-}NH_4Cl$ solution system

Material	Phase change temperature (°C)	Latent heat (kJ/kg)	Specific heat (kJ/K kg)
$NaCl\text{-}NH_4Cl\text{-}H_2O$	-25.10	226.42	3.25
+0.5% GP	-25.47	224.40	2.66
+1% GP	-25.44	223.62	2.85
+2% GP	-25.43	217.59	2.92
+4% GP	-25.49	217.18	2.56
+0.5% EG	-25.29	223.96	2.61
+1% EG	-25.30	217.81	2.93
+2% EG	-25.32	194.77	2.89
+4% EG	-25.35	171.71	2.56

composite contained one active ingredient, ternary salt solution. The smaller PCM ratio in the system is, the less latent heat it will release. GP shows less effect on the latent heat value compared to EG. With 4% GP, the latent heat of ternary system decreased 4.1% whereas in the case of 4% EG, it is increased to 24%.

The thermal conductivity of ternary systems with the aforementioned different powder graphite content was tested with LFA at ambient temperature. Their thermal diffusivity data was compared in Figure 5.2.

Both GP and EG help increase the thermal diffusivity of $NaCl\text{-}NH_4Cl$ solution considering the error bars. The former shows a larger diffusivity

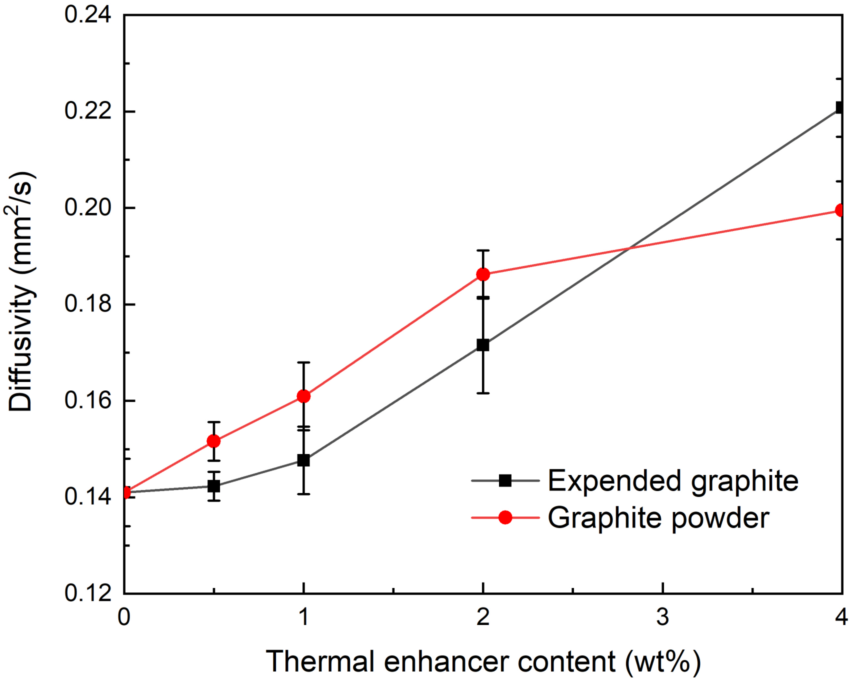

Figure 5.2: The diffusivity increment of NaCl-NH_4Cl-H_2O system with various expanded graphite/graphite powder contents

increase with less than 3% graphite added. The introduction of 0.5% GP enhanced the thermal diffusivity of NaCl-NH_4Cl solution by 7.5%. When the content of GP is 4%, the thermal diffusivity of the solution is increased by 41.5%. 1% of EG does not make significant impact on the diffusivity enhancement.

In addition, as shown in Table 5.2, the more thermal conductivity enhancer is added, the less energy density of the composite ternary PCM system is. As a result, GP is more preferable than EG with small portion. The thermal diffusivity of the composite PCM rises by 22% with 2% GP with little latent heat and specific heat reduction. The thermal conductivity of this composition is 0.65 W/m K.

Based on the experiment results above, 2% GP was also added into $MgCl_2$ solution to increase its thermal conductivity. The thermoproperties of the composite is shown in Table 5.2. The thermal conductivity of the composite $MgCl_2$ solution is 0.66 W/m K, which increased by 24.5% compared with the original binary solution.

Table 5.2: The effect of the nucleating agent on the supercooling degree of composite $MgCl_2$ solution system

Material	Phase change temperature (°C)	Latent heat (kJ/kg)	Specific heat (kJ/K kg)	Thermal conductivity (W/m K)
$MgCl_2$-H_2O	-33.22	201.03	2.96	0.53
$MgCl_2$-H_2O +2% GP	-33.32	199.89	2.74	0.66

5.2 Supercooling

Supercooling is the inherent disadvantage of the water based PCM. The supercooling degree of the material is affected by several factors, for instance, the cooling rate, thermal conductivity of the container and sample, etc. Milligrams of sample examined by DSC is not enough to provide an accurate supercooling value as illustrated in Section 2.3.3. Therefore, in this study, the supercooling is studied by T-history method.

$NaCl$-NH_4Cl solution system

Figure 5.3 presented the supercooling results of NaCl-NH_4Cl solution obtained with T-history method. The rapid cooling method was applied in the T-history process, in which 10 g sample was immerged directly in the $-40\,^{\circ}C$ thermostatic bath. After the crystallisation process finishes, the temperature of the sample increases and eventually reach the ambient temperature when it is left in the environment.

Generally, the supercooling degree is defined as the difference between the melting and crystallisation temperature. However, if the studied substance is a mixture or composite, and the freezing temperature is lower than the melting temperature as is illustrated in Figure 2.16 (c), it is hard to identify and define the supercooling effect. In Yinping and Yi's research (Yinping and Yi, 1999), both melting temperature and supercooling temperature are determined by the cooling curve, which is later adopted by many researchers. Hence the supercooling degree in this study will be validated using this method.

A simultaneous crystallisation can be observed in the temperature decreasing stage. The supercooling peak appears during the first cycle at $\sim 2\,^{\circ}C$. Then the plateau during cooling process indicated that the crystallisation of the ternary solution occurs at $-28.07\,^{\circ}C$. It is $3.24\,^{\circ}C$ lower than the melting temperature. The charging process is finished when the temperature starts

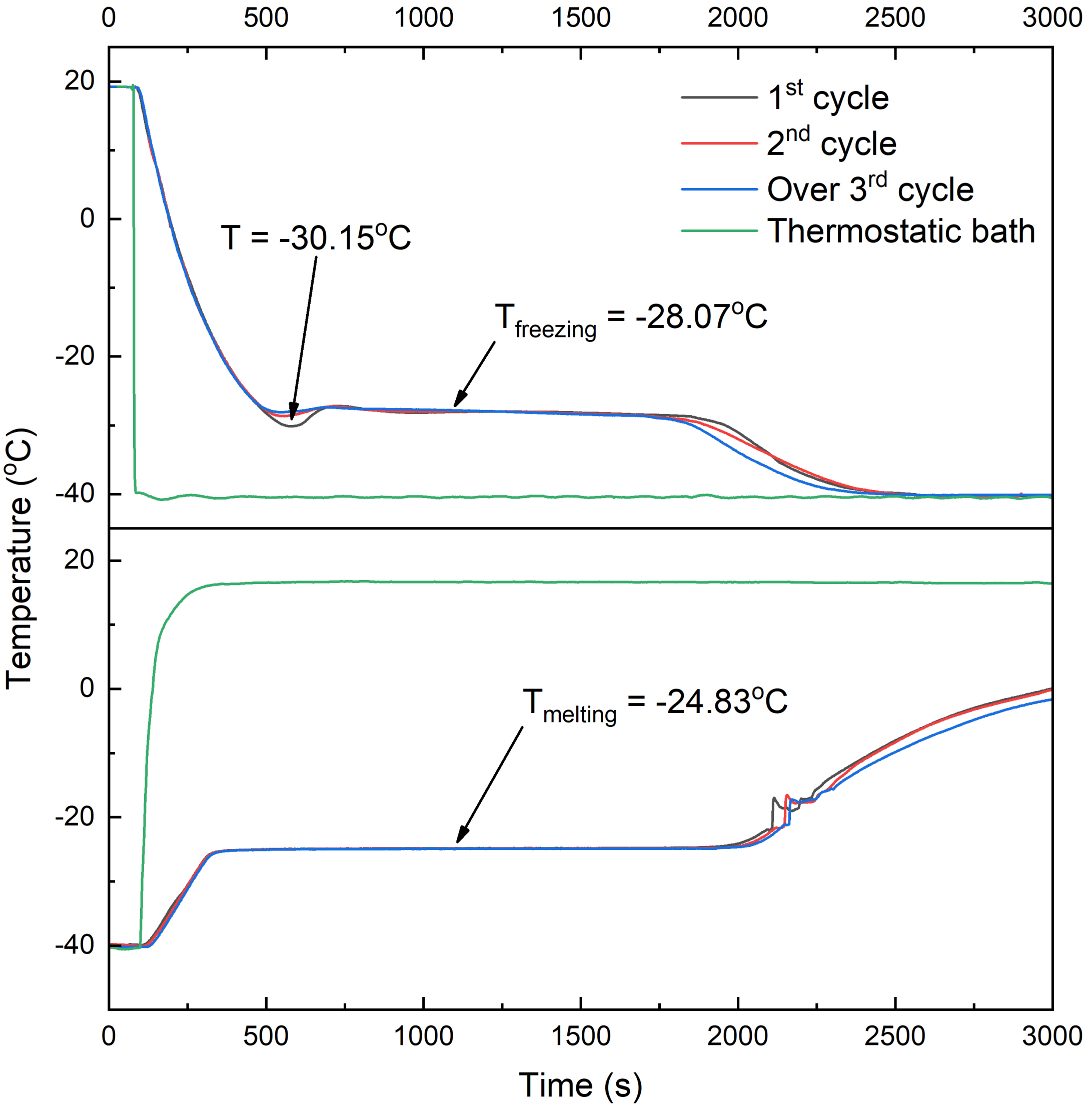

Figure 5.3: The first three charging/discharging cycles of NaCl-NH_4Cl solution

to decrease again. The temperature of the system gradually decreased to the temperature of thermostatic bath.

The supercooling degree reduces with the increase of cycling times, which results in the decrease of charging time. It is due to the triggered solidification by thermal history theory. Over the third cycle, the supercooling degree tend to be suppressed and the charging profile is more consistent. Under the influence of a lesser supercooling degree, the charging time reduced. The whole charging time of the 10 g sample from 20 °C is ~30 mins.

The T-history experiment result shows that the supercooling of the NaCl-NH_4Cl solution is effectively suppressed and therefore will not be further optimised in this study.

$MgCl_2$ solution system

It is reported that $MgCl_2$ solution has a large supercooling degree of 9–14 °C (Toner, Catling, and Light, 2014). Figure 5.4 investigated the crystallisation behaviour of the $MgCl_2$ solution at different charging temperature. The melting temperature of $MgCl_2$ solution is −33 °C. The charging temperature of the thermostatic bath was set at −45 °C, −50 °C and −60 °C for different tests.

The temperature of the samples drops steeply at first. The cooling rate is proportional to the temperature gradient between sample and thermostatic

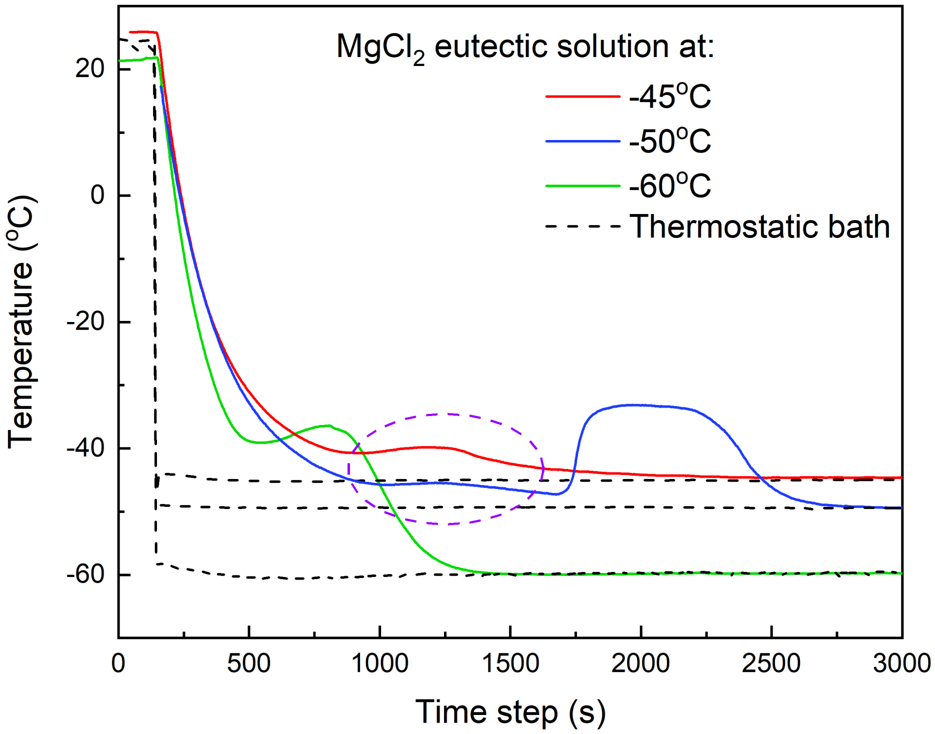

(a)

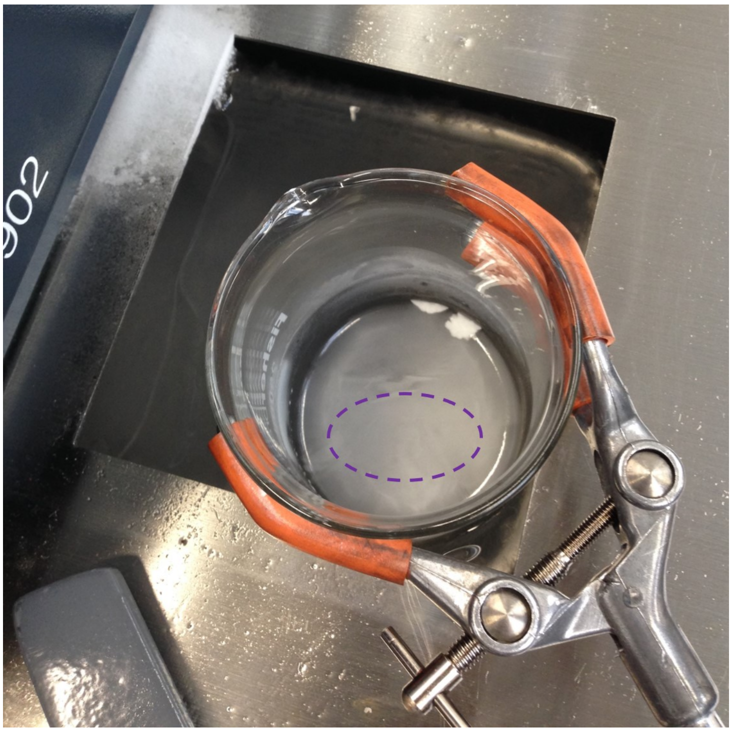

(b)

Figure 5.4: The T-history curves of $MgCl_2$ solution with different charging temperature (a) the amorphous state of the solution

bath. $MgCl_2$ solution does not crystallise with −45 °C charging. However, the temperature did not decrease directly to the thermostatic bath temperature. Instead, a small plateau is generated as illustrated in the purple dash circle area. The temperature is lower than the phase change temperature of $MgCl_2$ solution, but not low enough to overcome the barrier of supercooling. As a result, a opaque glass transition like amorphous (non-crystalline) solid was formed because of lacking of nucleus (the purple dash area as shown in Figure 5.4(b), which is in contrast to the stable crystallisation at top right corner). This phenomenon was reported by Moore and Molinero (2011) with supercooled water solution. Salt-water solution has the similar impact. Small amount of heat was released during this process and effected the trend of the cooling curve.

With a cooling temperature at −50 °C, the decreasing trend of the temperature curve is similar with previous temperature conditions for the first 28 mins. After it went through the amorphous solid state, the temperature keeps decreasing to −47.3 °C, the crystal nucleus appeared and solution started freezing. Normally, the cooling rate is governed by the velocity of nucleation and crystal growth rate. At this stage, the formation of the crystalline nucleus is spontaneously and arbitrarily. Nonetheless, with the generating of the nucleus, $MgCl_2$ solution crystallises and releases latent heat. It indicates that the formation of ice crystals brings uncertainty of the cooling process and hinders the cooling rate of the salt solution. Latent heat is released during phase change transition. The temperature of the solution rose to −33.3 °C then gradually decreased to thermostatic bath temperature.

Further lower the cooling temperature of the thermostatic bath to −60 °C, a typical cooling curve of $MgCl_2$ solution can be obtained with a crystallisation temperature of −40 °C. The nucleation occurs immediately after the solution temperature is lower than the supercooling temperature.

The different evolution of these three cooling curves indicate that the supercooling degree varies with different charging conditions. Although a faster charging rate will be achieved with a lower supercooling degree, as discussed in Section 2.3.3, it will result in the demand of more energy input which will lower the SOP and increase the system complexity. Therefore, the criteria of solution nucleation are:

- The charging temperature is lower than supercooling temperature;
- A sufficient temperature variation between the charging device and material to provide the driving force for the nucleation

Since extra energy input is essential for interior nucleation to occur in a uniform substance, foreign seedings can be introduced into the solution system to accelerate the hetenucleation.

The new $MgCl_2$ solution was formulated with tap water instead of distilled water. Samples are cooled with thermostatic bath to ensure the fully growth of the crystal (Li et al., 2019).

Graphite, borax, MgO and diatomite earth are selected as nucleation agents in this study. 0.5% of nucleating agent was added in each eutectic solution. In addition, the $MgCl_2$ solution was made by tap water instead of distilled water to ensure crystallisation and improve crystallisation rate.

As illustrated in Figure 5.5. $MgCl_2$ solution crystallised under $-50\,°C$ with a $15.3\,°C$ supercooling degree. With the adding of different nucleation agents, the supercooling degree of composite $MgCl_2$ solutions varies. Graphite, borax and diatomite have a positive effect on supercooling suppressing and diatomite has the best performance over graphite and borax. It decreases the supercooling of $MgCl_2$ solution to $7.2\,°C$. Graphite is following closely with a supercooling degree of $8.4\,°C$. With the adding of Borax, the supercooling degree of $MgCl_2$ solution decreased by $7.2\,°C$. The addition of 0.5% MgO, on the contrary, increases the the supercooling degree of $MgCl_2$ solution.

The supercooling reduction is not only related to the type of nucleation agent, but also its mass ratio in the system. Figure 5.6 shows the crystallisation performance of composite PCM system with different graphite in various proportions. The decrease of supercooling is directly proportional to the

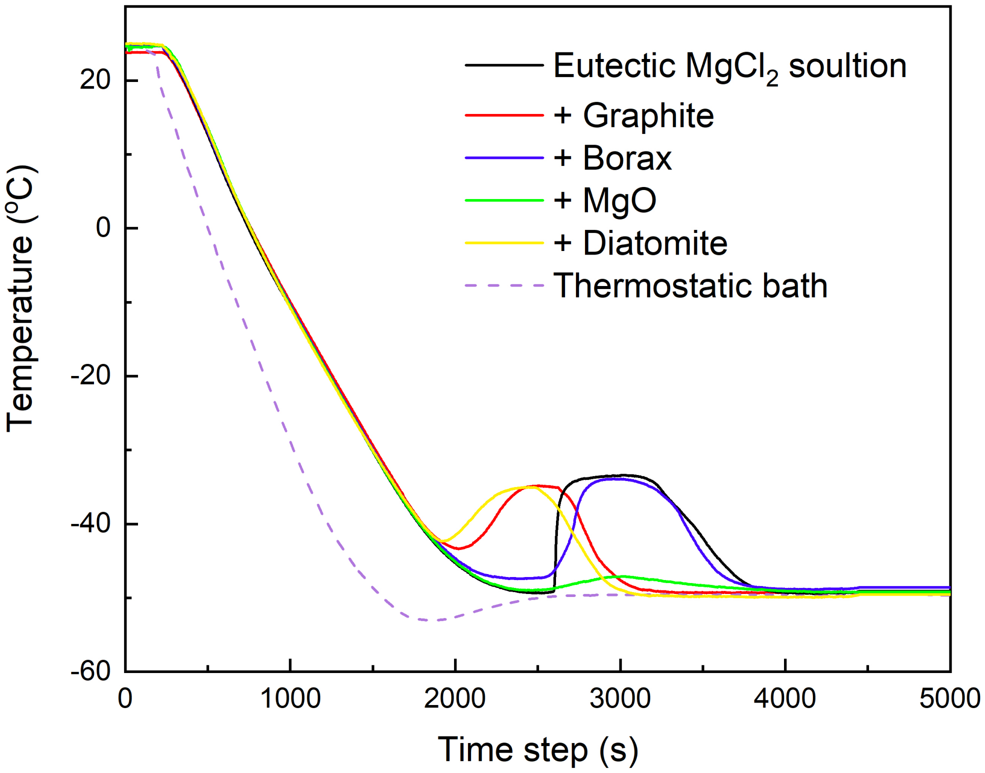

Figure 5.5: The cooling curve of eutectic $MgCl_2$ solution with different nucleating agents at −50 °C

graphite content. It is 3.62 °C lower with the presence of graphite and decreased slowly with the increase of graphite percentage of the system.

However, as stated in Section 2.3.3, charging at −50 °C will compromise the COP of the system. Therefore, temperature of the thermostatic bath was increased to −45 °C. The impact of diatomite and graphite was further tested since they performs well in previous tests.

As is reflected in figure Figure 5.7, when the content of both diatomite and graphite are 0.5%, the diatomite composite solution crystallised with

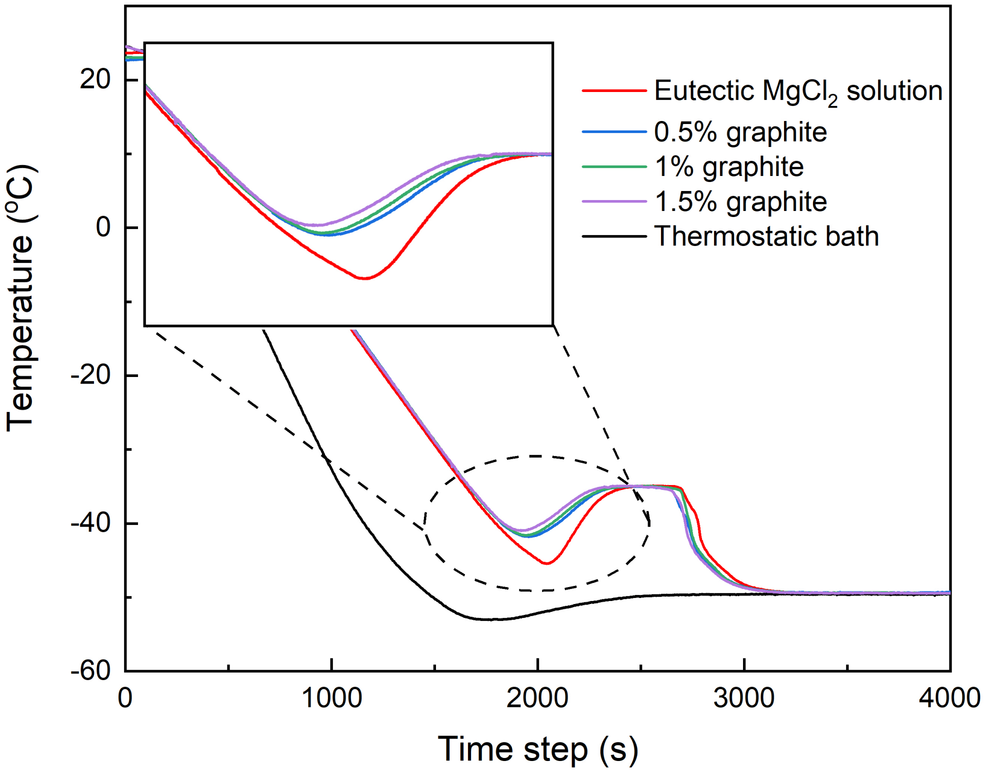

Figure 5.6: The supercooling degree reduction of composite MgCl2 solution with various graphite content

6.78 °C supercooling degree whereas graphite composite solution transitioned into an amorphous state.

In addition, the mass ratio of diatomite affect the supercooling degree of the composite PCM. There is no obvious effect with 0.1% diatomite addition. With the increase of the diatomite, the supercooling degree of the composite solution decreased and the charging time was reduced. It suggests that 0.2% is the minimum weight percent of diatomite addition that decreases the supercooling of MgCl2 solution, where the supercooling degree is 7.24 °C.

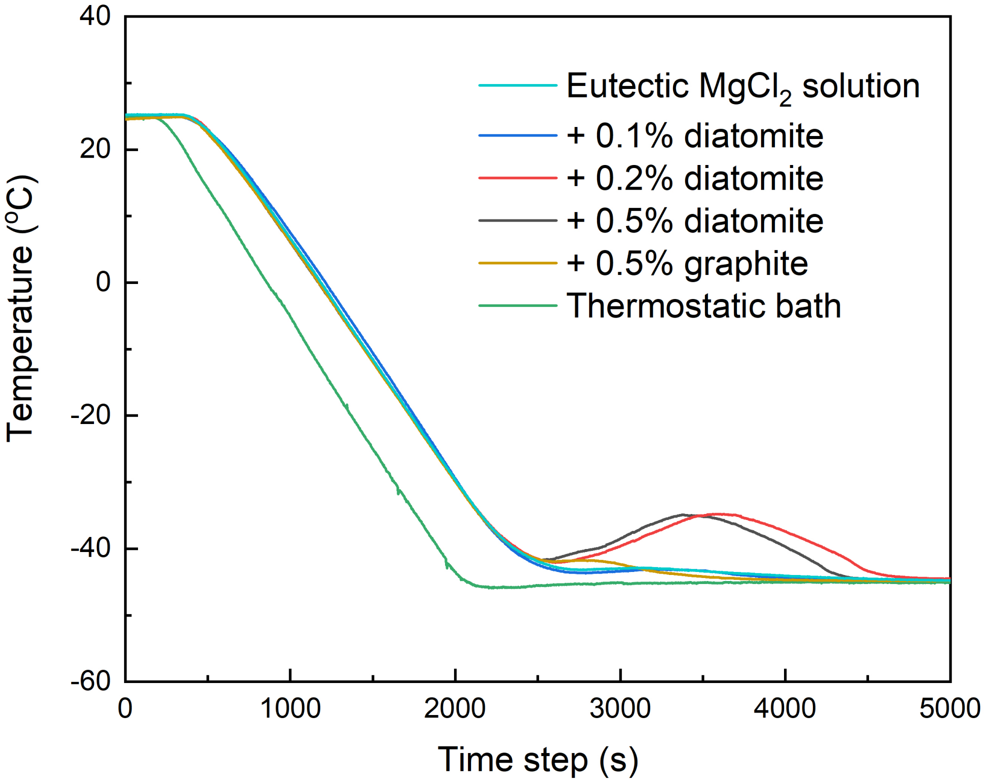

Figure 5.7: The cooling curve of eutectic $MgCl_2$ solution with different nucleating agents at −45 °C

Therefore, by mild temperature decreasing method, the composite solution can be charged at −45 °C. The charging time of 10 g composite solution from ambient temperature is estimated to be 50.6 min, whereas it is 22.8 min with −50 °C.

5.3 Stabilisation

The adding of thickening/gelling agent helps suspend the foreign solid particles, reduce the phase separation and stabilise the PCM system. The suitable water soluble thickening/gelling agent for salt-water based PCM was investigated.

NaCl-NH_4Cl solution system

The candidate agents were introduced to NaCl-NH_4Cl solution system and their thickening phenomena are observed and illustrated in Figure 5.8. The first five groups are mixed with different agents: tween 80, fumed silica 7 nm, fumed silica 200 nm, gum Arabic and polyacrylamide (PAM). The synergy effect among multi-agent is tested in last two groups with silica + PAM, silica + gum Arabic, respectively. The amount of each agents added is 2 wt%. Then the sample bottles were turned upside down simultaneously. Composite solutions flowed downward under gravity. Finally, samples were rested for 7 days in order to exam the system stability.

As shown in Figure 5.8. Tween 80, gum Arabic have little influence on the viscosity of the composite solution system. Fumed silica shows a limited effect on increasing the viscosity of the solution. The aggregated silica particles were observed separating out from the system after one week. Comparing group 2 and 3, fumed silica particle in smaller size has better suspension stability. However, it is still separated from the solution. Polyacrylamide

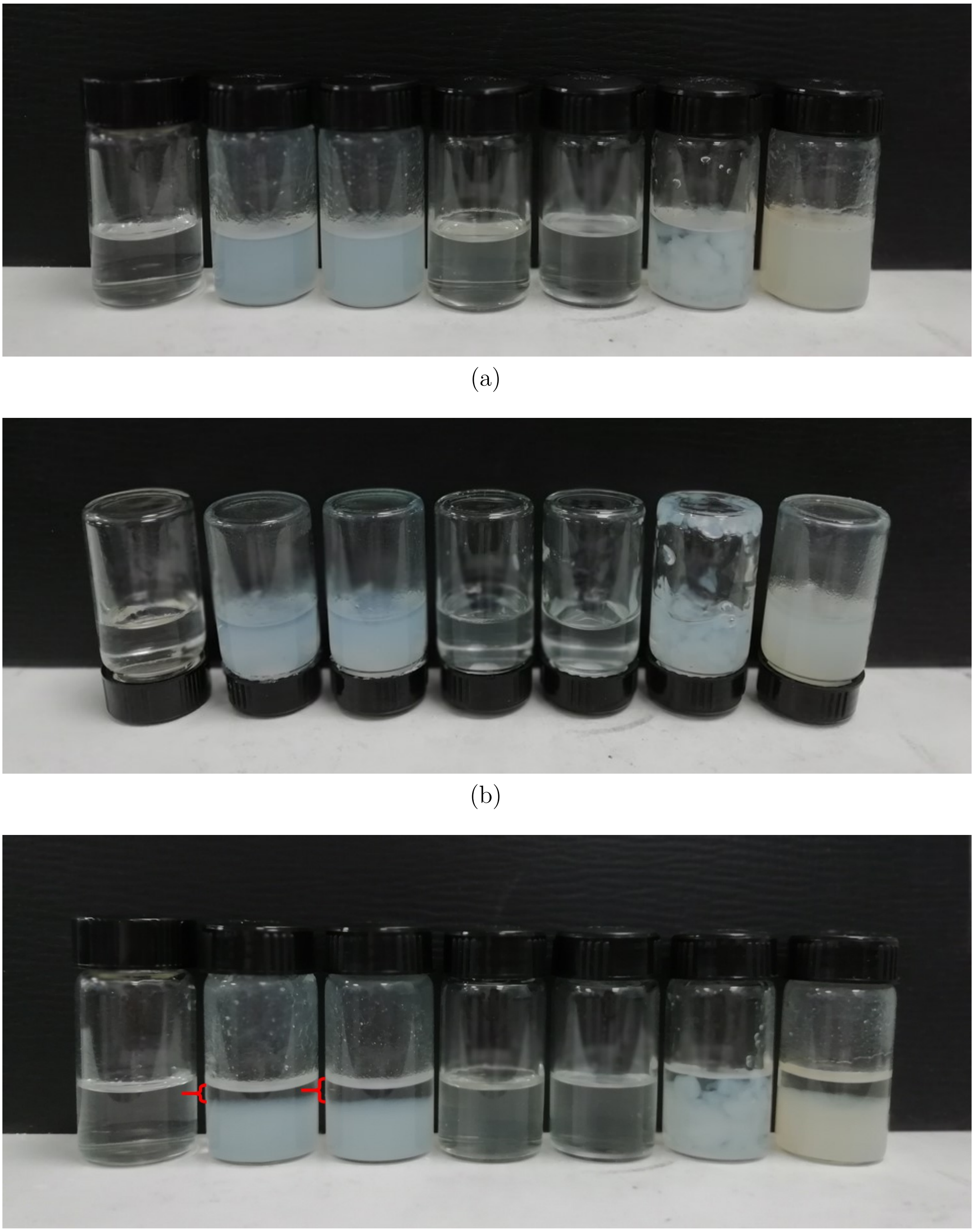

(a)

(b)

(c)

Figure 5.8: The phenomenon of adding different agents in the ternary solutions and the difference after resting seven days. From left to right: tween 80, fumed silica 7 nm, fumed silica 200 nm - 300 nm, gum Arabic, polyacrylamide, silica + PAM, silica + gum Arabic

exhibits good thickening ability and maintained the solution a uniform system after it was left stand for 7 days. When adding multi-agent, the presence of fumed silica causes the coagulation in the silica-polyacrylamide group. This is because that the hydrolysis of the amide groups in polyacrylamide build an irreversible bridging among silica particles (Maurya and Mandal, 2016). They trapped part of the salt-water solution and separated it from the homogeneous system. Another group of multi-agent also presented a noticeable separation after settlement. It is observed that by adding multi-agent, different agents interact with each other and decrease the system stability.

Following this particular procedure, similar experiments using thickening/gelling agents were conducted by other researchers. By applying this procedure, a stable homogeneous NaCl-NH_4Cl solution based systems can be formed with the following agents: xanthan, starch potato, polyacrylamide and carboxymethyl cellulose (CMC).

To form a stable and uniform NaCl-NH_4Cl solution system, a gel-like structure which is capable of confine or reduce the mobility of PCM is required. The composite solutions with thickening/gelling agents with the mass ratio from 2% to 6% is demonstrated in Figure 5.9.

When the bottles are upside down, the viscosity of the solutions can be compared by observing the falling speed of the liquid. The first two groups

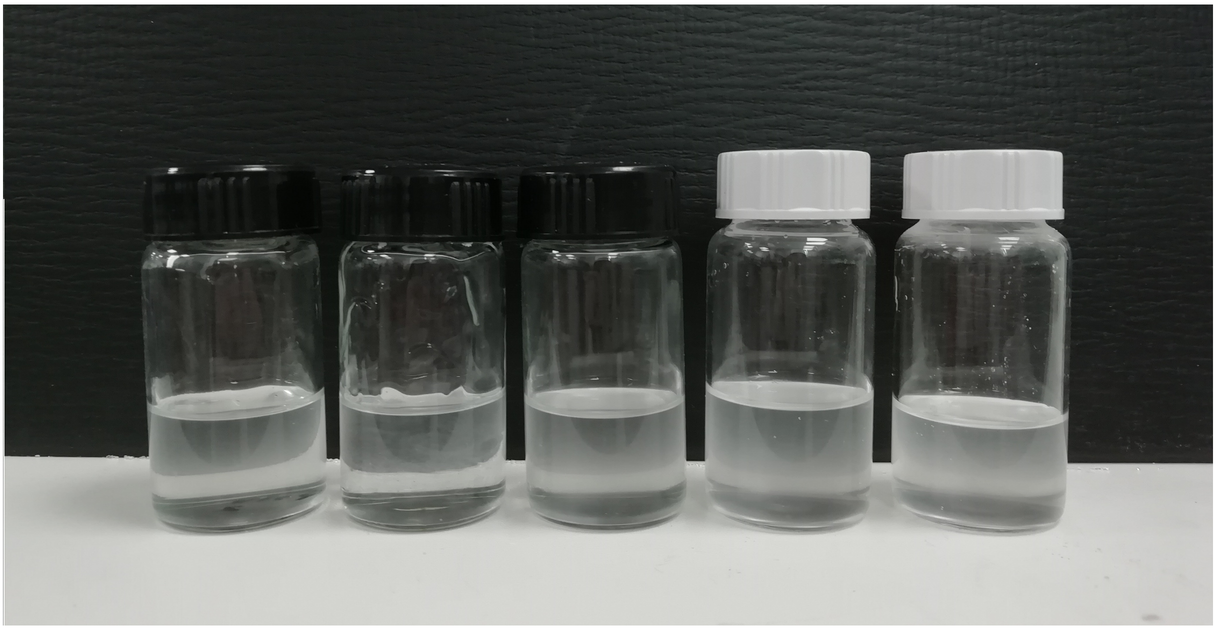

(a)

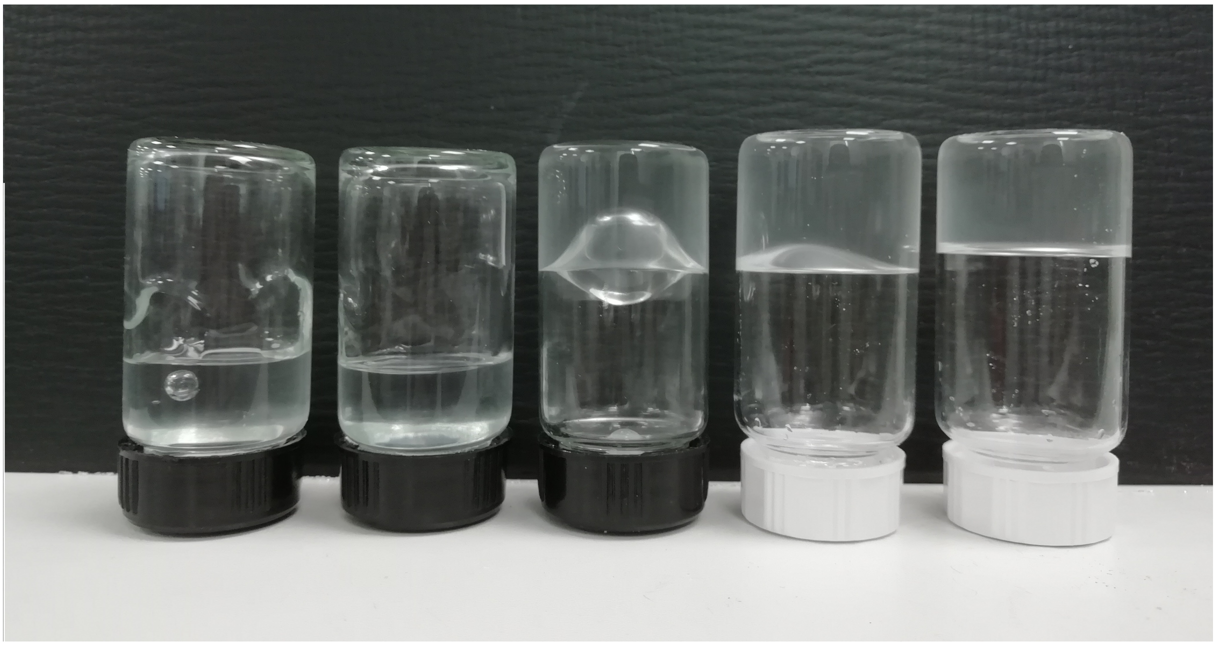

(b)

Figure 5.9: The thicken performance by adding 2%, 3%, 4%, 5%, 6% (from left to right) of polyacrylamide in the eutectic ternary solution. bottle upward (a) downward (b)

of solution falls directly after turning. There are air bubble generated in the 2% group due to the rapid motion. When the weight percentage of thickening/gelling agents is larger than 4%, solution shows slower mobility. 6% group sat still at the bottom of the bottle.

The mobility of the solution is negative correlated to the agent mass ratio. However, thick liquid cause aggregation of ingredients during formulation. Besides, lacking of mobility cause difficulties in filling PCM into containers. In this case, 4% is the favourable ratio because it exhibits good stability that meet the project demand and enough mobility to be filled in a container.

With the adding of 4% of starch potato, polyacrylamide, CMC and xanthan, respectively, the thickening performance is compared in Figure 5.10 after resting 7 days. For starch potato specifically, the heating effects was also studied in this experiment.

Compared with the first two groups, starch segregated at the bottom of the bottle after mixing directly with the NaCl-NH_4Cl solution whereas introducing high temperature during mixing helps build inter-molecular hydrogen bonding within starch. With the help of the entangled network, a uniform system is formed and it prevents starch from segregation. As regards four thickening agents, polyacrylamide and xanthan groups represented significant fluidity reduction compared to starch potato and CMC groups with the same mass ratio. Their thickening capability is: xanthan > polyacrylamide > CMC > starch potato (heated) > starch potato.

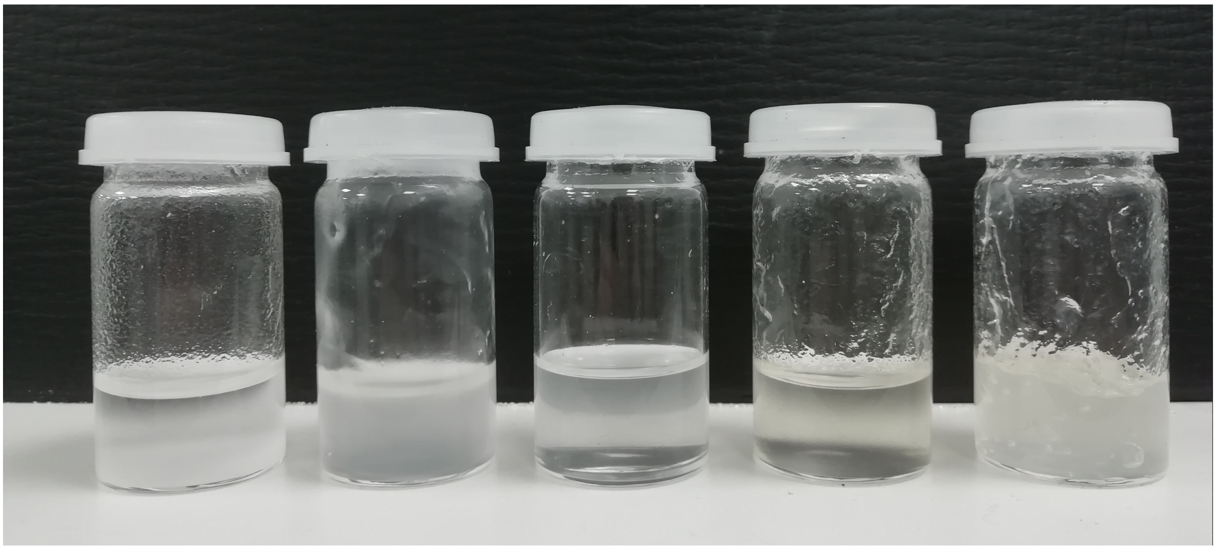

(a)

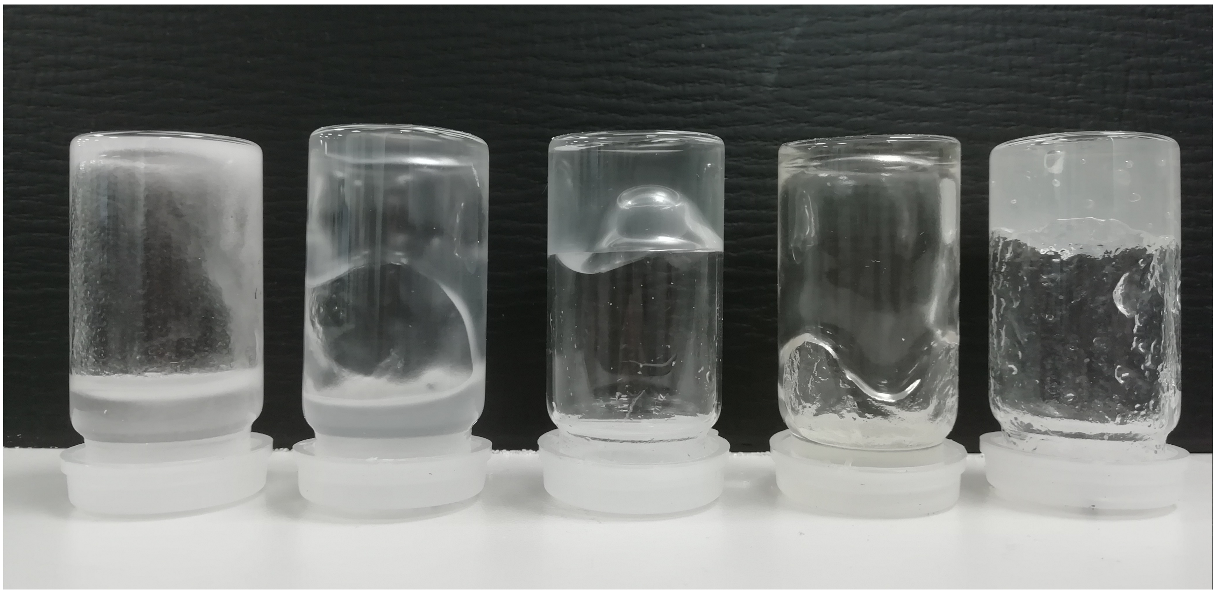

(b)

Figure 5.10: The thicken performance by adding starch potato, starch potato (heated), polyacrylamide, CMC, xanthan in the ternary solution after resting 7 days . bottle upward (a) downward (b)

Xanthan is widely used in food applications because of its good solubility in either hot or cold solutions. It shows high viscosity and excellent thermal stability. 4% of xanthan is selected to be the thickening/gelling agent for NaCl-NH_4Cl solution.

$MgCl_2$ solution system

Diatomite is added into $MgCl_2$ solution to suppress the supercooling effect. As a solid compound, it separates itself from liquid phase. This issue can be suppressed by adding stabilisation compounds.

The effect of both surfactants and thickening/gelling agents was investigated. Those consist of cation Cetylpyridinium chloride (CPC), anion Sodium dodecyl sulfate (SDS), water soluble non-ionic Polyethylene glycol (PEG) and Poly(vinyl alcohol) (PVA). Three thickening/gelling agents that showed good performance in previous experiment: polyacrylamide, xanthan, CMC. The adding quality is 2 wt%. Result shown in Figure 5.11.

Diatomite is light yellow in the solution. The dispersion can be distinguished from the colour distribution of the solution. It is indicated that all the surfactants are not sufficient for suspending diatomite particles. As for the thickening/gelling agents, although polyacrylamide thickened the solution, the cross-link structure created by polyacrylamide cannot fully suspend diatomite. CMC and xanthan can maintain an uniform composite system.

In addition, increased solution viscosity affects the supercooling degree of the solution. Therefore, the supercooling of composite $MgCl_2$ solution system

(a)

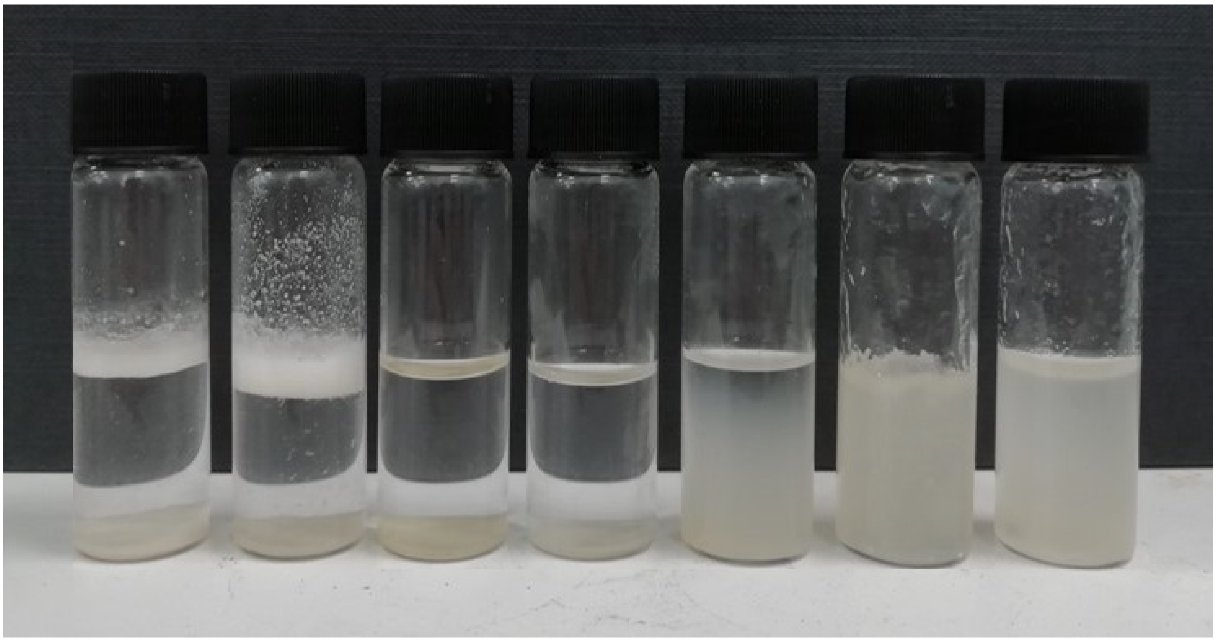

(b)

Figure 5.11: The stabilisation of $MgCl_2Cl$ solution with 2% CPC, SDS, PEG, PVA, polyacrylamide, Xanthan, CMC (a) and rest for 7 days (b)

was studied.

The supercooling curves of composite $MgCl_2$ solution with xanthan (a) or CMC is shown in Figure 5.12. With 0.5 wt% of xanthan, the supercooling of composite $MgCl_2$ gel decreases so that it does not crystallise during cooling. The supercooling of this composite material can be suppressed either by decreasing thickening agent amount or adding nucleating agent. However, the cooling process was hindered because of the lack of nucleus. On the contrary, the composite $MgCl_2$ gel with 0.5% CMC crystallised at −39.06 °C. The supercooling degree increased with increasing CMC weight percentage. When using 1.5% CMC as thickening agent in the system, the nucleus generation was affected negatively. Hence 1% of CMC do not only stabilises the gel system but also ensures the effective cooling of the composite system at the temperature of −45 °C.

5.4 Corrosion

Corrosion rate is temperature dependent. The corrosion of PCMs issue is worth addressing is because that salts are corrosive in high temperature applications. Their corrosion rate usually reach hundreds mg/cm^2 yr. However few research is performed at ambient for low temperature applications. This corrosion test was conducted with the weight loss method at ambient

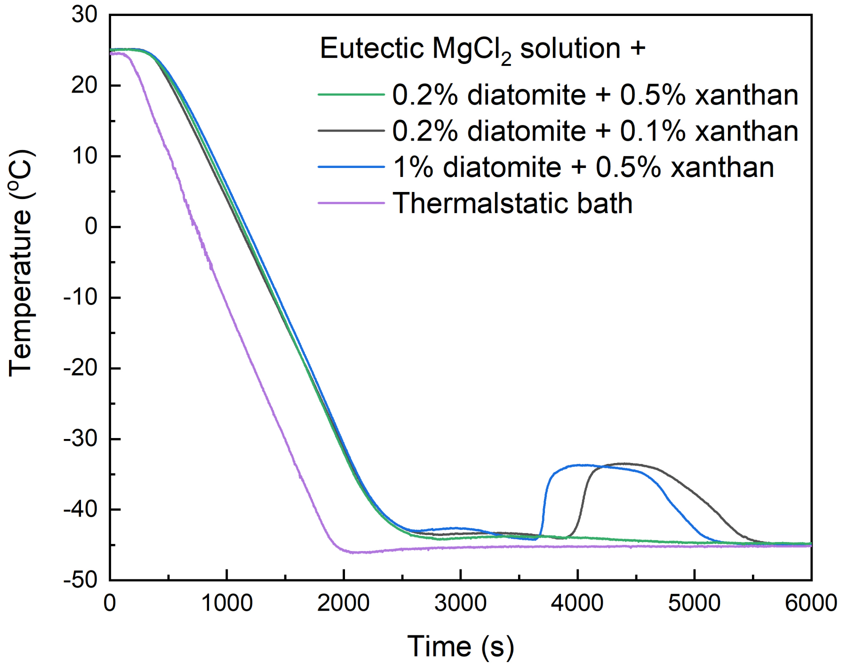

(a)

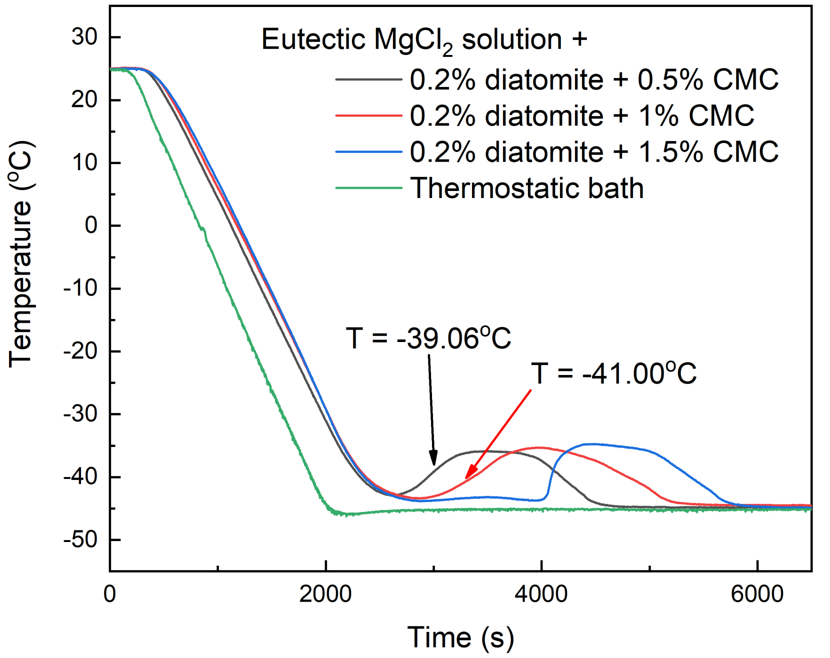

(b)

Figure 5.12: The supercooling curves of composite $MgCl_2$ solution with xanthan (a) or CMC (b)

temperature. Metals were weighted before and after immersing in eutectic NaCl-NH_4Cl solution or $MgCl_2$ solution for 7, 28, 84 days, respectively.

Figure 5.13(a) and Figure 5.14(a) presented the metal plates and the immersed PCM solution after 84 days. Their corrosion rate (CR) have been calculated and illustrated in Figure 5.13(b) and Figure 5.14(b), respectively.

As depicted in Figure 5.13, four metal plates presented various corrosion conditions in NaCl-NH_4Cl solution. After 84 days, coloured sediment was shown in each studied bottle and its intensity increased with time. Brown rust appears in stainless steels and copper K65 groups, light grey in Aluminium group. Surface tarnishing was also observed. For aluminium group specifically, bubbles generated from the metal surface was observed. The CR curve shows that the first week has the fastest corrosion rate at 20.13 mg/cm^2 yr. Then the corrosion rate decreases and is levelling off within 84 days. Aluminium and copper samples are more vulnerable to the corrosion compared to stainless steel given the same solution as they are more active with NaCl-NH_4Cl solution. Aluminium has a significant weight loss in the first week, followed by copper K65. With the passage of the time, the corrosion rate of aluminium become slower than that of copper K65. It can be due to the tenacious passive oxide layer generated on the metal surface which protects aluminium from further oxidation. Stainless steel 316 and 304 have similar performance and

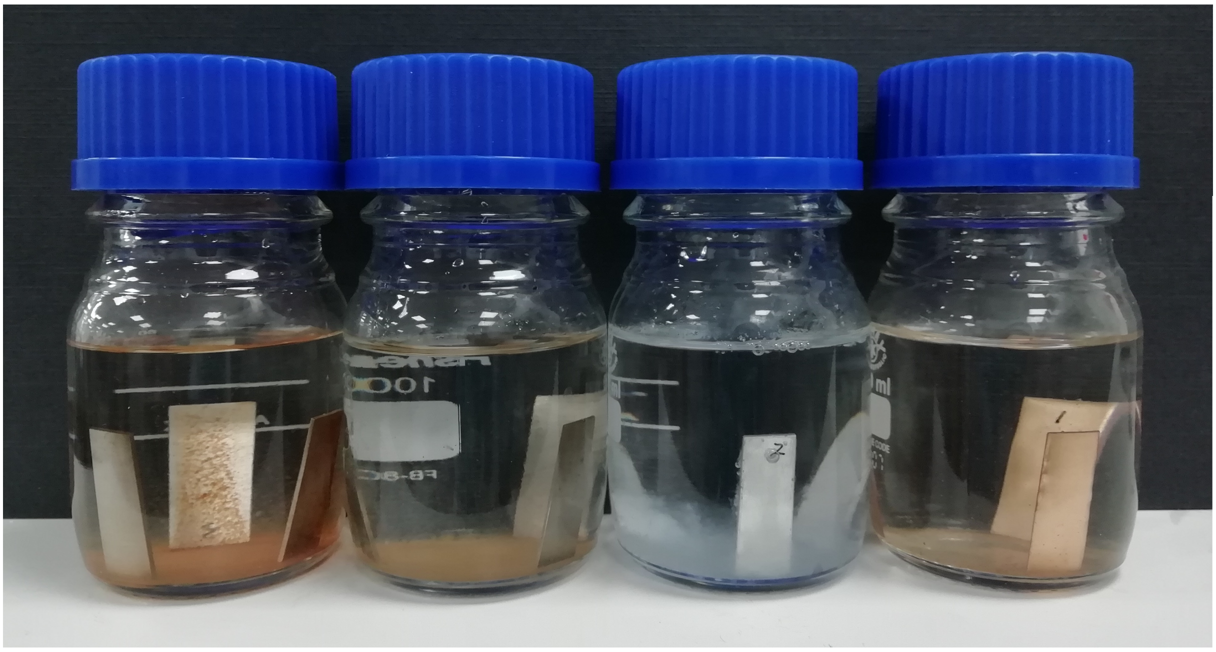

(a)

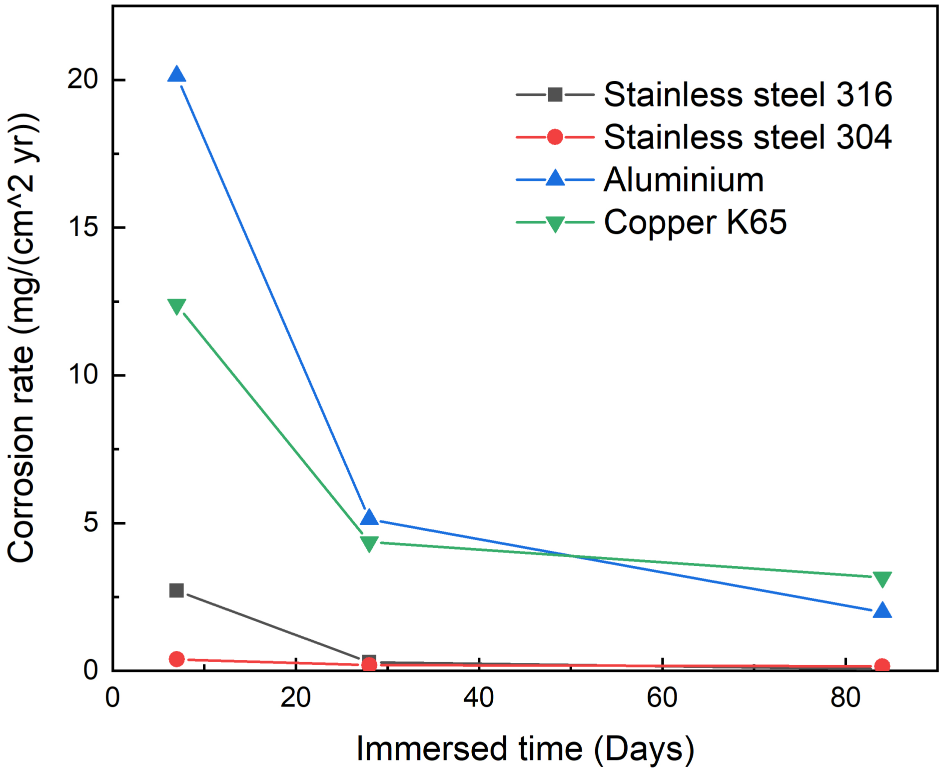

(b)

Figure 5.13: The corrosion experiment of four metals in eutectic NaCl-NH_4Cl solution (a) and their corrosion rate (b)

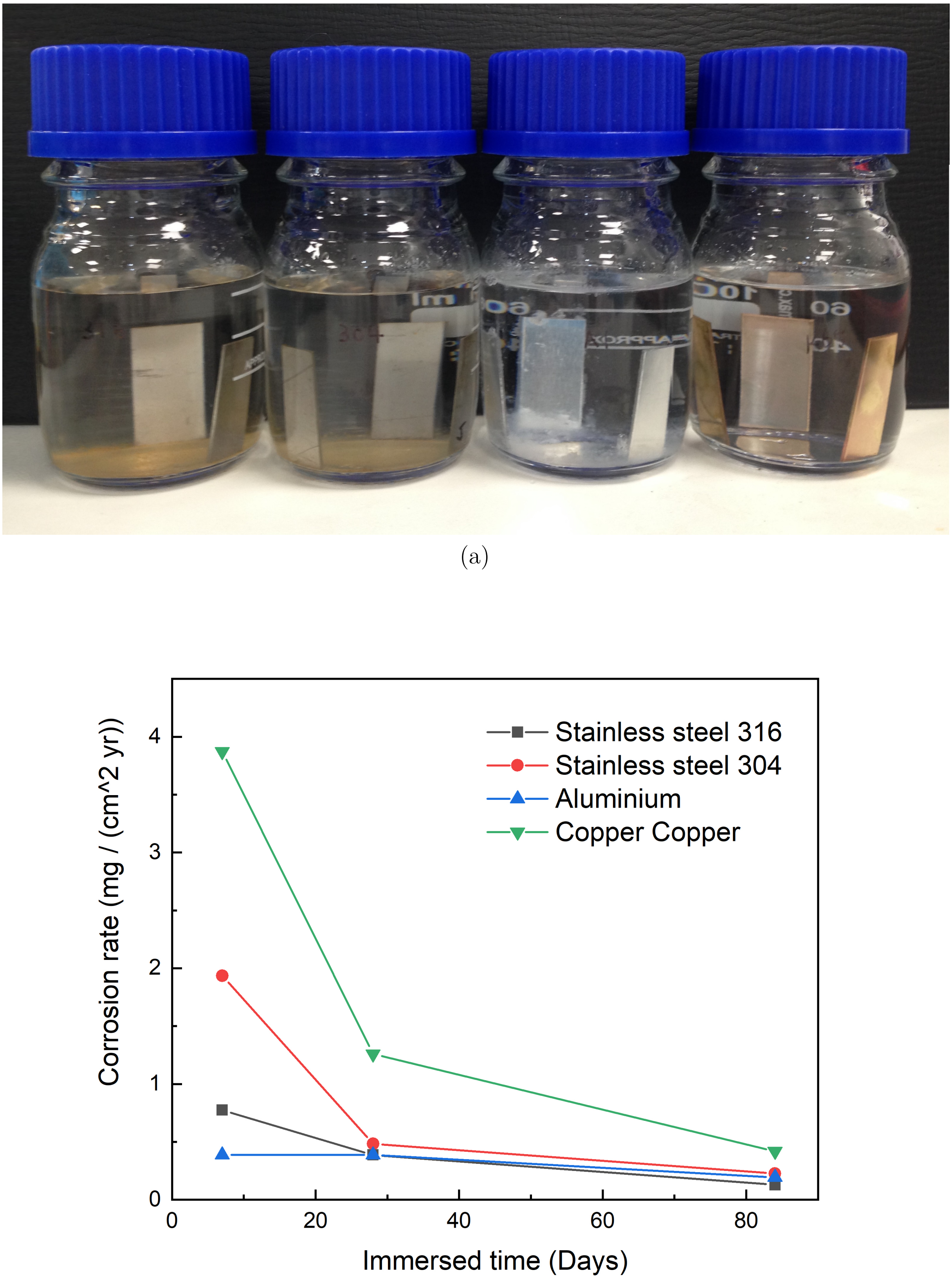

(a)

(b)

Figure 5.14: The corrosion experiment of four metals in eutectic $MgCl_2$ solution (a) and their corrosion rate (b)

are more stable when immersed in NaCl-NH_4Cl salt solution. Their CR is less that 3 mg/cm^2 yr.

A similar profile was obtained in the corrosion experiment with $MgCl_2$ solution. Metal presents good corrosion resistance in $MgCl_2$ solution overall. The solution contains less metal oxidation particles compared with NaCl-NH_4Cl solution. Copper K65 has the fastest CR of 3.87 mg/cm^2 yr. Others show negligible CR within 84 days.

The evaluation standard in the industry prospective is shown in Table 2.7. According to this guide, a recommendation table developed for NaCl-NH_4Cl solution and $MgCl_2$ solution is shown in Table 5.3.

Table 5.3: The recommendation guidance for stainless steel 316, 304, aluminium, copper K65 in NaCl-NH_4Cl solution and and $MgCl_2$ solution

Metal	In NaCl-NH_4Cl solution	In $MgCl_2$ solution
Stainless steel 316	long term service	long term service
Stainless steel 304	long term service	long term service
Aluminium	caution use	long term service
Copper K65	caution use	long term service

5.5 Summary

In this chapter, The thermoproperties of the salt-based PCMs were characterised and enhanced. Their thermoproperties were shown in the Table 5.4.

· Owning to the charging/ discharging rate of PCM suppressed by low thermal

Table 5.4: The thermal properties of the studied PCM systems

	$NaCl/NH_4Cl/H_2O$		$MgCl_2/H_2O$	
	Before	After	Before	After
Phase change temperature (°C)	-25.1	-25.67	-33.22	-33.32
Latent heat (kJ/kg)	226.42	207.18	201.03	199.89
Specific heat (kJ/(kg K))	3.25	2.92	2.96	2.74
Thermal conductivity (W/(m K))	0.507	0.62	0.53	0.66
Supercooling (K)	3.24	-	15.3	7.2

conductivity, graphite powder was introduced to increase the thermal conductivity of both NaCl-NH_4Cl solution and $MgCl_2$ solution. Their thermal conductivity were increased 22% and 24.5% individually. The supercooling of NaCl-NH_4Cl solution is 3.24 °C and no further optimisation is required. Whilst $MgCl_2$ solution have a large supercooling degree, which can be reduced to 7.24 °C with 0.2% diatomite addition at a charging temperature of −45 °C.

- Thickening/gelling agents were added to suspend foreign solid particles and stabilise the PCM system. CMC, polyacrylamide and xanthan show good thickening performance in NaCl-NH_4Cl solution. Polyacrylamide has a poor suspended ability towards diatomite powder and xanthan greatly hinders the supercooling of $MgCl_2$ solution. Hence 1% CMC was used in composite $MgCl_2$ solution system.

- In addition, corrosion experiment was conducted for both salt-water solution. A recommendation guidance was made for solution with stainless steel 316, stainless steel 304, aluminium and copper K65 plates at ambient temperature, respectively.

CHAPTER 6

RESULTS AND DISCUSSION: THEORETICALLY ANALYSIS & MATHEMATICAL MODELLING

This chapter analysis the theoretical basis of the energy consumption and dissipation conditions. Section 6.1 calculates the cold load within vehicle containers of both 12 ton and 3.5 ton vehicle scenarios. Due to the cold loss by air infiltration though unload, an air curtain was introducing to the vehicle system and its performance was investigated in Section 6.2. This section has been published in the paper.

6.1 Cooling Load Calculation

The cooling load of the vehicle was calculated based on practical transportation circumstances at $-25\,°\mathrm{C}$ and $-33\,°\mathrm{C}$. Equations are shown in Section 3.3.1. The specifications of the studied vehicle at each temperature are down below:

Table 6.1: The specifications of the multi-compartment 12 ton vehicle and conventional 3.5 ton vehicle

Compartment	12 ton		3.5 ton
	Chiller	freezer	
Inner length (m)	4	3.38	3.6
Inner width (m)	2	2	2.04
Inner height (m)	2	2	1.7
Operating temperature (°C)	5	-25	-33

6.1.1 Transmission Load

Based on *ASHRAE Handbook-Refrigeration* (ASHRAE, 2014b), the minimum effective insulation thickness of expanded polyurethane board (k = 0.023 - 0.026 W/(m K)) regarding temperature range of $-26\,°\mathrm{C}$ to $-18\,°\mathrm{C}$ is 100 mm. Considering the ageing effects on the insulation, the U can be increased by 25% for 3-year or older vehicles. The effect of solar radiation is considered based on Table 3.3. No matter what direction the vehicle is facing, the wall nearest to the vehicle tractor and the floor of the container will not affected by radiation. The condition of other walls is explained in Table 3.3.

While h_i and h_o have little impact, λ was found a dominate factor on the U value, which indicates that the transmission load is mainly determined by the quality of the insulation material. As shown in Figure 6.1, when the thermal conductivity λ of the polyurethane board change from 0.023 to 0.026 W/(m K), the U-value increased from 0.19 to 0.22 (W/(m^2 K)). With the effect of ageing process, the U-value is increased to 0.24 - 0.27 (W/(m^2 K)).

In order to identify each wall in the study, the vehicle is assumed facing north. For a U-value equal to 0.27 (W/(m^2 K)), the transmission load can be calculated by adding the heat gain through the walls, roof and floor together plus solar effects. The value for 12 ton and 3.5 ton vehicles are shown in Table 6.2 and Table 6.3, respectively.

Table 6.2: The cold load through transmission of 12 ton vehicle with U-value = 0.27 (W/(m^2 K)) (ASHRAE, 2014a)

	A [m^2]		Δ T [K]		Q [W]	
	chilled	frozen	chilled	frozen	chilled	frozen
East/west wall	9.24	7.88	30 + 4	60 + 4	84.67	135.86
South wall	4.84	4.84	30 + 3	60 + 3	43.05	82.18
Roof	9.24	7.88	30 + 9	60 + 9	97.13	146.47
Floor	9.24	7.88	30	60	74.71	127.37
North wall	4.84	4.84	30	60	39.13	78.27
Total	-	-	-	-	423.37	706

The frozen compartment has a significantly larger transmission gain compared with the chilled compartment. It is attributed to the larger outside surface area of the frozen compartment and the larger temperature difference.

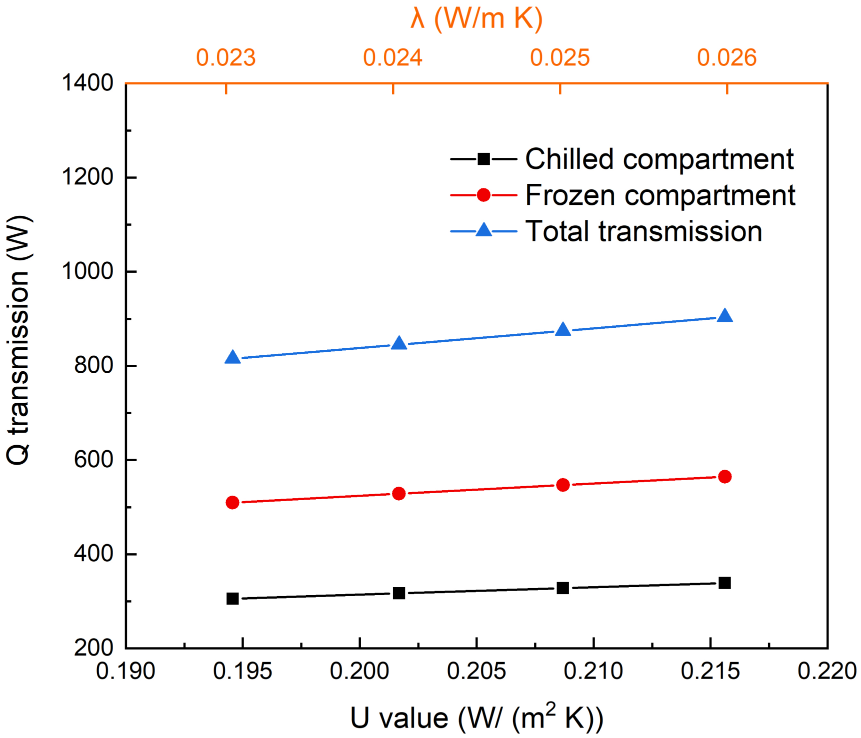

(a)

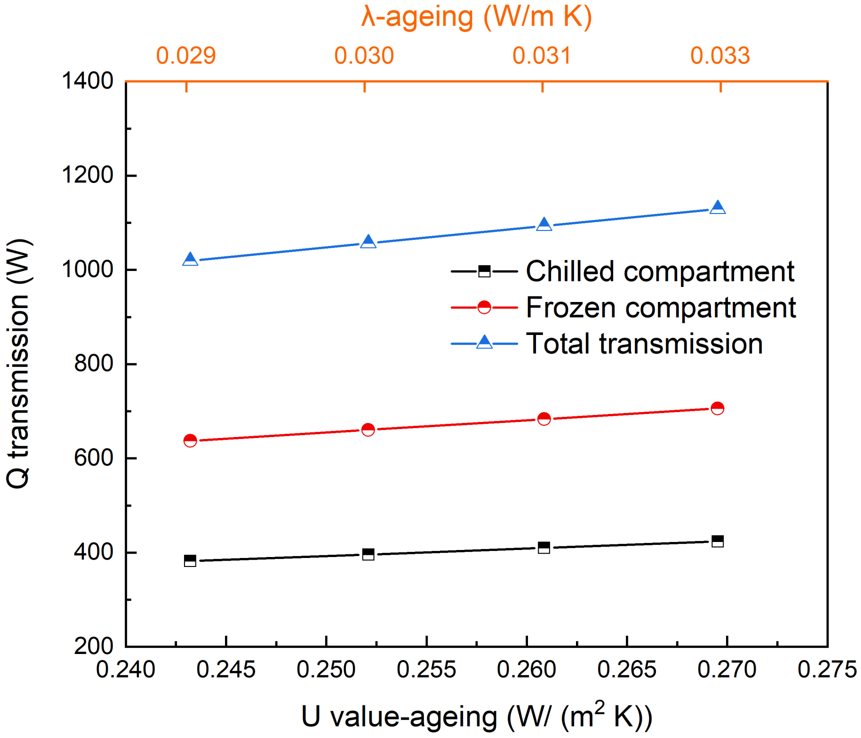

(b)

Figure 6.1: The U value and transmission load with different thermal conductivity value of the insulating material (a) original (b) after 3 years or more ageing

Table 6.3: The cold load through transmission of 3.5 ton vehicle with U-value = 0.27 (W/(m^2 K)) (ASHRAE, 2014a)

	A [m^2]	Δ T [K]	Q [W]
East/west wall	7.22	68 + 4	145.95
South wall	4.26	68 + 3	84.88
Roof	8.51	68 + 9	183.53
Floor	8.51	68	162.89
North wall	4.26	68	81.44
Total	-	-	804.64

The transmission through the roof has the largest value of the whole vehicle. It captured the direct solar radiation and has a considerable heat gain compared to the floor. In this case, a practical way to reduce the transmission load is to increase the thickness of the insulation layer, especially in the roof area, or employ a better insulating material with higher thermal resistance.

6.1.2 Infiltration Load

The infiltration load of each compartment of the vehicle is calculated, respectively. The extreme outdoor condition is 35°C in temperature and 50% in RH (ASHRAE, 2014a). The internal temperature will be maintained at -25°C during phase change process. The RH within container, which affects the properties of the inner air, remains unknown. The air property with different RH conditions can be checked in psychrometric chart. Another uncertainty in the calculation is ACH value. Generally, ACH varies based on sealing properties from well to poor. For a well insulated container, a empirical ACH = 0.2 and the ACH value for a truck tractor is about 0.7 (Chaney, Sailor, et al., 2008). Hence the ACH value for a refrigerated container fall in between.

For instance, in Equation 3.11, all the potential scenario with different ACH factors and the relative humidity in refrigerated space were laid out in Figure 6.2.

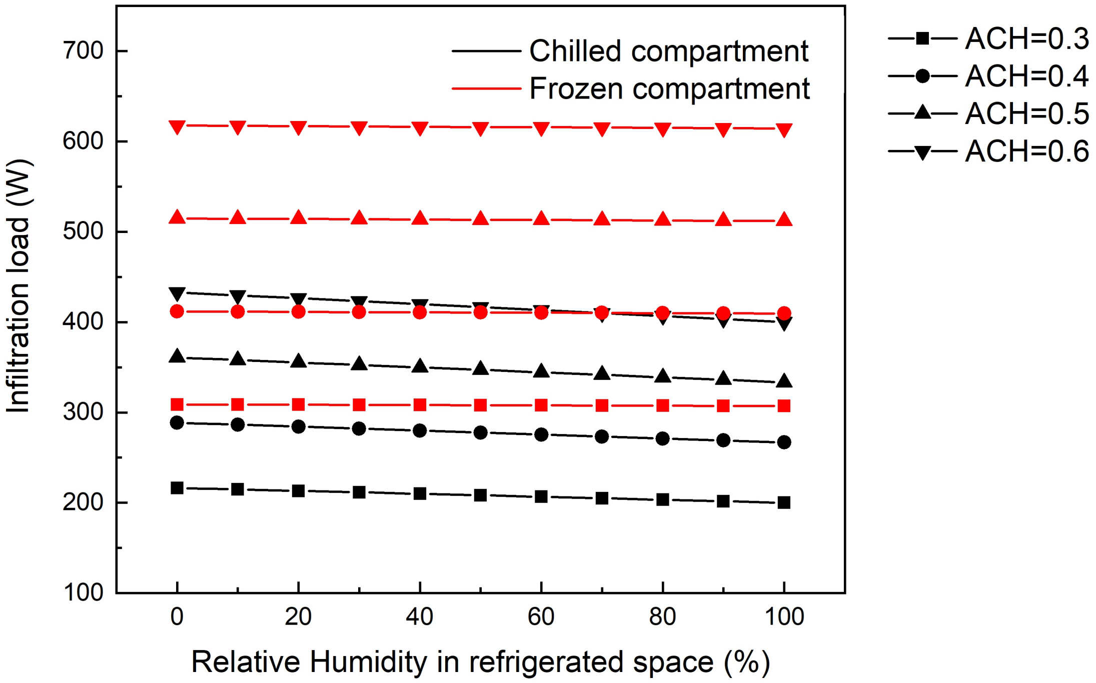

Figure 6.2: The calculation value of the infiltration load with the change of in-vehicle humidity and ACH by Equation 3.11

Overall, the infiltration load of the frozen compartment is larger than the chilled compartment. In the refrigerated space, ACH value has a greater impact on the infiltration load than RH. With every 0.1 increase in the ACH value, the infiltration load rises ∼0.25%, whilst with the increasing of the RH, the infiltration load slightly decreased.

As introduced in Section 3.3.1. The air loss by product loading/unloading is one of the main contribution of the vehicle infiltration load. Two operating conditions are discussed in this study: the door opening and door closing.

Door opening The door opening condition is set according to the given application: each door opening takes 25 seconds and there are 36 door openings in a 9 h trip, that is, the door will be opened once in every 15 minutes. Each door opening last for 1 minute.

Four equations in Section 3.3.1.2 evaluate the infiltration load from different perspective. The calculation results for the worst-case scenario of four equations are compared and listed in Table 6.4.

Table 6.4: The air infiltration load calculated in each compartment by different equations

	12 ton			3 ton
	Chilled compartment (W)	Frozen compartment (W)	Total infiltration load (W)	Infiltration load (W)
Equation 3.5	187.25	585.94	773.19	550.99
Equation 3.9	393.25	671.94	1065.2	748.7
Equation 3.11	397.28	493.47	890.75	496.35
Equation 3.12	265.89	350.88	616.77	369.51

Top three equations provided similar calculation result. Among them, Equation 3.5 and Equation 3.11 is based on the absence of any winds. Equation 3.9 is identical to that of open doorways exposed to wind or with a frequently open doorways. Hence the infiltration load result is higher than other two.

Liu (2010) calculated the infiltration load of a 3.5 ton vehicle by Equation 3.5. Owing to an arithmetical error on doorway open-time factor D_t, the result is not accurate. Eby. S. W (1955) discussed the extra infiltration load through cracks in the front of a moving vehicle under a the ambient condition same with this study. The extra infiltration load is approximately 1115 W at the vehicle temperature of $-18\,^{\circ}\mathrm{C}$ (ASHRAE, 2014a). Therefore, the top three equations are useful guides in infiltration load estimation. The maximum infiltration load of the multi-compartment vehicle is 1.07 kW. The total cold load of the 12 ton vehicle is ~2.19 kW.

Similar conclusion can be drawn for 3.5 ton multi-compartment vehicle. Top three equations provide similar infiltration load value. Result of Equation 3.9 is larger since it includes the heat gain by negative pressure caused by vehicle movement. Therefore this value is proportional to the vehicle speed. The total cold load of the 3.5 ton vehicle is ~1.55 kW.

Normally, 10% of safety factor is introduced for possible discrepancies. Therefore, if the new PCMs formulated in this study are applied for passive cooling accordingly, in an 8 h transportation, the weight requirement of eutectic NaCl-NH_4Cl solution and $MgCl_2$ solution is 308.26 kg and 240.17 kg, respectively.

Door closing The door opening effect was considered by doorway open-time factor in the first two equations. Under the door closing condition, the calculation results by Equation 3.5 and Equation 3.9 is listed in Table 6.5.

Table 6.5: The air infiltration load calculated in each compartment by different equations with the door closed

	12 ton			3 ton
	Chilled compartment (W)	Frozen compartment (W)	Total infiltration load (W)	Infiltration load (W)
Equation 3.5	11.70	36.62	48.32	34.44
Equation 3.9	24.58	41.99	66.57	46.79

As it can be seen in Table 6.5, the air infiltration load under door closing condition is dramatically decreased compared with Table 6.4. It is evident that the door open-close time have significant effect on the value of infiltration load. In order to minimise the infiltration loss, a smaller door area and less frequent door opening time are required. On top of that, decreasing the duration of the doorway passages can also reduce the infiltration load.

However, the door opening condition mainly depends on the goods delivery requirement. A more practical way to decrease the infiltration loss is through installing air curtain at doorway of the refrigerated vehicle. Therefore, numerical study have been done to investigate the performance of the air curtain on a refrigerated vehicle. There are researches regarding the performance of the air curtain at chilling temperature. In order to compare the result, the inner temperature of the vehicle is set at 5 °C. The next section explains the modelling methods and results.

6.2 Numerical study (Cong et al., 2019)

6.2.1 Model validation

The model setup is presented in Section 3.3.2.2. In order to validate the reliability of the established numerical model, the numerical simulation was carried out for an open cavity with the same geometrical configurations and thermal boundary conditions as shown in the work of Juárez et al. (2011). The top and bottom horizontal walls of the open cavity were adiabatic, while its left vertical wall was kept at a constant temperature T_h. The right side of the cavity was open to the surroundings. The surrounding fluid interacting with the cavity was at a constant temperature T_l, which was lower than T_h. The temperature difference induces natural convection of the surrounding fluid, which is similar to the situation of the refrigerated container when the door is opened in the present study. The comparison of results obtained by the present model with those reported by Juárez et al. (2011) is presented in Figure 6.3(a).

The results are the dimensional temperature profiles along the dimensional coordinate X at the dimensional coordinate Y = 1.5 for dimensionless temperature difference $\alpha = 0.3$ and 1.3 when the Rayleigh number is 104. It can be seen from Figure 6.3(a) that the results obtained by the present model agree well with those reported by Juárez et al. (2011) for both two different dimensionless temperature differences. Therefore, the established model proves to be valid. In order to demonstrate the accuracy of 2D simulations, a 3D simulation was carried out to study the case with a jet velocity of 2 m/s and a nozzle width of 10 cm. The comparison of the average air temperature inside the container between 2D and 3D simulations is shown in Figure 6.3(b). It can be found that the average temperature obtained in the 3D simulation is slightly lower than that obtained in the 2D simulation. It is attributed to the effect of the side wall of the container, which reduces the velocity of hot air flowing into the container. Even so, they have the same evolution tendency and the small temperature deviation ($< 0.5\,^{\circ}\mathrm{C}$) between 2D and 3D simulations is acceptable. It implies that the 2D simulations adopted in this paper can accurately capture the flow and heat transfer characteristics

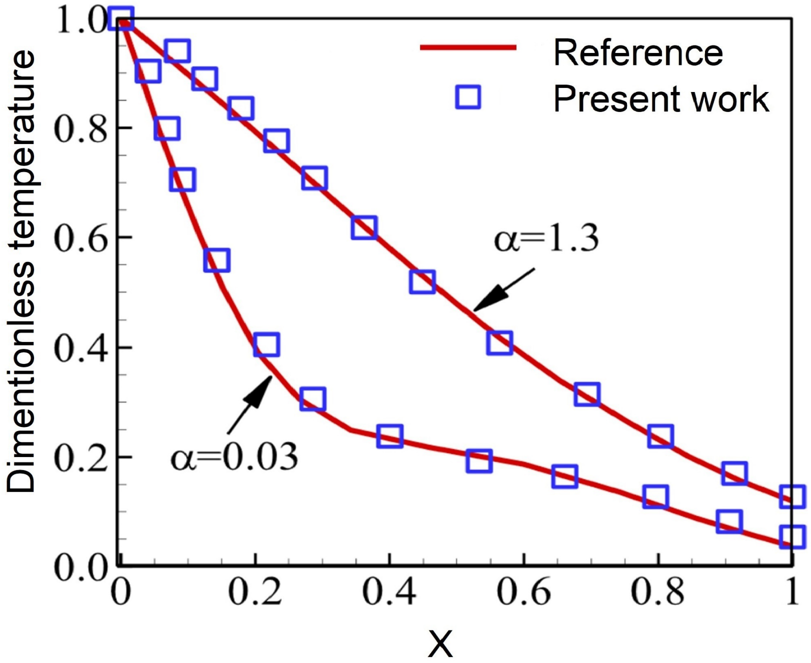

(a)

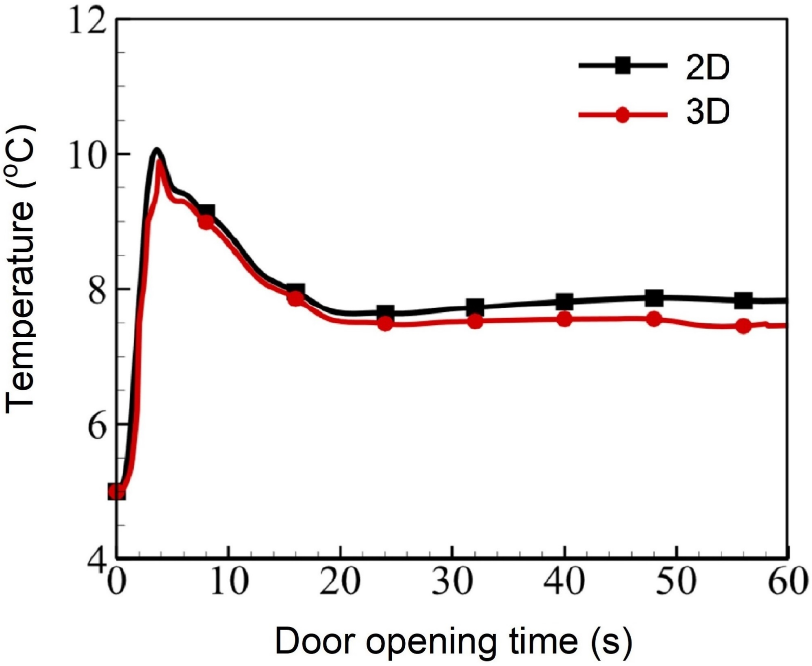

(b)

Figure 6.3: Validation of the present numerical model with results reported by Juárez et al. (2011) (a) and comparison of the average air temperature in the container between 2D and 3D simulations (b)

in and near the container with an air curtain.

6.2.2 Simulation results

Based on the validated numerical model in Section 3.3.2.2, the effects of jet velocity, nozzle width, and jet angle of the air curtain on the evolution of the velocity and temperature inside the container and near the doorway were explored and elaborated, respectively.

6.2.2.1 Effects of Jet Velocity

Figure 6.4 illustrates the evolution temperature distribution and airflow pattern inside and near the container with different jet velocities (0 m/s, 1 m/s, 2 m/s, and 4 m/s) of the air curtain within 1 min after the door is opened. In all the four scenarios, the air nozzle has a width of 10 cm and the air jet angle is 0 (i.e., vertical jet). When the refrigerated container door is opened without an air curtain, hot air outside will fill into the refrigerated space immediately and the inner cold air will flow outward due to the temperature difference.

As is illustrated in Figure 6.4(a), the situation is well reproduced. After opening the door, massive hot air outside is invading inward through the ceiling of the container while the cold air inside is flowing outward through

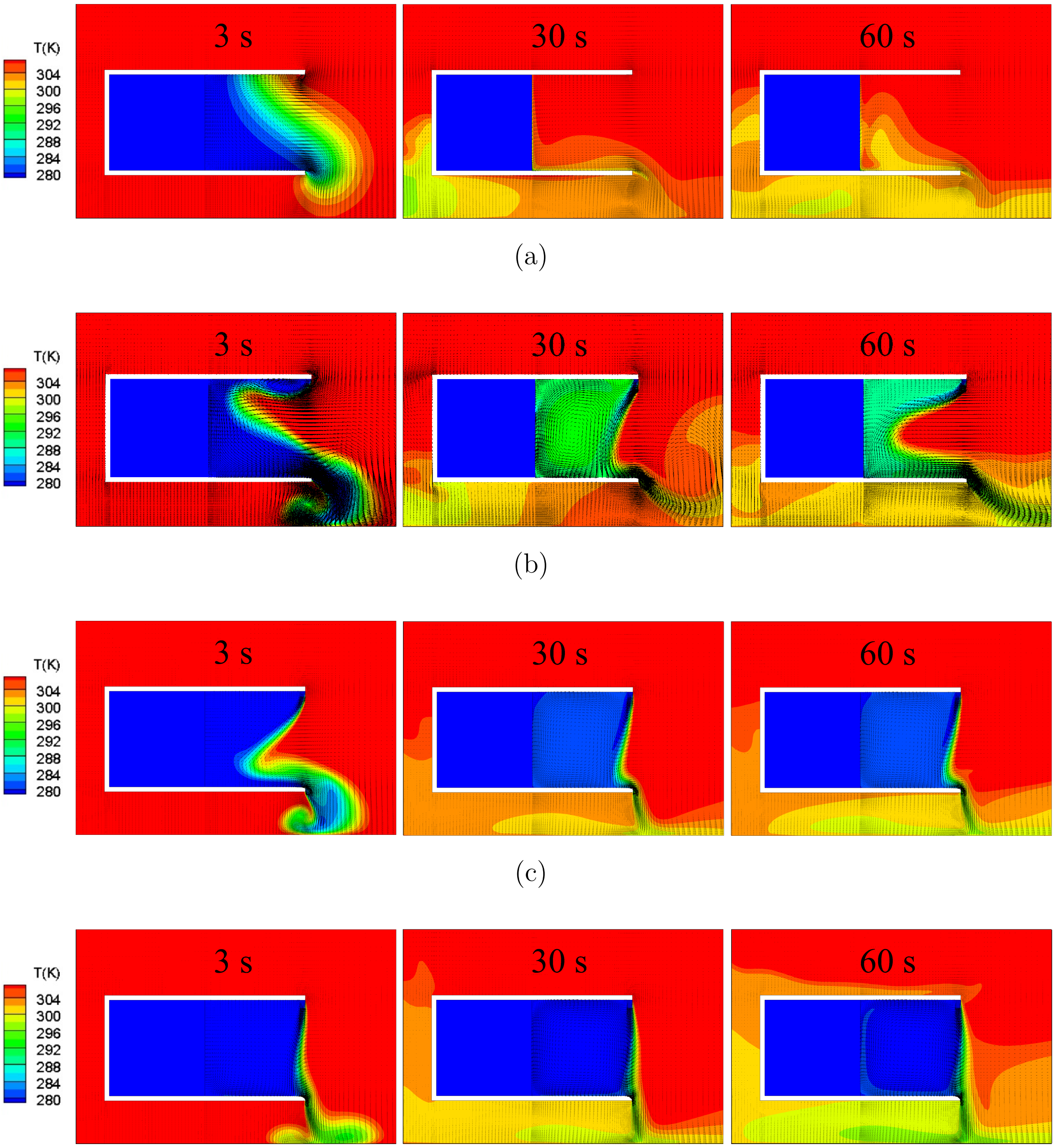

(a)

(b)

(c)

(d)

Figure 6.4: The temperature and velocity distribution at 3 s, 30 s, and 60 s after the door is opened when the air jet velocity of air curtain is (a) 0 m/s, (b) 1 m/s, (c) 2 m/s, and (d) 4 m/s

the bottom of the open doorway. The hot air almost occupies the whole refrigerated space within 30 s when the air curtain does not exist. The hot air continues infiltrating afterwards and absorbing cold of the products directly.

With the help of the air curtain, the hot air infiltrated into the container decreases in various degrees with different air jet velocities as illustrated in Figure 6.4(b) - Figure 6.4(d). Generally, a larger airflow rate exhibits better insulation capability against the hot air infiltration. For the jet velocity of 1 m/s, the air curtain is unstable and cannot effectively prevent the infiltration of outer hot air. From 3 s to 30 s, the air curtain moves outwards and tends to be stabilised. It becomes concave inward again at 60 s. In terms of the temperature difference between inside and outside of the container, the jet velocity of 1 m/s cannot provide a stable barrier between the inner cold air and the outer hot air. The temperature rise is lower than that without an air curtain, though the inner air temperature increases significantly at 60 s. When the jet velocity increases to 2 m/s, the air curtain touches the bottom of the container at 30 s and maintains the shape and position stably afterwards. Therefore, the infiltration of outer hot air is effectively blocked and the inner air temperature rise is effectively suppressed. When the jet velocity is further increased to 4 m/s, the improvement in the obstruction ability to the infiltration of outer hot air and suppression of temperature rise is very limited.

The temperature evolution of the monitored points and surface are illustrated in Figure 6.5. Various air jet velocities lead to significant differences in the temperature evolution.

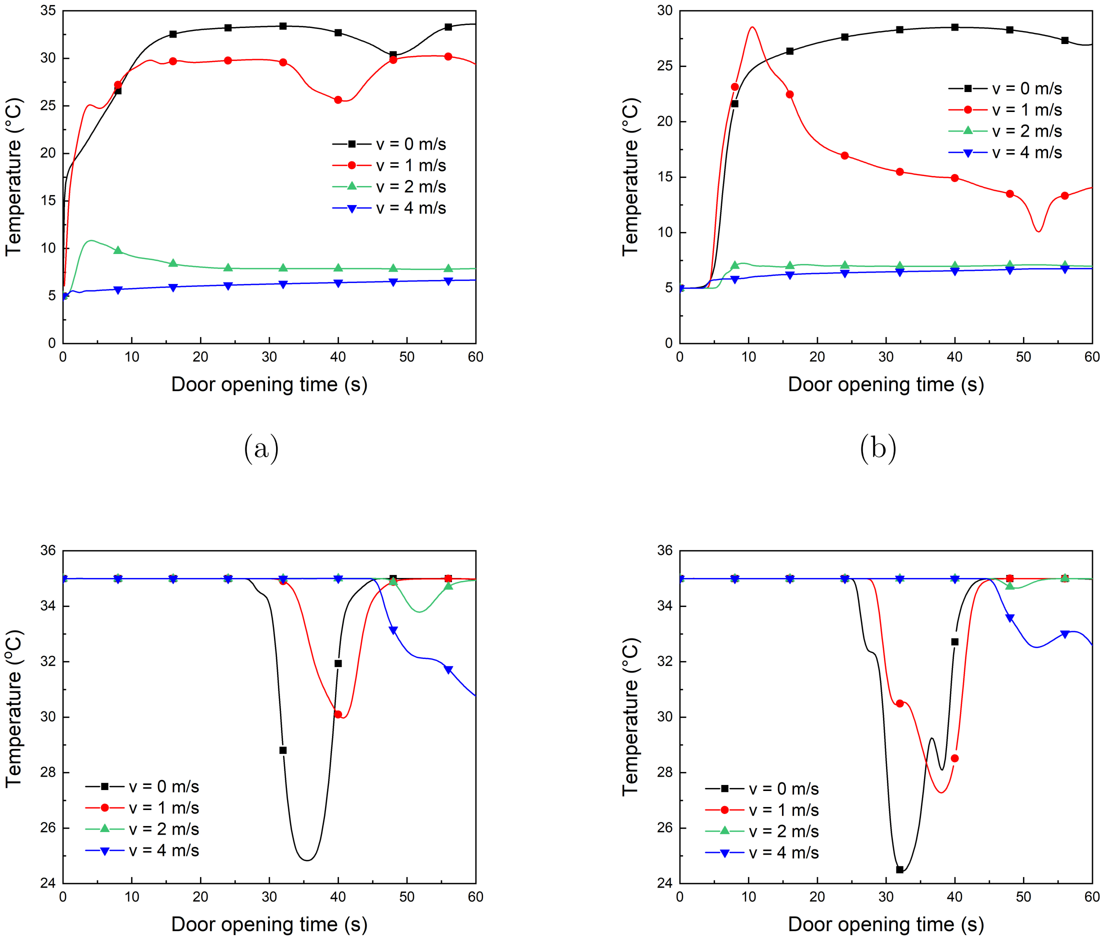

(a)

(b)

(c)

(d)

Figure 6.5: The temperature evolution within 1 min after the door is opened with different air jet velocities (v): (a) the average air temperature inside the container, (b) the temperature of the monitoring point at the air–goods interface, (c) and (d) the temperatures outside the container at Point 2 and Point 3, respectively

As is shown in Figure 6.5(a), without an air curtain (v=0 m/s), the average temperature of the inner air increases to about 33 °C within 20 s after the door is opened and is maintained at this level with small fluctuations; in the case with the jet velocity of 1 m/s, the average temperature also sharply increases to about 29 °C within 20 s and is also maintained at this level with small fluctuations; when the jet velocity reaches 2 m/s, the average temperature smoothly increases from initial temperature to ∼12 °C and then decreases to ∼7.9 °C. When the jet velocity further increases to 4 m/s, the average temperature has a minimum increment of about 6.5 °C within 60 s among the four jet velocities. Although the jet velocity doubles from 2 m/s to 4 m/s, the average temperature rise only decreases by about 1.4 °C. The temperature at the goods–air interface directly reflects the risk of quality degradation of goods. Figure 6.5(b) displays the temperature evolution of the monitoring point at the goods–air interface. For the jet velocity of 1 m/s, the temperature at the interface fluctuates acutely within 1 min and even increases to a higher value than that without air curtain within 13 s. This is due to the convection enhancement caused by the unstable air curtain. When the jet velocity is increased to 2 m/s, the temperature at the interface slightly increases and is maintained at about 6.5 °C after 20 s. Thus, the temperature rise at the interface is also reduced at $v = 2$ m/s compared to that without the air curtain. When the jet velocity is further increased to 4 m/s, the improvement on temperature preservation is limited. The temperature of the monitoring point outside the container can be used to indicate the cold loss. Figure 6.5(c) and Figure 6.5(d) present the temperature evolution at the different monitoring points outside the container (only Point 2 and Point 3 are shown). The change tendency of the temperature fluctuation amplitude with the jet velocity is the same at all three monitoring points while the evolution patterns of the temperature at all the three monitoring points are similar for each jet velocity. The lower the temperature at the monitoring point outside the container is, the larger the cold loss within the container is. The cold loss is not negligible when the jet velocity is lower than 1 m/s. When the jet velocity is increased to 2 m/s or 4 m/s, the cold energy loss is notably reduced, although the cold loss is slightly increased after 40 s. This part of the cold loss is provided by the air curtain. It can also be found that the cold loss at v = 4 m/s is larger than that at v = 2 m/s. Therefore, the most efficient jet velocity in this study should be 2 m/s. The above results demonstrate that introducing the air curtain with precisely tailored jet velocity can help reduce the infiltration of outer hot air and realise decent low-temperature preservation inside the refrigerated container after the door is opened.

Furthermore, more simulations were carried out to unveil the effect of the Reynolds number on the average air temperature within the container with 60 s door opening, which is shown in Figure 6.6. There is a sharp temperature decline with the increase of the Reynolds number when Reynolds number is less than 10,000. When the Reynolds number is greater than 14,000, the average temperature within the container nearly keeps constant with the increase of the Reynolds number. It means that the air curtain is enough to effectively maintain a low temperature within the container when the Reynolds number is 14,000, which corresponds to the jet velocity of 2 m/s in this study.

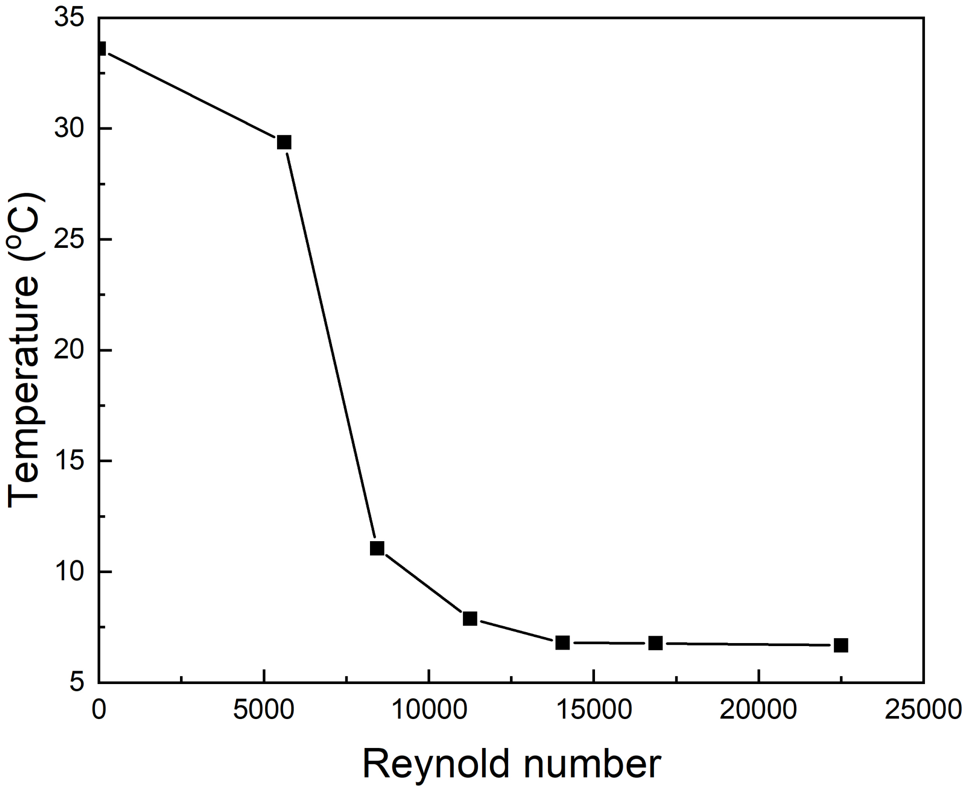

Figure 6.6: Variation of the average air temperature in the container with the Reynolds number at 60 s after opening of door

6.2.2.2 Effects of Nozzle Width

To study the influence of the nozzle width of the air curtain, the air convection and heat transfer of air curtains with nozzle widths of 1 cm, 5 cm, and 10 cm were simulated and comparatively analysed. In this section, the air jet velocity was set to 2 m/s. Figure 6.7 presents the transient air convection patterns and the temperature distribution for different nozzle widths. It is obvious that the nozzle width significantly influences the stability of the air curtain. As is shown in Figure 6.7(a), the air curtain with a nozzle width of 1 cm is too weak so that the air jet does not reach the container and the air curtain is severely concave inwards. The air curtain cannot withstand the ventilation caused by the large temperature difference between the air inside and outside the container. Within 3 s after the door is opened, a large amount of hot air invaded from the outside while the cold air continuously flows outward. After 30 s, the hot air nearly occupied the whole cold space. Within the calculating period, the air fluctuated severely in the space. The air curtain with a nozzle width of 5 cm in Figure 6.7(b) provides better temperature preservation compared to that with a nozzle width of 1 cm. A relatively stable air curtain is formed after 60 s, which prevents the infiltration of the outer hot air to some extent. However, the air curtain is still concave inwards and the air temperature inside the container still shows a noticeable rise after 60 s. When the nozzle width is further increased to 10 cm as shown in Figure 6.7(c), a more stable air curtain is formed and creates a good thermal barrier to prevent the infiltration of the outer hot air, which demonstrates the best performance of all three nozzle widths.

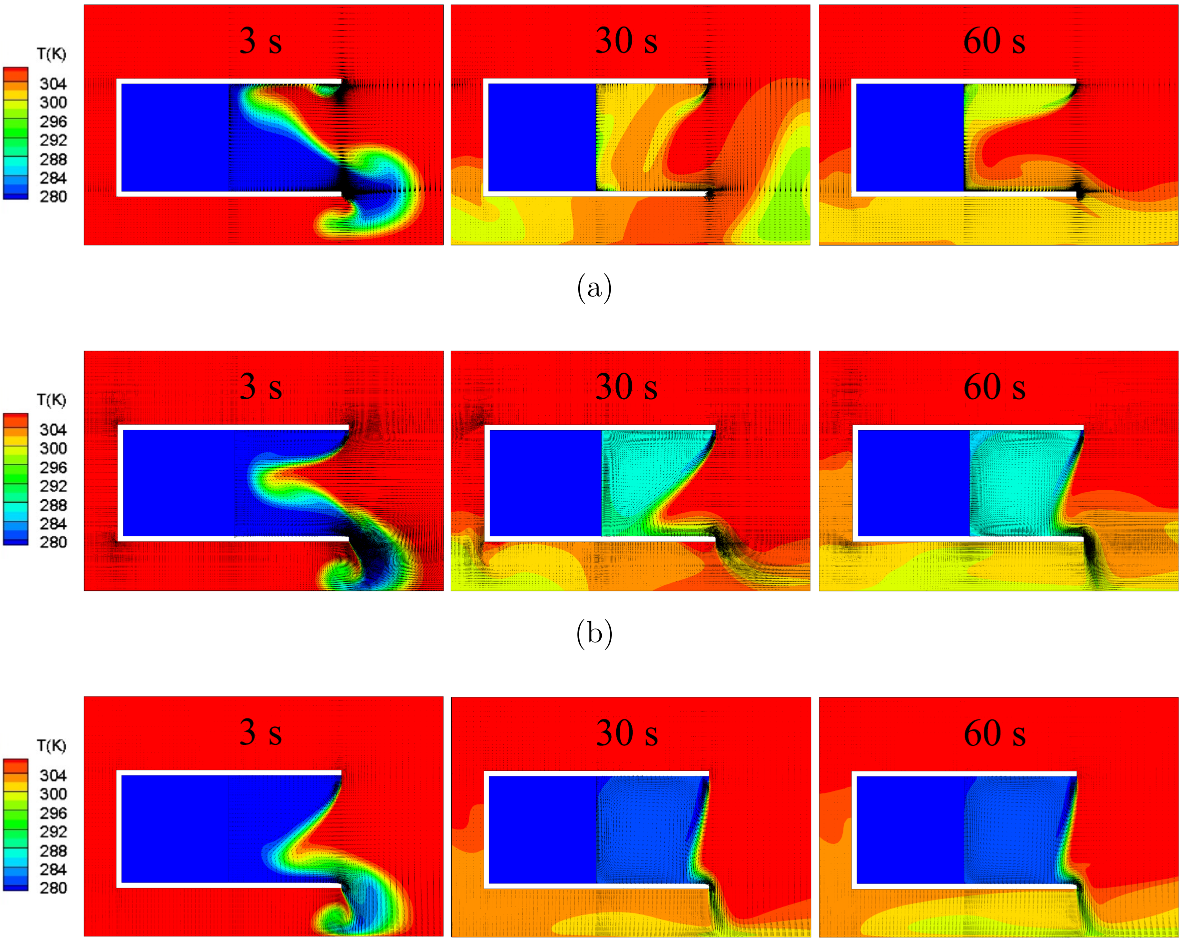

(a)

(b)

(c)

Figure 6.7: The temperature and velocity distribution (3 s, 30 s, and 60 s) when the nozzle widths of the air curtain are (a) 1 cm, (b) 5 cm, and (c) 10 cm, respectively

The profiles of the temperature evolution under different nozzle widths are summarised in Figure 6.8. The evolution of the average air temperature inside the container show a similar change trend for the three nozzle widths as shown in Figure 6.11(a).

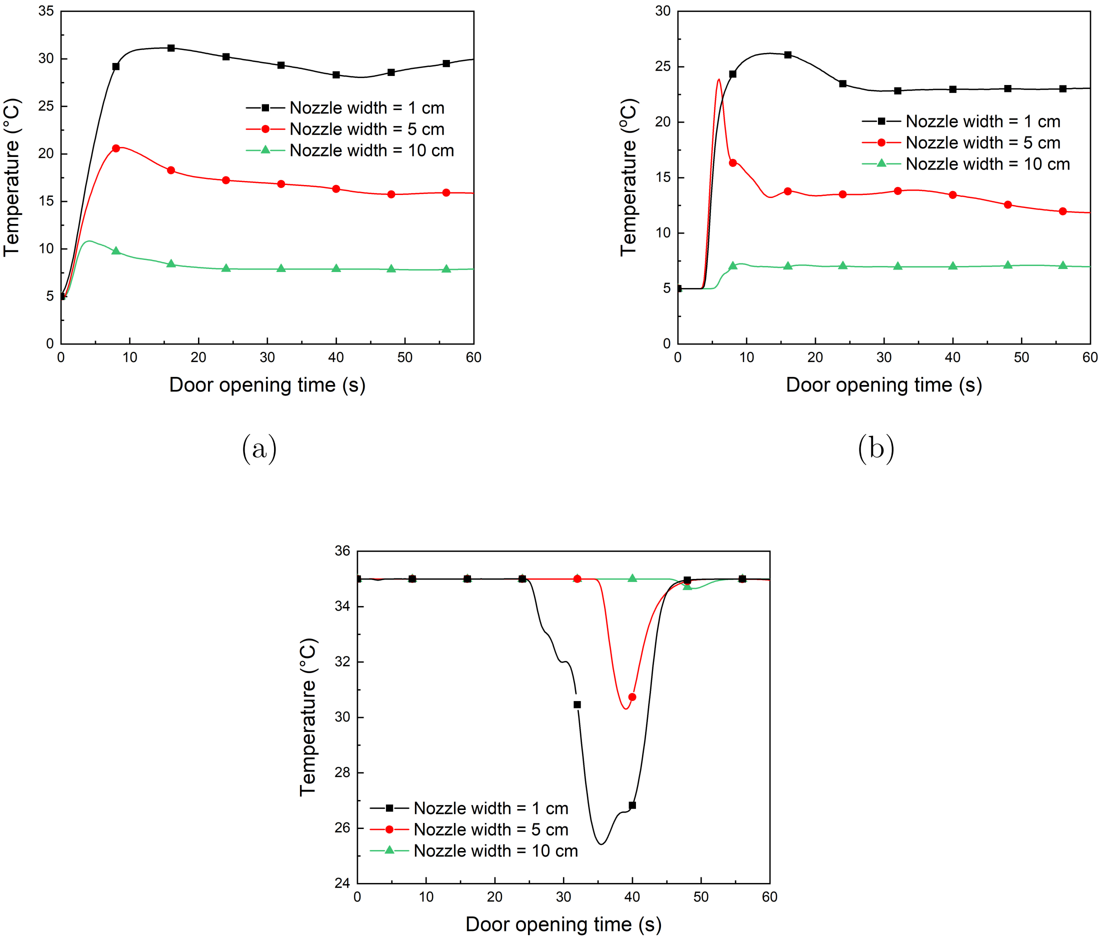

(a)

(b)

(c)

Figure 6.8: The temperature evolution within 1 min after the door is opened with different nozzle widths: (a) the average air temperature inside the container, (b) the temperature of the monitoring point at the air–goods interface, and (c) the temperature of monitoring point 3 outside the container

Generally, they first increase sharply and then decrease slowly until become stable. Both the increase rate and the end temperature decrease with the increase of the nozzle width. The average air temperature inside the container first rises to about 31.5 °C, 21.0 °C, and 11.0 °C after the door is opened for nozzle widths of 1 cm, 5 cm and 10 cm, respectively. Afterwards, they decrease to about 30 °C, 16 °C, and 7.9 °C at 60 s, respectively. The average air temperature is stabilised more quickly with the nozzle width of 10 cm than other nozzle widths. The temperature evolution of the monitoring point at the goods–air surface are shown in Figure 6.11(b). When the nozzle width of the air curtain is 1 cm, the temperature of the air contacting with the surface of the goods has increased to about 26 °C within 15 s and eventually maintained at about 23 °C. In the case with a nozzle width of 5 cm, this temperature increases sharply to about 24 °C within 8 s and eventually declines to about 12 °C at 60 s. The air curtain with a nozzle width of 10 cm keeps a stable inner air environment from the very beginning and keeps the temperature at the goods–air interface near 6.5 °C. Figure 6.11(c) shows the temperature evolution of the monitoring point 3 outside the container. It indicates that the value of the nozzle width is in negative correlation with the cold loss. Besides, a larger nozzle width delays the occurring of cold loss. For instance, the cold loss into the ambient is detected at about 25 s for the nozzle width of 1 cm, about 35 s for the nozzle width of 5 cm, and 44 s for the nozzle width of 10 cm. Furthermore, more simulations are carried out to reveal the effects of relative nozzle width on the average air temperature in the container at 60 s after door opening, as shown in Figure 6.9. When the relative nozzle width is below

0.0375, the average temperature linearly and markedly decreases. When the relative nozzle width increases from 0.0375 to 0.05, the average temperature slightly decreases. It means that the air curtain is effective enough when the relative nozzle width is set between 0.0375 and 0.05, which correspond to the nozzle width between 7.5 cm and 10 cm. The stable average air temperature inside the container is about 8 °C after the door is opened for the nozzle width of 7.5 cm.

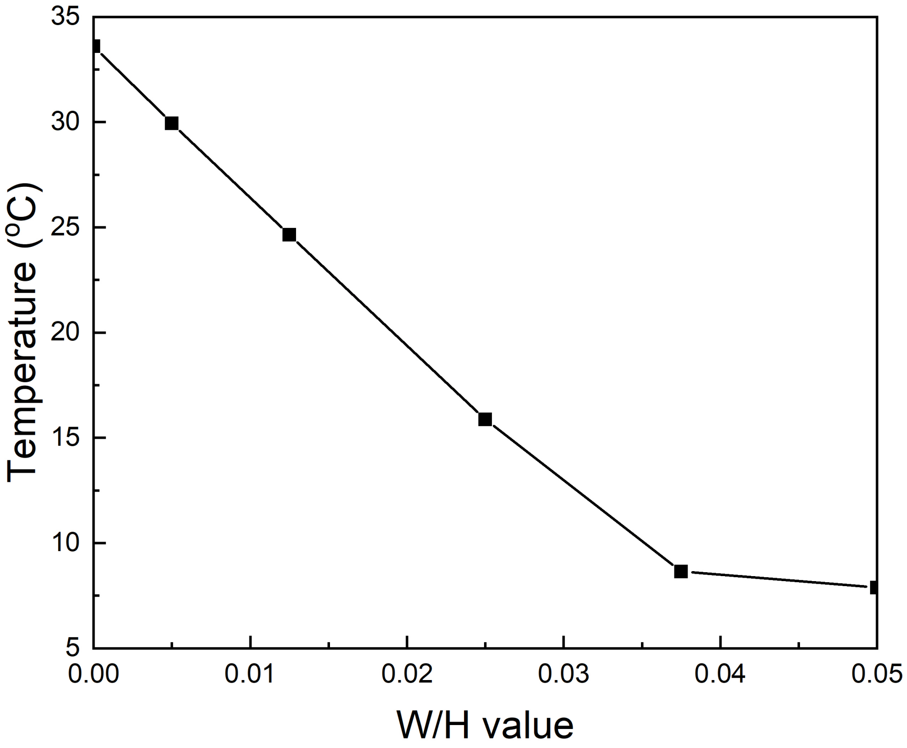

Figure 6.9: Variation of the average air temperature in the container with relative nozzle width (W/H) at 60 s after opening of door

6.2.2.3 Effects of the Jet Angle

Four different jet angles of the air curtain were studied at a jet velocity of 2 m/s with a nozzle width of 10 cm. The jet direction along the negative Y-axis is defined as 0 deg, and the jet direction towards the outside of the container is positive. The effects of the jet angle were examined among -15 deg, 0 deg, 15 deg, and 30 deg. Figure 6.10 shows the temperature distributions under different jet angles. The jet angle exhibits less effect than jet velocity and nozzle width since the temperature distributions under different jet angles are similar. When the jet angle is -15 deg as shown in Figure 6.10(a), the air curtain blows more cold energy out and allows more hot air into the container than other cases, because it partially follows the direction of natural convection. During the pure natural convection as shown in Figure 6.4(a), the buoyancy force makes the hot airflow into the container from the upper part of the doorway while the cold air flows out of the container from the lower part of the doorway. The airflow caused by the air curtain with the -15 deg jet angle has a similar direction. Also, it provides a minimum cold space after the air curtain becomes stable at 60 s. The temperature distribution shows little changes as the jet angle increases from 0 deg to 30 deg as shown in Figure 6.10(b) - Figure 6.10(d), except those near the air curtain. The air curtain is only concave inwards at a jet angle of 0 deg, while they are convex outwards near the ceiling of the container and concave inwards near the floor of the container at jet angles of 15 deg and 30 deg.

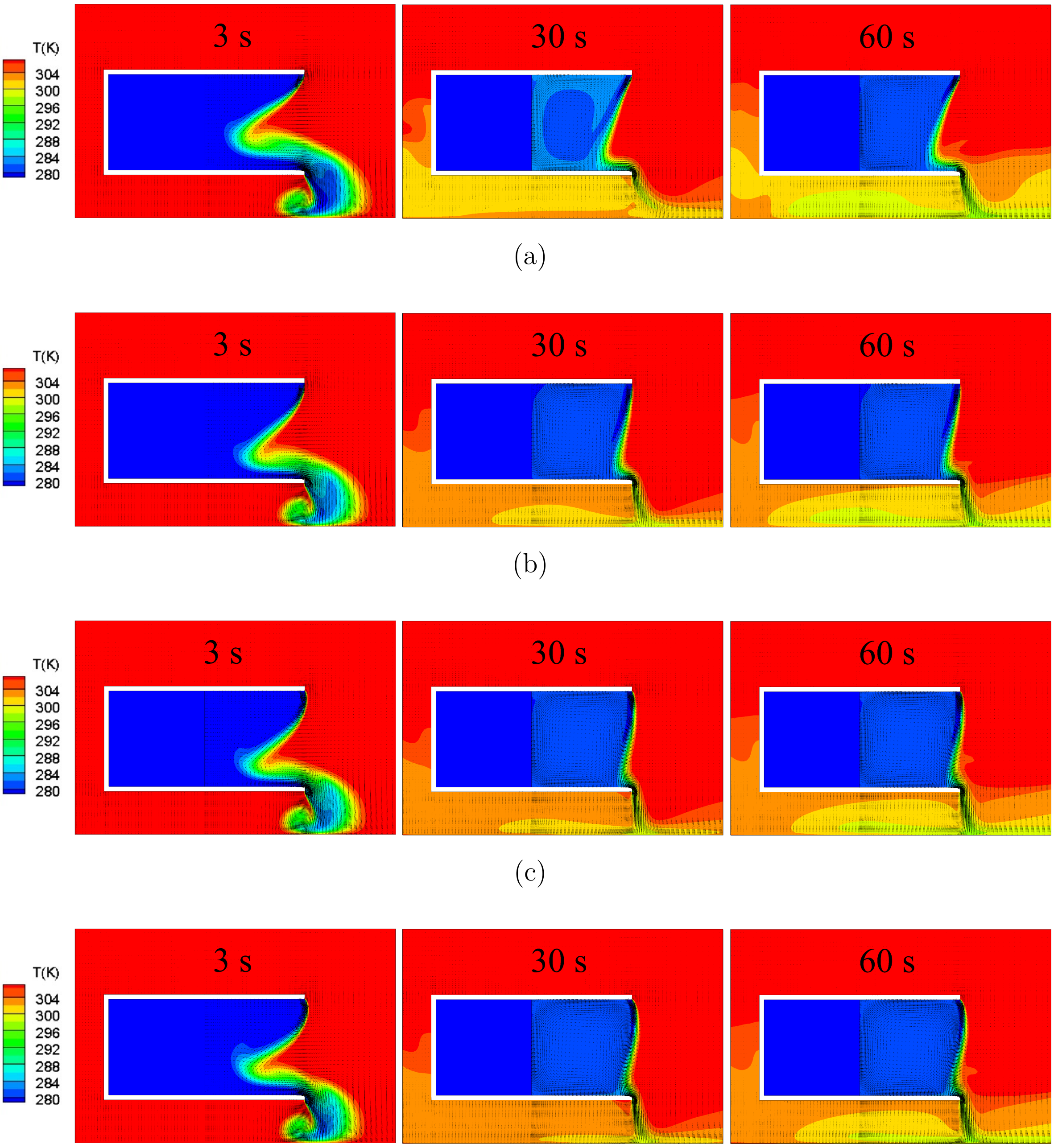

(a)

(b)

(c)

(d)

Figure 6.10: The temperature and velocity distribution (3 s, 30 s, and 60 s) when the jet angles of the air curtain are (a) -15 deg, (b) 0 deg, (c) 15 deg, and (d) 30 deg, respectively

The profiles of the temperature evolution with different jet angles are summarised in Figure 6.11. It can be seen from Figure 6.11(a) that the air curtain with a jet angle of 15 deg provides the best performance in preventing the infiltration of outer hot air and keeps the average air temperature at about 7.6 °C. When the jet angle is decreased to 0 deg or increased to 30 deg, the average air temperature slightly increases. When the jet angle decreased to -15 deg, the average air temperature increases to 11.5 °C. For the temperature at the products-air interface as shown in Figure 6.11(b), the air curtain which is kept at about 7 °C with a vertical jet angle (0 deg) provides the lowest interface temperature among the four jet angles. The interface temperature with the jet angle of 15 deg is higher than the vertical jet angle with an increment of about 0.3 °C. According to the temperature distributions for a 0 deg jet angle and a 15 deg jet angle as shown in Figure 6.10(b) and Figure 6.10(c), it can be seen that the air curtain of the 0 deg jet angle tilts outwards while that for the 15 deg jet angle exhibits an ”s” shape. It implies that within the container with the 0 deg jet angle larger area is occupied by hot air than that with the 15 deg jet angle while with the 0 deg jet angle more cold energy is transported to the gas/products interface. As shown in Figure 6.11(a) and Figure 6.11(b), with the 15 deg jet angle, the average temperature in the container is lower while with the 0 deg jet angle, the temperature at the gas/products interface is lower. Even so, the temperature difference between the two cases with the 0 deg jet angle and the 15 deg jet angle is not significant. From the temperature evolution of the monitoring point 3 outside the container as shown in Figure 6.11(c), it can be seen that only very small cold loss occurs under jet angles of 0 deg, 15 deg, and 30 deg, while the jet angle of -15 deg leads to markedly larger cold loss. From the above, the jet angle between 0 deg and 15 deg is a preferable choice.

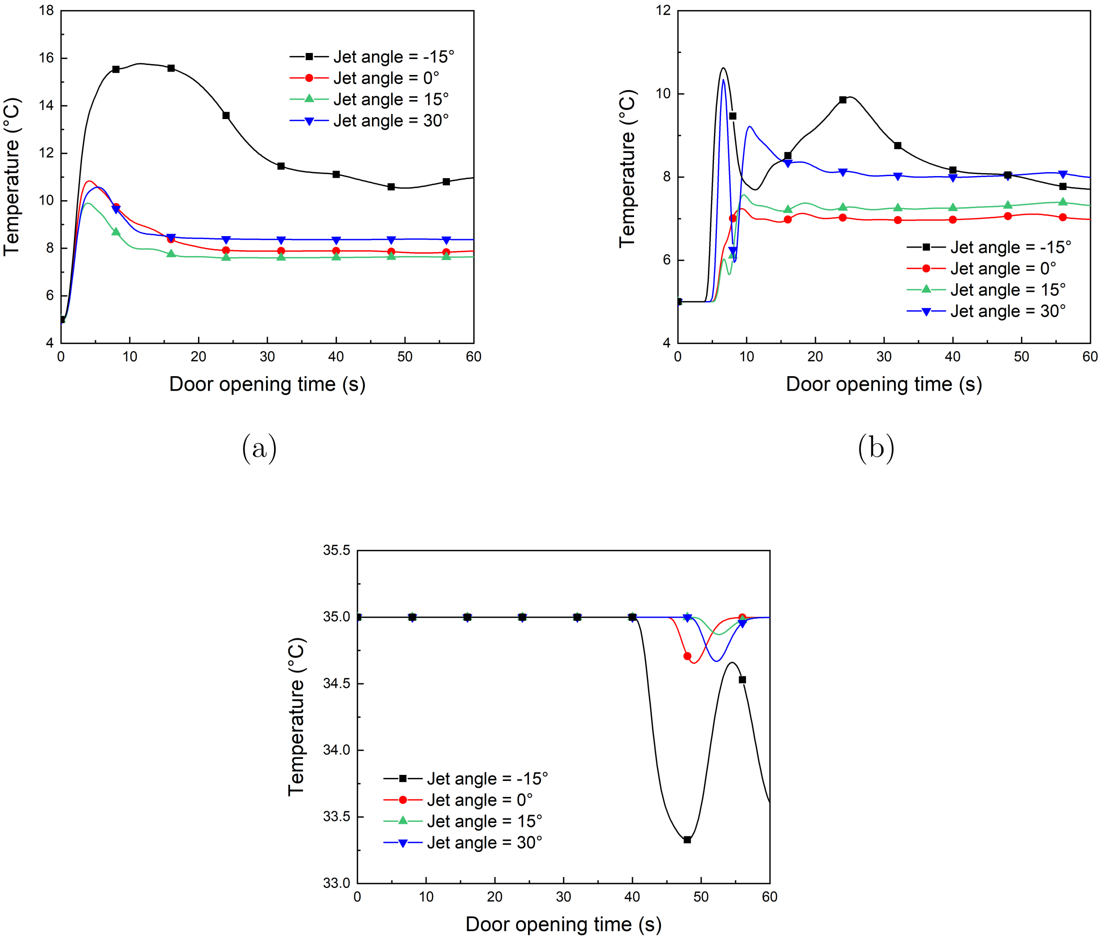

(a)

(b)

(c)

Figure 6.11: The temperature evolution within 1 min after the door is opened with different jet angles: (a) the average air temperature inside the container, (b) the temperature of the monitoring point at the air-products interface, and (c) the temperature of monitoring point 3 outside the container

6.3 Summary

The cooling load was calculated for −25 °C and −33 °C scenarios. By calculating transmission load and infiltration load within vehicle container, the total cooling load can be determined. 308.26 kg NaCl-NH_4Cl solution can provide the cold demand of a 12 ton vehicle for 8 hours, while 240.17 kg meets the cold demand of a 3.5 ton vehicle.

By comparing the working conditions of the refrigerated vehicle, the door opening is one of the most significant reasons that results in the cooling dissipation. In this case, air curtain is introduced to reduce the air infiltration in refrigerated vehicle. Three main air curtain factors which are jet velocity, nozzle width, and jet angle were evaluated with numerical simulations in this study. This work provides significant guidance for the optimal design of utilising the air curtain on refrigerated vehicles. Two non-dimensional parameters, Reynolds number and relative nozzle width, are introduced to extend the applicability of this study (Cong et al., 2019).

CHAPTER 7

CONCLUSIONS & RECOMMENDATIONS

7.1 Conclusions

The purpose of this study is to develop suitable PCMs for both −25 °C and −33 °C vehicle transportation and understand the heat and mass flow in a temperature controlled vehicle.

To sum up, the following conclusions can be drawn:

- The NaCl-NH_4Cl solution and eutectic $MgCl_2$ solution have exhibited favourable thermophysical properties at −25 °C and −33 °C, respectively;
- The mass ratio of salt and water was studied and optimised;
- An approach for identifying the ternary eutectic point at subzero temperatures is optimised;
- The optimised techniques of adding thermal conductivity enhancers, nucleation agents and thickening/gelling agents are developed;
- The impact of the nozzle width, jet velocity and jet angle on the performance of air curtain is studied and the preferable parameter combination is found.

The eutectic NaCl-NH_4Cl solutions have shown the best thermophysical properties among the ternary solution candidates. By comparing the charng/discharging process and stability, the best mass ration of NaCl, NH_4Cl and water is 18.54%, 7.29%, and 74.17%, respectively. By applying the similar method, the formulation of eutectic $MgCl_2$ solution with the best thermoproperties was found. With 49 wt% of $MgCl_2{\cdot}6H_2O$ powder in distilled water, eutectic $MgCl_2$ solution is formed. A new approach for identifying the ternary eutectic point that simplifies the experiment procedure and provides accurate eutectic composition as demanded was illustrated. The phase change temperature and latent heat of the ternary PCM was measured by DSC. The experiment data was combined with the 4^{th} order polynomial fitting to help determine the eutectic composition.

Adding the thermal conductivity enhancers, nucleation agents and thickening/gelling agents into the PCMs can effectively improve the thermoproperties of PCMs. However, the latent heat and energy storage capability of PCMs will be negatively affected by the additives. Therefore, a balance between different properties was studied based on the demand of the project. It is found that with 2% graphite powder (GP) added, the thermal diffusivity of the NaCl-NH_4Cl solution is increased by 22%. Similarly, with 2% GP, the thermal conductivity of the $MgCl_2$ solution was increased by 24.5%. It was observed that diatomite can suppress the supercooling effect with the minimum amount of 0.2% addition. The adding of the thickening/gelling agent helps reduce the phase separation and stabilise the PCM system. 4% xanthan, CMC and polyacrylamide all have significant thickening capability towards the salt-water based PCM. 1% of CMC does not only stabilises the PCM system but also ensures the effective cooling of the composite $MgCl_2$ system at the temperature of −45 °C. The corrosion effect of the composite PCMs was evaluated. A recommendation guidance was made for solution with stainless steel 316, stainless steel 304, aluminium and copper K65 plates at ambient temperature, respectively.

The addition of an air curtain significantly decreases the cold loss within the container. The jet velocity and nozzle width of the air curtain provide larger influences on the air temperature distribution and cold loss inside the container than the jet angle. With an increasing jet velocity, the cold loss decreases. When the jet velocity increases to a certain value, its further increase can only provide very limited improvement in reduction of cold loss and preservation of low temperature and lead to low system efficiency. A stable and effective air curtain can be obtained by precisely tailoring the key parameters to keep the inner air temperature rise below 3 °C. The preferable parameter combination in this study was a jet velocity of 2 m/s, a nozzle width of 7.5 cm, and a jet angle between 0 deg and 15 deg (Cong et al., 2019).

7.2 Recommendations & future work

Based on the findings of this thesis, the recommendation for furture work is as follows:

- Other salts and thermophysical property enhancers should be studied. Based on the results of different formulations, a library should be established to provide guidance of selecting PCMs for different applications;
- The eutectic point analysis technique in the thesis can be promoted to other salt-water solutions with due adjustment;
- The cold storage performance of actual refrigerated vehicles with the PCMs developed in this thesis should be evaluated to provide data establishing a more accurate mathematical model of this application.

LIST OF PUBLICATIONS

L. Cong, Q. Yu, G. Qiao,et al., “Effects of air curtain on temperature distribution in refrigerated vehicles under a hot climate condition,”*Journal of Thermal Science and Engineering Applications*, pp. 1–23, 2019.

L. Cong, X. She, G. Leng, G. Qiao, C. Li, and Y. Ding, “Formulation and characterisation of ternary salt based solutions as phase change materials for cold chain applications,”*Energy Procedia*, vol. 158,pp. 5103–5108, 2019.

Q. Yu, Z. Jiang, **L. Cong**, T. Lu, B. Suleiman, G. Leng, Z. Wu, Y.Ding, and Y. Li, “A novel low-temperature fabrication approach of composite phase change materials for high temperature thermal energy storage,”*Applied Energy*, vol. 237, pp. 367–377, 2019.

A. Palacios, **L. Cong**, M. Navarro, Y. Ding, and C. Barreneche, “Thermal conductivity measurement techniques for characterizing thermal energy storage materials–a review,”*Renewable and Sustainable Energy Reviews*, vol. 108, pp. 32–52, 2019.

Y. Huang, **L. Cong**, X. She, Y. Li, and Y. Ding, “A novel method to predict thermal conductivity of nacl/water based MCNT nano-suspesnion for cold energy storage,”*Energy Procedia*, vol. 158, pp. 4834–4839, 2019.

J. Liu, X. She, X. Zhang, **L. Cong**, L. Man, B. Lindeman, and T. Lin, “Experimental and theoretical study on a novel double evaporating temperature chiller applied in THICS using r32/r236fa,”*Inter-national Journal of Refrigeration*, vol. 75, pp. 343–351, 2017.

X. She, **L. Cong**, B. Nie, G. Leng, H. Peng, Y. Chen, X. Zhang, T.Wen, H. Yang, and Y. Luo, “Energy-efficient and -economic technologies for air conditioning with vapor compression refrigeration:A comprehensive review,”*Applied Energy*, vol. 232, pp. 157–186,Dec. 2018.

X. Peng, X. She, **L. Cong**, T. Zhang, C. Li, Y. Li, L. Wang, L. Tong,and Y. Ding, “Thermodynamic study on the effect of cold and heat recovery on performance of liquid air energy storage,” *Applied Energy*, vol. 221, pp. 86–99, 2018.

X. She, X. Peng, T. Zhang, **L. Cong**., “Preliminary study of liquid air energy storage integrated with LNG cold recovery,” *Energy Procedia*, vol. 158,pp. 4903–4908, 2019.

N. M. Elena, A. Palacios, T. Hughes, C. Connolly, H. Uppal, **L. Cong**, X.

Lei, G. Qiao, G. Leng, and Y. Ding, “Ceramic-salt based composites for thermal energy storage,” *Energy Storage Science and Technology*, vol. 6, no. 4, 688, p. 688, 2017.

G. Xu, G. Leng, C. Yang, Y. Qin, Y. Wu, H. Chen, **L. Cong**, and Y.Ding, “Sodium nitrate–diatomite composite materials for thermal energy storage,” *Solar Energy*, vol. 146, pp. 494–502, 2017.

G. Leng, H. P. Navarro, Q. Yu, G. Wellio, G. Qiao, C. Li, Y. Huang,Y. Zhao, G. Zhang, S. C. Y. Meng, C. J. Chang, Y. Li, Y. Ding, Z. Jiang, and **L. Cong**, “Design of composite materials/devices for thermal storage – a critical review,” *Veruscript Functional Nanomaterials*, vol. 2, 2018.

G. Qiao, H. Cao, F. Jiang, X. She, **L. Cong**, et al., “Experimental study of thermophysical characteristics of molten nitrate salts based nanofluids for thermal energy storage,”*ES Energy Environment*, 2019.

C. Li, Q. Li, Y. Zhao, **L. Cong**, et al., “Composite phase change materials for thermal energy storage: From molecular modelling based formulation to innovative manufacture,”*Energy Procedia*, vol. 158, pp. 4510–4516, 2019.

BIBLIOGRAPHY

Abedin, Ali H and A Marc Rosen (2011). “A critical review of thermochemical energy storage systems”. In: *The Open Renewable Energy Journal* 4.1.

Ahmed, Mashud, Oliver Meade, and Mario A Medina (2010). “Reducing heat transfer across the insulated walls of refrigerated truck trailers by the application of phase change materials”. In: *Energy Conversion and Management* 51.3, pp. 383–392.

Akdemir, S (2008). “Designing of cold stores and choosing of cooling system elements”. In: *Journal of Applied Sciences* 8.5, pp. 788–794.

Araújo, Adriano Antunes Souza et al. (2010). “Determination of the melting temperature, heat of fusion, and purity analysis of different samples of zidovudine (AZT) using DSC”. In: *Brazilian Journal of Pharmaceutical Sciences* 46.1, pp. 37–43.

ASHRAE (2010). “Commodity Storage Requirements”. In: *ASHRAE Handbook - Refrigeration (SI Edition)*. ASHRAE. Chap. 21, pp. 1–10.

ASHRAE (2014a). “Cargo Containers, Rail Cars, Trailers, And Trucks”. In: *ASHRAE Handbook-Refrigeration.* ASHRAE. Chap. 25, pp. 1–13.

— (2014b). “Refrigerated-Facility Loads”. In: *ASHRAE Handbook-Refrigeration.* ASHRAE. Chap. 24, pp. 1–10.

ASTM G1-03 (2017). *Standard Practice for Preparing, Cleaning, and Evaluating Corrosion Test Specimens.* URL: `https://compass.astm.org/download/G1.1337.pdf` (visited on 02/08/2018).

Badr, O, PW O’Callaghan, and SD Probert (1990). “Vapour-compression refrigeration systems”. In: *Applied Energy* 36.4, pp. 303–331.

Beaupere, N, U Soupremanien, and L Zalewski (2018). “Nucleation triggering methods in supercooled phase change materials (PCM), a review”. In: *Thermochimica acta.*

Beckmann, Wolfgang (2013). *Crystallization: Basic concepts and industrial applications.* John Wiley & Sons.

Belleghem, Marnix Van et al. (2012). “Heat transfer through vertically downward-blowing single-jet air curtains for cold rooms”. In: *Heat Transfer Engineering* 33.14, pp. 1196–1206.

Boettinger, William J. et al. (2011). “DTA and Heat-Flux DSC Measurements of Alloy Melting and Freezing”. In: *Methods for phase diagram determination.* elsevier. Chap. 5, pp. 169–170.

Cabeza, Luisa F (2008). *Heat And Cold Storage With PCM: An Up To Date Introduction Into Basics And Applications.* Springer.

Cabeza, Luisa F et al. (2011). “Materials used as PCM in thermal energy storage in buildings: a review”. In: *Renewable and Sustainable Energy Reviews* 15.3, pp. 1675–1695.

Cao, Zhikun et al. (2010). “Application of an effective strategy for optimizing the design of air curtains for open vertical refrigerated display cases”. In: *International Journal of Thermal Sciences* 49.6, pp. 976–983.

Çengel, YUNUS A. and Afshin J. Ghajar (2011). “Refrigeration and freezing of foods”. In: *Heat and Mass Transfer: Fundamentals and Applications.* New York: McGraw-Hill Education. Chap. 17. URL: `http://highered.mheducation.com/sites/dl/free/0073398187/835451/Chapter17.pdf`. (Accessed 02/05/2018).

Chaney, Lawrence, Eric Sailor, et al. (2008). “Thermal Load Reduction of Truck Tractor Sleeper Cabins”. In: *SAE International Journal of Commercial Vehicles* 1.2008-01-2618, pp. 268–274.

CIBSE (2009). “Refrigeration Selection and Storage Temperatures page”. In: *Energy efficiency in commercial kitchens.* CIBSE. Chap. 12, pp. 28–34.

Coachworks, Jackson (2018). *Aero Roof Eco Truck.* URL: `http://www.jacksoncoachworks.co.uk/aero-roof-eco.html` (visited on 10/11/2018).

ColdCar (2016). URL: `https://www.coldcarusa.com/eutectic` (visited on 10/11/2018).

Cong, Lin et al. (2019). “Effects of an Air Curtain on the Temperature Distribution in Refrigerated Vehicles Under a Hot Climate Condition”. In: *Journal of Thermal Science and Engineering Applications* 11.6.

Cui, YS (2009). “Study on phase equilibrium of ternary system NaCl–NH_4Cl–H_2O”. In: *J Salt Chem Ind* 38.1, pp. 11–14.

Cunha, Jose Pereira da and Philip Eames (2016). “Thermal energy storage for low and medium temperature applications using phase change materials–a review”. In: *Applied energy* 177, pp. 227–238.

Dearman (2016). *A Technical Introduction.* URL: `http://dearman.co.uk/wp-content/uploads/2016/05/Dearman-A-Technical-Introduction-For-Web-1.pdf` (visited on 03/21/2017).

Deng, TL, Huan Zhou, and Xia Chen (2013). “Salt-water system phase diagrams and applications”. In: *Chem. Ind. Press, Beijing.*

Department for Business, Energy & Industrial Strategy (2017). *Energy Consumption in the UK.* URL: `https://www.gov.uk/government/uploads/system/uploads/attachment_data/file/633503/ECUK_2017.pdf` (visited on 01/30/2018).

Department for Business, Energy & Industrial Strategy (2018). *Updated Energy And Emissions Projections 2018*. URL: `https://assets.publishing.service.gov.uk/government/uploads/system/uploads/attachment_data/file/794590/updated-energy-and-emissions-projections-2018.pdf` (visited on 01/30/2018).

Dieckmann, Jens Holger (2006). *Latent heat storage in concrete*. URL: `http://www.eurosolar.org/new/pdfs_neu/Thermal/IRES2006_Dieckmann.pdf` (visited on 03/05/2017).

Dong, Ouyang et al. (2018). "A Novel Composite Phase-Change Material: CaCl2 · 6H2O+ MgCl2 · 6H2O+ NH4Cl". In: *Australian Journal of Chemistry* 71.6, pp. 416–421.

Downing, CC and WA Meffert (1993). "Effectiveness of cold-storage door infiltration protective devices (rp-645)". In: *TRANSACTIONS-AMERICAN SOCIETY OF HEATING REFRIGERATING AND AIR CONDITIONING ENGINEERS* 99, pp. 356–356.

Eby. S. W, Collister. R. L (1955). "Insulation in refrigerated transportation body design". In: *Rfrig. Engin.* 63.7.

Erol, N (1993). "Fundamental methods for refrigeration and air-conditioning". In: *Istanbul Technical University, Alumni Association of Vocational School of Maritime, Mar Ajans, Istanbul, Turkey.*

Evans, JA et al. (2014). “Assessment of methods to reduce the energy consumption of food cold stores”. In: *Applied Thermal Engineering* 62.2, pp. 697–705.

Ferrer, Gerard et al. (2015). “Corrosion of metal containers for use in PCM energy storage”. In: *Renewable Energy* 76, pp. 465–469.

Foster, A et al. (2013). “Freely available cold store energy models”. In: *ICCC 2013*.

Foster, AM et al. (2003). “Experimental verification of analytical and CFD predictions of infiltration through cold store entrances”. In: *International Journal of Refrigeration* 26.8, pp. 918–925.

Gao, Daolin et al. (2015). “Thermal characteristics of room temperature inorganic phase change system containing calcium chloride”. In: *Chemical Research in Chinese Universities* 31.3, pp. 452–456.

Gao, Haiyang (2019). “Analysis of New Energy-saving Technology for Cold Chain Logistics”. In: *IOP Conference Series: Earth and Environmental Science*. Vol. 252. 3. IOP Publishing, pp. 1–5.

Gao, Xiaoqiang et al. (2018). “Solid–Liquid Phase Equilibria of the Ternary System (2-Naphthaldehyde+ 4-Methylphthalic Anhydride+ Ethyl Acetate) at (288.15, 298.15, and 308.15) K”. In: *Journal of Chemical & Engineering Data* 63.8, pp. 2848–2855.

Gasia, Jaume, Laia Miró, and Luisa F Cabeza (2016). “Materials and system requirements of high temperature thermal energy storage systems: A review. Part 2: thermal conductivity enhancement techniques”. In: *Renewable and Sustainable Energy Reviews* 60, pp. 1584–1601.

Ghali, Edward, Vedula S Sastri, and Mimoun Elboujdaini (2007). *Corrosion prevention and protection: practical solutions.* John Wiley & Sons.

Gin, Benjamin and Mohammed M Farid (2010). “The use of PCM panels to improve storage condition of frozen food”. In: *Journal of Food Engineering* 100.2, pp. 372–376.

Gök, Özgül, Metin Ö Yilmaz, and Halime Ö Paksoy (2006). *Stabilization of Glauber’s salt for latent heat storage.*

GOSNEY, WB and HAL QLAMA (1976). “HEAT AND ENTHALPY GAINS THROUGH COLD ROOM DOORWAYS”. In: *Proceedings of the Institute of Refrigeration.*

Grodzka, PG et al. (1969). “Space Thermal Control by Freezing and Melting”. In: *Second Interim Report," Space Thermal Control Study", LMSC/HREC-D148619, Contract NAS8-21123, Lockheed Missiles & Space Company, Huntsville, Alabama.*

Han, Bumsoo et al. (2006). “A quantitative analysis on latent heat of an aqueous binary mixture”. In: *Cryobiology* 52.1, pp. 146–151.

He, Qinbo et al. (2012). “Experimental study on thermophysical properties of nanofluids as phase-change material (PCM) in low temperature cool storage”. In: *Energy conversion and management* 64, pp. 199–205.

Hendrix, WA, DR Henderson, and HZ Jackson (1989). “Infiltration heat gains through cold storage room doorways”. In: *ASHRAE Transactions (American Society of Heating, Refrigerating and Air-Conditioning Engineers); (USA)* 95. ISSN: 0001-2505.

Himran, Syukri, Aryadi Suwono, and G Ali Mansoori (1994). “Characterization of alkanes and paraffin waxes for application as phase change energy storage medium”. In: *Energy Sources* 16.1, pp. 117–128.

Hirschey, Jason et al. (2018). “Review of Inorganic Salt Hydrates with Phase Change Temperature in Range of 5 to 60°C and Material Cost Comparison with Common Waxes”. In: *5th International High Performance Buildings Conference.*

Honcova, Pavla et al. (2017). “Suppressing supercooling in magnesium nitrate hexahydrate and evaluating corrosion of aluminium alloy container for latent heat storage application”. In: *Journal of Thermal Analysis and Calorimetry* 129.3, pp. 1573–1581.

Hou, Pumin et al. (2018). “Preparation and Thermal Performance Enhancement of Low Temperature Eutectic Composite Phase Change Materials Based on Na2SO4 · 10H2O”. In: *Materials* 11.11, p. 2230.

Huang, Jingjing et al. (2018). “Solid-liquid phase equilibria of ternary system $Na_2S_2O_3$-Na_2SO_4-H_2O in a wide range of temperatures: Measurement and application”. In: *The Journal of Chemical Thermodynamics* 125, pp. 1–10.

Huang, Li and Udo Piontek (2017). “Improving Performance of Cold-Chain Insulated Container with Phase Change Material: An Experimental Investigation”. In: *Applied Sciences* 7.12, p. 1288.

Jankowski, Nicholas R and F Patrick McCluskey (2014). “A review of phase change materials for vehicle component thermal buffering”. In: *Applied Energy* 113, pp. 1525–1561.

Jiang, Juan et al. (2016). “Solubility Phase Diagram of the $Ca(NO_3)_2$–$LiNO_3$–H_2O System”. In: *Journal of Chemical & Engineering Data* 61.3, pp. 1125–1130.

Juárez, José Octavio et al. (2011). “Numerical study of natural convection in an open cavity considering temperature-dependent fluid properties”. In: *International Journal of Thermal Sciences* 50.11, pp. 2184–2197.

Kant, Karunesh, Amritanshu Shukla, and Atul Sharma (2016). “Ternary mixture of fatty acids as phase change materials for thermal energy storage applications”. In: *Energy Reports* 2, pp. 274–279.

Katsuki, Kazutaka et al. (2017). “Liquid-solid phase equilibria and the frozen ratio of ternary aqueous solution of acetic acid and sodium chloride”. In: *International Journal of Food Properties.*

Khan, Md Imran Hossein and Hasan MM Afroz (2013). “Effect of phase change material on performance of a household refrigerator”. In: *Asian Journal of Applied Sciences* 6.2, pp. 56–67.

Kharagpur, IIT (2016). *Lesson 35 Cooling And Heating Load Calculations-Estimation Of Required Cooling/Heating Capacity.* URL: `http://nptel.ac.in/courses/112105129/pdf/R&AC%20Lecture%2035.pdf` (visited on 01/30/2018).

Krishna, D Jaya and Aditya Shinde (2017). “Step by Step Methodology for the Assessment of Metal Corrosion Rate with PCMs Suitable for Low Temperature Heat Storage Applications”. In: *Materials Today: Proceedings* 4.9, pp. 10039–10042.

Kumano, Hiroyuki et al. (2007). “Study on latent heat of fusion of ice in aqueous solutions”. In: *International Journal of Refrigeration* 30.2, pp. 267–273.

Laguerre, O et al. (2014). “Using simplified models of cold chain equipment to assess the influence of operating conditions and equipment design on cold chain performance”. In: *International Journal of Refrigeration* 47, pp. 120–133.

Lane, GA (1983). “Solar heat storage: Latent heat materials”. In: *Volume 1. Background and scientific principles.*

Li, Gang et al. (2013a). “Review of cold storage materials for subzero applications”. In: *Energy* 51, pp. 1–17.

Li, Hairong et al. (2013b). “Aqueous preparation of polyethylene glycol/sulfonated graphene phase change composite with enhanced thermal performance”. In: *Energy conversion and management* 75, pp. 482–487.

Li, Min, Zhishen Wu, and Jinmiao Tan (2012). “Properties of form-stable paraffin/silicon dioxide/expanded graphite phase change composites prepared by sol–gel method”. In: *Applied energy* 92, pp. 456–461.

Li, Runjing et al. (2019). “Glass transition, structural relaxation and stability of spray-dried amorphous food solids: A review”. In: *Drying Technology* 37.3, pp. 287–300.

Li, Ting, Xin Pan, and Tiejin Ying (2011). “Optimization and Application of Formula for CTESM as Temperature Regulator in Food Storage”. In:

Journal of Chinese Institute of Food Science and Technology 11.4, pp. 115–122.

Liang, Jing Jing et al. (2015). “Numerical simulation of the influence of a internally suction type air curtain to refrigerated truck’s heat preservation performance”. In: *2015 International conference on Applied Science and Engineering Innovation*. Atlantis Press.

Liang, Lin and Xi Chen (2018). “Preparation and Thermal Properties of Eutectic Hydrate Salt Phase Change Thermal Energy Storage Material”. In: *International Journal of Photoenergy* 2018.

Lide, David R (2010). “Aqueous solubility of inorganic compounds at various temperatures”. In: *CRC Handbook of Chemistry and Physics, 90th Edition (Internet Version 2010). CRC Press/Taylor and Francis, Boca Raton, FL.*

Liebers, Mike et al. (2017). “Using Air Walls for the Reduction of Open-Door Heat Losses in Buses”. In: *SAE International Journal of Commercial Vehicles* 10.2017-01-9179, pp. 423–433.

Liu, Ming (2010). “Development of phase change thermal storage unit for refrigerated trucks”. PhD thesis.

Liu, Ming, Wasim Saman, and Frank Bruno (2012). “Development of a novel refrigeration system for refrigerated trucks incorporating phase change material”. In: *Applied Energy* 92, pp. 336–342.

Liu, Ming, Wasim Saman, and Frank Bruno (2014). “Computer simulation with TRNSYS for a mobile refrigeration system incorporating a phase change thermal storage unit”. In: *Applied Energy* 132, pp. 226–235.

Lu, W and SA Tassou (2013). “Characterization and experimental investigation of phase change materials for chilled food refrigerated cabinet applications”. In: *Applied energy* 112, pp. 1376–1382.

Maurya, Neetish Kumar and Ajay Mandal (2016). “Studies on behavior of suspension of silica nanoparticle in aqueous polyacrylamide solution for application in enhanced oil recovery”. In: *Petroleum Science and Technology* 34.5, pp. 429–436.

Mehling, Harald and Luisa F Cabeza (2008). “Solid-liquid phase change materials”. In: *Heat and cold storage with PCM*. New York: Springer. Chap. 2.

Mitsui, Takeo (1997). *New cosmetic science*. Elsevier.

Mo, Songping et al. (2017). “Phase change characteristics of ethylene glycol solution-based nanofluids for subzero thermal energy storage”. In: *International Journal of Energy Research* 41.1, pp. 81–91.

Moore, Emily B and Valeria Molinero (2011). “Structural transformation in supercooled water controls the crystallization rate of ice”. In: *Nature* 479.7374, p. 506.

Moreno, Pere et al. (2014). “Corrosion of metal and metal alloy containers in contact with phase change materials (PCM) for potential heating and cooling applications”. In: *Applied Energy* 125, pp. 238–245.

Moureh, J, N Menia, and D Flick (2002). “Numerical and experimental study of airflow in a typical refrigerated truck configuration loaded with pallets”. In: *Computers and Electronics in Agriculture* 34.1-3, pp. 25–42.

MRao, Chandra Gopala (2015). “Design of Small-Capacity Cold Storages”. In: *Engineering for storage of fruits and vegetables: cold storage, controlled atmosphere storage, modified atmosphere storage.* Academic Press. Chap. 23, pp. 389–425.

Nagano, K et al. (2003). “Thermal characteristics of manganese (II) nitrate hexahydrate as a phase change material for cooling systems”. In: *Applied thermal engineering* 23.2, pp. 229–241.

Nagano, K et al. (2004). “Thermal characteristics of magnesium nitrate hexahydrate and magnesium chloride hexahydrate mixture as a phase change material for effective utilization of urban waste heat”. In: *Applied Thermal Engineering* 24.2-3, pp. 221–232.

Nelson, Stephen A. (2011). *Ternary Phase Diagrams.* URL: `https://www.tulane.edu/~sanelson/eens212/ternaryphdiag.htm` (visited on 01/07/2019).

Npower (2020). *What are the Economy 7 peak and off-peak periods?* URL: `https://www.npower.com/faq/179` (visited on 08/26/2020).

Oró, E et al. (2012). "Review on phase change materials (PCMs) for cold thermal energy storage applications". In: *Applied Energy* 99, pp. 513–533.

Oró, Eduard et al. (2013). "Corrosion of metal and polymer containers for use in PCM cold storage". In: *Applied energy* 109, pp. 449–453.

Oró, Eduard et al. (2014). "Energy management and CO2 mitigation using phase change materials (PCM) for thermal energy storage (TES) in cold storage and transport". In: *International journal of refrigeration* 42, pp. 26–35.

Palacios, Anabel et al. (2019). "Thermal conductivity measurement techniques for characterizing thermal energy storage materials–A review". In: *Renewable and Sustainable Energy Reviews* 108, pp. 32–52.

Pasquali, Irene, R Bettini, and F Giordano (2007). "Thermal behaviour of diclofenac, diclofenac sodium and sodium bicarbonate compositions". In: *Journal of Thermal Analysis and Calorimetry* 90.3, pp. 903–907.

Patankar, Suhas (1980). *Numerical heat transfer and fluid flow.* CRC press.

Perry, Robert H and Cecil H Chilton (1973). *Chemical engineers' handbook (fifth Edition).*

Purdon, Frederick Field and Victor Wallace Slater (1946). *Aqueous solution and the phase diagram.* E. Arnold & Company, pp. 63–69.

Purusothaman, M et al. (2017). "Experimental Investigation of Thermal Performance in a Vehicle Cabin Test Setup With Pcm in the Roof". In: *IOP Conference Series: Materials Science and Engineering.* Vol. 197. 1. IOP Publishing, pp. 1–9.

Qureshi, Zubair Ahmad, Hafiz Muhammad Ali, and Shahab Khushnood (2018). "Recent advances on thermal conductivity enhancement of phase change materials for energy storage system: a review". In: *International Journal of Heat and Mass Transfer* 127, pp. 838–856.

Raj, Vivek and Goswami TK (2018). "Use of phase change material (PCM) for the improvement of thermal performance of cold storage". In: *Current Research & Reviews* 1.2, pp. 49–61.

Rathod, Manish K and Jyotirmay Banerjee (2013). "Thermal stability of phase change materials used in latent heat energy storage systems: a review". In: *Renewable and Sustainable Energy Reviews* 18, pp. 246–258.

Ren, SJ et al. (2017). "Corrosion testing of metals in contact with calcium chloride hexahydrate used for thermal energy storage". In: *Materials and Corrosion* 68.10, pp. 1046–1056.

Rycerz, Leszek (2013). “Practical remarks concerning phase diagrams determination on the basis of differential scanning calorimetry measurements”. In: *Journal of Thermal Analysis and Calorimetry* 113.1, pp. 231–238.

Ryu, Hee W et al. (1992). “Prevention of supercooling and stabilization of inorganic salt hydrates as latent heat storage materials”. In: *Solar energy materials and solar cells* 27.2, pp. 161–172.

Safari, A et al. (2017). “A review on supercooling of Phase Change Materials in thermal energy storage systems”. In: *Renewable and Sustainable Energy Reviews* 70, pp. 905–919.

Saha, Dipjyoti and Suvendu Bhattacharya (2010). “Hydrocolloids as thickening and gelling agents in food: a critical review”. In: *Journal of food science and technology* 47.6, pp. 587–597.

Sakare, Priyanka (2014). “Design of cold storage structure for thousand tonne potatoes”. In: *International Journal of Agriculture and Food Science Technology* 5.3, pp. 171–178.

Schmit, Henri et al. (2014). “Three–step method to determine the eutectic composition of binary and ternary mixtures”. In: *Journal of Thermal Analysis and Calorimetry* 117.2, pp. 595–602.

Schreinemakers, F.A.H (1893). “Graphical deductions from the solution isotherms of a double salt and its components”. In: *Z.Phys.Chem* 11, pp. 75–109.

Science, Popular (2014). *Invention Awards 2014: A Cryogenic Engine Powered By Heat*. URL: `https://www.popsci.com/article/technology/invention-awards-2014-cryogenic-engine-powered-heat` (visited on 10/10/2018).

Seidell, Atherton (1919). *Solubilities of inorganic and organic compounds (Second Edition)*. D. Van Nostrand Company. URL: `http://scans.library.utoronto.ca/pdf/1/2/2ndsolubilitieso00seiduoft/2ndsolubilitieso00seid` `bw.pdf` (visited on 01/30/2018).

Shahbaz, Kaveh et al. (2016). “A novel calcium chloride hexahydrate-based deep eutectic solvent as a phase change materials”. In: *Solar Energy Materials and Solar Cells* 155, pp. 147–154.

Sharma, Munesh Kumar and D Buddhi (2013a). “Designing of a noval refrigerated van incorporated phase change material”. In: *International Journal of Latest Research in Science and Technology* 2.1, pp. 447–449.

— (2013b). “Performance studies of refrigerated van having PCM for generating off site refrigeration effect”. In: *Journal of Pure and Applied Science and Technology* 3.1, pp. 1–12.

Shen, HY (2008). “Thermal properties of compound low-temperature phase change materials and application in numeric simulation of refrigerator (Master Thesis)”. In: *College of power engineering, Chongqing University. China.*

Su, Weiguang, Jo Darkwa, and Georgios Kokogiannakis (2015). “Review of solid–liquid phase change materials and their encapsulation technologies”. In: *Renewable and Sustainable Energy Reviews* 48, pp. 373–391.

Tassou, SA, G De-Lille, and YT Ge (2009). “Food transport refrigeration–Approaches to reduce energy consumption and environmental impacts of road transport”. In: *Applied Thermal Engineering* 29.8-9, pp. 1467–1477.

Tassou, SA et al. (2010). “A review of emerging technologies for food refrigeration applications”. In: *Applied Thermal Engineering* 30.4, pp. 263–276.

Toledo, Mettler (2010). *Interpreting DSC curves Part 1: Dynamic Measurements.*

Toner, JD, DC Catling, and B Light (2014). “The formation of supercooled brines, viscous liquids, and low-temperature perchlorate glasses in aqueous solutions relevant to Mars”. In: *Icarus* 233, pp. 36–47.

Tso, CP et al. (2002). “Experimental study on the heat and mass transfer characteristics in a refrigerated truck”. In: *International Journal of Refrigeration* 25.3, pp. 340–350.

Ushak, Svetlana et al. (2016). “Reduction of the subcooling of bischofite with the use of nucleatings agents”. In: *Solar Energy Materials and Solar Cells* 157, pp. 1011–1018.

Veerakumar, C and A Sreekumar (2016). “Phase change material based cold thermal energy storage: Materials, techniques and applications–A review”. In: *international journal of refrigeration* 67, pp. 271–289.

WU, Weidong et al. (2015). “Preparation and thermal properties of nano-organic composite phase change materials for cool storage in air-conditioning”. In: *CIESC Journal* 3, p. 046.

Xie, Ning et al. (2017). “Inorganic Salt Hydrate for Thermal Energy Storage”. In: *Applied Sciences* 7.12, p. 1317.

Xie, Ruhe, Wenbo Tao, and Guanghai Liu (2016). “Development of Phase Change Materials for Refrigerated Transportation of Fruits and Vegetables”. In: *DEStech Transactions on Computer Science and Engineering.*

Ye, Hong et al. (2017). “Study on the influence of air curtain barrier efficiency on infiltration air volume and temperature distribution in large space in winter”. In: *Procedia Engineering* 205, pp. 2509–2516.

Yilmaz, Selma et al. (2009). “New binary alkane mixtures as pcms for cooling applications”. In: *11th International Conference on Thermal Energy Storage for Energy Efficiency and Sustainability, Stockholm International Fairs. Stockholm, Sweden.*

Yinping, Zhang and Jiang Yi (1999). “A simple method, the-history method, of determining the heat of fusion, specific heat and thermal conductivity of phase-change materials”. In: *Measurement Science and Technology* 10.3, p. 201.

Zeng, Yan and Zhibao Li (2015). “Solubility Measurement and Modeling for the NaCl–NH_4Cl–Monoethylene Glycol–H_2O System from (278 to 353) K”. In: *Journal of Chemical & Engineering Data* 60.8, pp. 2248–2255.

Zhang, Yinping, Yuehong Su, and Xinshi Ge (1995). “Prediction of the melting temperature and the fusion heat of (quasi-) eutectic PCM”. In: *Journal of China University of Science and Technology* 25.4, pp. 474–478.

Zheng, DX and XH Wu (2002). “Comprehensive evaluation of eutectic character used as low temperature thermal energy storage”. In: *Cryogenics* 1, pp. 37–45.

Zhijuan, Chang et al. (2013). “Numerical simulation on the food package temperature in refrigerated display cabinet influenced by indoor environment”. In: *Advances in Mechanical Engineering* 5, p. 708785.

Zhou, Dan, Chang-Ying Zhao, and Yuan Tian (2012). “Review on thermal energy storage with phase change materials (PCMs) in building applications”. In: *Applied energy* 92, pp. 593–605.

Zhu, FY et al. (2017). “Phase change performance assessment of salt mixtures for thermal energy storage material”. In: *International Journal of Energy Research* 41.13, pp. 1855–1866.